THE UNIVERSITY
of EDINBURGH

Sparsity Driven Ground Moving Target Indication in Synthetic Aperture Radar

Di Wu

A thesis submitted for the degree of Doctor of Philosophy.
The University of Edinburgh.
May 30, 2018

Abstract

Synthetic aperture radar (SAR) was first invented in the early 1950s as the remote surveillance instruments to produce high resolution 2D images of the illuminated scene with weather-independent, day-or-night performance. Compared to the Real Aperture Radar (RAR), SAR is synthesising a large virtual aperture by moving a small antenna along the platform path. Typical SAR imaging systems are designed with the basic assumption of a static scene, and moving targets are widely known to induce displacements and defocusing in the formed images. While the capabilities of detection, states estimation and imaging for moving targets with SAR are highly desired in both civilian and military applications, the Ground Moving Target Indication (GMTI) techniques can be integrated into SAR systems to realise these challenging missions. The state-of-the-art SAR-based GMTI is often associated with multi-channel systems to improve the detection capabilities compared to the single-channel ones. Motivated by the fact that the SAR imaging is essentially solving an optimisation problem, we investigate the practicality to reformulate the GMTI process into the optimisation form. Furthermore, the moving target sparsities and underlying similarities between the conventional GMTI processing and sparse reconstruction algorithms drive us to consider the compressed sensing theory in SAR/GMTI applications.

This thesis aims to establish an end-to-end SAR/GMTI processing framework regularised by target sparsities based on multi-channel SAR models. We have explained the mathematical model of the SAR system and its key properties in details. The common GMTI mechanism and basics of the compressed sensing theory are also introduced in this thesis. The practical implementation of the proposed framework is provided in this work. The developed model is capable of realising various SAR/GMTI tasks including SAR image formation, moving target detection, target state estimation and moving target imaging. We also consider two essential components, i.e. the data pre-processing and elevation map, in this work. The effectiveness of the proposed framework is demonstrated through both simulations and real data.

Given that our focus in this thesis is on the development of a complete sparsity-aided SAR/GMTI framework, the contributions of this thesis can be summarised as follows. First, the effects of SAR channel balancing techniques and elevation information in SAR/GMTI applications are analysed in details. We have adapted these essential components to the developed framework for data pre-processing, system specification estimation and better SAR/GMTI accuracies. Although the purpose is on enhancing the proposed sparsity-based SAR/GMTI framework, the exploitation of the DEM in other SAR/GMTI algorithms may be of independent interest.

Secondly, we have designed a novel sparsity-aided framework which integrates the SAR/GMTI missions, i.e. SAR imaging, moving target and background decomposition, and target state estimation, into optimisation problems. A practical implementation of the proposed framework with a two stage process and theoretically/experimentally proven algorithms are proposed in this work. The key novelty on utilising optimisations and target sparsities is explained

in details.

Finally, a practical algorithm for moving target imaging and state estimation is developed to accurately estimate the full target parameters and form target images with relocation and refocusing capabilities. Compared to the previous processing steps for practical applications, the designed algorithm consistently relies on the exploitation of target sparsities which forms the final processing stage of the whole pipeline. All the developed components contribute coherently to establish a complete sparsity driven SAR/GMTI processing framework.

Declaration of Originality

I hereby declare that the research recorded in this thesis and the thesis itself was composed and originated entirely by myself in the School of Engineering at The University of Edinburgh.

Di Wu

Acknowledgements

Probably it is only in retrospect that one can better conquer the obstacles. The days of pursuing the Doctor of Philosophy (PhD) degree have been a challenging period from both scientific and routine perspectives. I am very grateful that these joys and frustrations have become the most important lessons in my life.

Foremost, I would like to thank Prof. Mike Davies who supervises me on the PhD study. He has shown impressive intellectual rigour and erudition in the daily work. From him I recognise the perseverance of a pioneering scientist. On one hand, people have problems and they search for algorithms; on the other hand, some people have algorithms and they search for problems. He always inspires me to go for the former case which emphasises the importance of solving practical problems. These precious experiences will continuously encourage me in the future endeavours.

My sincerest gratitude also goes to Dr. Mehrdad Yaghoobi who not only mentors me on general academic research but also gives me detailed instructions on mathematical modelling. His knowledge in efficient signal processing is the valuable treasury that I can always learn from. I hereby would like to congratulate him on being a father!

I would also like to thank my parents for the consistent love and support. I would not have been able to complete all these without their unconditional care and encouragement. Last but not the least, from my deep heart, I would like to thank those sincere friends who have taught me contents and helped me through difficulties. It is forever my great honor to share experiences with them.

> *There will always be signals, they will always need processing, and there will always be new applications, new mathematics and new implementation technologies.*
>
> – Prof. Alan V. Oppenheim, *The Future of Signal Processing*

Just like the literal meaning of PhD, what one really harvests with time is probably not the knowledge but the life philosophy. Novel algorithms can be outdated someday, but the life experiences and the capability of solving problems will accompany me eternally.

Venture the dream, embrace the future!

Contents

List of Figures

List of Tables

Acronyms and Abbreviations

2D	2-Dimensional
3D	3-Dimensional
ATI	Along Track Interferometry
ATR	Automatic Target Recognition
CFAR	Constant False Alarm Rate
CS	Compressed Sensing
DEM	Digital Elevation Model
DPCA	Displaced Phase Center Antenna
EDPCA	Extended Displaced Phase Center Antenna
GMTI	Ground Moving Target Indication
IHT	Iterative Hard Thresholding
LASSO	Least Absolute Shrinkage and Selection Operator
MDV	Minimum Detectable Velocity
NASA	National Aeronautics and Space Administration
PRF	Pulse Repetition Frequency
PSF	Point Spread Function
RCS	Radar Cross Section
RIP	Restricted Isometry Property
RP	Random Projections
RVP	Residual Video Phase
SAR	Synthetic Aperture Radar
SINR	Signal-to-Interference and Noise Ratio
STAP	Space-Time Adaptive Processing
TBP	Time-Bandwidth Product

Nomenclature

$\mathbf{X}$	the complex SAR image
$\mathbf{X}_d$	the SAR image of the moving targets
$\mathbf{X}_s$	the SAR image of the background
$\mathbf{Y}_i$	the 2D phase history for the i-th channel
$\widetilde{\mathbf{Y}}_i$	the pre-processed phase histories of the i-th channel
$\mathbf{V}^{(x)}$	the x-direction velocities of the image pixels ($\mathbf{V}^{(y)}$ and $\mathbf{V}^{(z)}$ likewise)
$\mathbf{V}$	the velocity map ($\mathbf{V}^{(x)}$,$\mathbf{V}^{(y)}$,$\mathbf{V}^{(z)}$) of the whole observed scene
$\mathbf{P}$	the phase correction matrix on $\mathbf{X}_d$ between different channels
$\mathbb{G}_{ml}$	the discrete grid on which the SAR image is formed
g_i	the antenna gain of the i-th channel
σ	the reflectivity of the moving target
c	the velocity of light
f_k	the discrete range frequencies
τ_n	the discrete slow time with pulse number n
d	the channel spacing
f_{PRF}	the system pulse repetition frequency
$\mathbf{r}$	the instantaneous position vector of the platform
$\mathbf{r}_t$	the instantaneous position vector of the target
$\mathbf{r}_i^{(t)}$	the vector from the i-th antenna to the moving target
$\mathbf{r}_i^{(o)}$	the vector from the i-th antenna to the origin
$\mathbf{v}_t$	the vector that represents the moving target velocity
$\mathbf{v}_p$	the vector that represents the platform velocity
$\mathbf{H}$	the channel balancing matrix in the Doppler and range frequency domain
$Q_i(\Omega)$	the channel-dependent term in $\mathbf{Y}_i$ with the continuous range frequency Ω
$D_{(\omega)}$	the antenna pattern vector in $\mathbf{Y}_i$ with the continuous Doppler frequency ω
$\|\|\|_F$	the Frobenius norm
$\mathcal{N}$	the element-wise normalisation operator
$\odot$	the element-wise product operator
$\oslash$	the element-wise division operator
$\langle \cdot, \cdot \rangle$	the dot product operator

$E\{\cdot\}$ the expected value of the argument

$\mathcal{T}$ the hard-thresholding operator

1

Introduction

1.1 Research Problem

Synthetic aperture radar (SAR) was invented as an imaging technique which enabled high resolution image formation under any weather conditions. Practical SAR systems include airborne SAR and satellite SAR which produce much better image resolution compared to what the real-aperture radar can achieve. SAR mainly benefits from the advanced signal processing techniques, which allow the SAR system to equip much smaller antennas than the ones with real-aperture radar systems. The conventional real-aperture radars require a single large antenna with narrow beamwidth for the high resolution. On the contrary, SAR is mounted with the antennas of small sizes which is obviously beneficial to practical applications. To still provide high resolution with such small antennas, SAR is acquiring samples along a specific flight path and synthesizing a large virtual aperture. The synthesized large aperture can thus produce a very narrow beamwidth. The state-of-the-art SAR theory suggests that the image azimuth resolution of SAR can be half the antennas size, regardless of the range distances [2] [3]. However, such high image resolution comes along with high system complexity and how the observed scene behaves during the monitoring process. In general, the finer SAR image resolution requires the platform to move a longer path. If the observed region contains dynamic parts during the flight, those parts of the SAR image will be blurred correspondingly. Therefore, SAR is mainly an imaging tool for stationary ground reflectors.

The all-weather and high resolution imaging capabilities are obviously gaining favour from the military applications in modern battlefield surveillance. As the military community is particularly interested in detecting and tracking moving targets in the monitored scene, the Ground Moving Target Indication (GMTI) techniques have drawn significant attention to filter out static reflectors and reveal the moving objects. While the SAR and GMTI were historically implemented via different architectures, one attractive exploration was to integrate the SAR and GMTI algorithms into a single framework and benefit from both their features.

Furthermore, a number of investigations have shown that multi-channel SAR systems have significant advantages in SAR-based GMTI. Motivated by the fact that the moving targets are approximately sparse in monitored scene, in this thesis, we aim to link the state-of-the-art compressed sensing theory with the multi-channel SAR-based GMTI applications, and explore the most appropriate framework of sparsity-aided SAR/GMTI.

1.2 Thesis Statement

This thesis investigates the practicality of implementing GMTI missions with multi-channel SAR utilising the sparse concepts. The proposed SAR/GMTI framework is designed by considering the state-of-the-art GMTI methods, i.e. Displaced Phase Centre Antenna (DPCA) and Along Track Interferometry (ATI). Note that DPCA and ATI are subtractive methods on formed SAR images, and the conventional SAR image formation is essentially approximating the solution of an optimisation problem. We are thus motivated to design an optimisation framework for SAR-based GMTI and also exploit the sparse information. Furthermore, some other practical components in SAR/GMTI processing have to be considered, such as the data pre-processing to balance different SAR channels and the utilisation of the DEM information when significant elevation variations exist. All these aspects are investigated in this thesis to establish an end-to-end sparity-driven framework for SAR/GMTI, which is capable of simultaneously forming high resolution images of the observed scene, utilising the elevation information, separating moving targets from the static background, forming moving target images and estimating moving target states.

The proposed framework has achieved experimentally proved performance with the AFRL GOTCHA GMTI challenge dataset [4]. To briefly explain the SAR/GMTI problem to be addressed in this thesis, in Chapter 2 we present the detailed specifications of the SAR scenario, in which a controlled vehicle is moving along a mountainous path and the task is to indicate this target via processing the SAR data. In Chapter 3, we leverage the multi-channel information and elevation map to improve the accuracies and SAR imaging. In chapter 4 and 5, we investigate the appropriate methods to indicate the moving targets while preserving high resolution SAR images, and show that the estimated states are fairly accurate compared to the ground truth.

1.3 Main Contributions

This thesis proposes an end-to-end SAR/GMTI processing framework regularised by sparsities based on multi-channel SAR systems. Motivated by the optimisation equivalence of SAR image formation, we explore the practicality for the optimisation modelling for SAR-based GMTI. Furthermore, we are inspired by the similarities between conventional GMTI methods and sparse reconstruction algorithms to leverage the target sparsities in SAR/GMTI. This thesis reflects our investigations in sparsity driven SAR/GMTI applications and the practical challenges we encountered. We propose a number of implementation algorithms to tackle individual problems and finally integrate the explorations into the complete SAR/GMTI framework.

The main contributions of this thesis are:

1. The SAR channel balancing techniques are analysed and the utilisation of elevation information in SAR/GMTI applications is investigated. Specifically, the channel balancing corresponds to the pre-processing method for the raw data to retrieve the same signal responses for static scatterers among different channels, and the elevation data can serve as the axillary information to improve the SAR/GMTI performance. These are the two essential parts in practical SAR/GMTI that have been adapted to the developed framework to pre-process SAR data, estimate system specifications and improve SAR/GMTI accuracies. The exploitation of the elevation in other SAR/GMTI approaches may be of independent interest, though the purpose is on enhancing the proposed sparsity driven SAR/GMTI framework. Our related investiagations are published in [5].

2. The novel sparsity driven framework has been developed to integrate the SAR/GMTI tasks, i.e. SAR imaging, target/background separation, and target state estimation, into optimisation formulations. All the developed components contribute coherently to establish this complete sparsity-aided SAR/GMTI processing framework. The practical implementation of the proposed framework with a two stage process and theoretically/experimentally proven algorithms are developed in this thesis. The key novelty on structuring optimisations with further target sparsities is explained in details. Our related investiagations are published in [6]. A more complete work has been submitted to related academic journals. Future publications with the complete SAR/GMTI processing framework are obviously in our vision. The idea of using sparsities in indication and decomposition tasks have shown its advantages in various signal processing modalities. For

example, in the defence related domain, the chemical spectral decomposition can benefit from the signal sparsities, and the effectiveness can be significantly improved. We have related publications in [7] [8] [9].

3. The practical algorithm for moving target imaging and state estimation is developed to accurately estimate the full target parameters and form target images with relocation and refocusing capabilities. This investigation serves as the final stage of the SAR/GMTI framework pipeline. While the designed method is implemented after the moving target and background decomposition for practical considerations, it preserves the consistency by exploiting the target sparsities. Our related investiagations are published in [10].

1.4 Thesis Organisation

In Chapter 2, we start with the introduction to Radar systems. The background of Radar and SAR are discussed in details. We then present the SAR signal models along with its processing pipeline, and the received signal model is formulated in this chapter which is used in the remainder of the thesis. Furthermore, we present the basics of sparsity and Compressed Sensing (CS) theory and related applications in this chapter. By establishing a link between SAR/GMTI and CS, we explore the detailed implementation to design a novel SAR-based GMTI framework in this thesis. We next introduce the state-of-the-art GMTI techniques in the SAR/GMTI community, and explain our motivation of designing the sparsity-aided SAR/GMTI framework. The descriptions of the real data used in this thesis are also discussed in this chapter.

In Chapter 3, we investigate several essential parts in the SAR/GMTI processing, i.e. the channel balancing and DEM processing. We present in detail how the SAR channels are different in the signal models and how they can be balanced for the subsequent processing. The incorporation of the elevation map into the SAR applications is also discussed in this chapter. Particularly, we incorporate the DEM into the SAR forward and backward operators, and present both DEM-aided Moving Target Imaging. The performance of the channel balancing and DEM processing are analysed in the experiments with the AFRL GMTI challenge dataset.

In chapter 4, we focus on the SAR-based moving target detections. We present the proposed sparsity-driven GMTI model with its motivation. The differences between the proposed method and conventional methods are analysed. A practical implementation of the proposed model is designed which breaks the framework into a two-stage processing pipeline considering the

difficulties in solving the problem directly. The first stage to separate moving targets from the background is explored in this chapter. We validate the effectiveness of the proposed method through both real SAR data and simulations.

In chapter 5, following the extracted moving targets as described in chapter 4, we design the novel sparsity-aided methods for the moving target state estimation and image formation. The proposed model establishes an optimisation problem to utilise the sparse prior information which is consistent with the method described in Chapter 4. The experiments with both real data and simulations are demonstrated in this Chapter.

In Chapter 6, we conclude the outcomes of this thesis and summarise the future research.

2

Background on SAR and CS

2.1 Introduction

Radar served as the vital military system for "RAdio Detection And Ranging" during World War II [11]. Its early developments mainly focused on the defence monitoring with ground-based devices. The range to the targets can be estimated based on the round-trip time of the transmitted signal, while the angular position of the target is determined via directive antennas. Although this revolutionary technology was initially invented for target detection purposes, it was soon extended with advanced platforms and sophisticated imaging features after the war. In the early 1950s, Synthetic Aperture Radar (SAR) sensors were first introduced as the remote surveillance instruments to provide high resolution 2D images of the monitored region with all-weather, day-or-night capability [12]. Unlike the Real Aperture Radar (RAR) which requires an impractically large antenna to achieve acceptable cross-range resolution, SAR is synthesising a large virtual antenna by moving a small antenna along the platform path [13]. In 1978, the National Aeronautics and Space Administration (NASA) launched the well known SEASAT remote sensing satellite which was the first spaceborne SAR system for earth surface imaging [14]. The developments of SAR were then significantly driven by the success of SEASAT. In the same year, SAR started to be equipped with the state-of-the-art digital processors [15]. Following that, the digital signal processing techniques quickly demonstrated the enormous strength in SAR processing [16]. For the past few decades, both airborne and spaceborne SAR applications have been on the rapid growth trajectories, which were significantly empowered by the emerging SAR processing algirthms. Nowadays, the trend in SAR developments is strongly associated with the advanced SAR-based applications (such as target indication, automatic target recognition [17] [18]) and modalities (such as polarimetry and interferometry [19] [20] [21]).

The indication of moving targets had raised significant interest since Radar systems started to be placed in service especially for battlefield reconnaissance applications. The developments in SAR enabled the high resolution image formation of the monitored region which straightforwardly

led the community to put efforts into investigating SAR-based moving target detection approaches. Some early developments included the detection of ships and the guidance of fire control systems [22]. Within this context, the related applications, such as target detection, state estimation, tracking, and classification, have received remarkable explorations for both military and civilian purposes in the past decades [23] [24] [25]. Some common difficulties for SAR-based GMTI tasks are that the moving targets encounter velocity-induced defocusing and azimuth displacements in the SAR images, and the Doppler frequency shifts of moving targets are very likely to be mixed in the endo-clutter (mainlobe clutter) spectra, i.e. the Doppler band with non-negligible clutter energy. Recently, some striking projects in multi-channel SAR systems led to the potential in advanced target indication abilities [26] [27]. These state-of-the-art SAR platforms significantly mitigated these difficulties in SAR-based GMTI missions. Based on the multi-channel SAR platforms, various clutter suppression algorithms have been proposed to cope with the Ground Moving Targets Indication (GMTI) challenges, e.g. the widely used Displaced Phase Centre Antenna (DPCA), Along Track Interferometry (ATI) and Space-time Adaptive Processing (STAP) [28] [29] [30] [31]. In particular, the DPCA and ATI are the subtractive algorithms which exploit the idea to reveal the moving targets through the differences between different SAR channels. STAP is essentially a filtering method which estimates a weight matrix in the spatial-temporal domain to maximise the Signal-to-Interference-plus-Noise Ratio (SINR) and finds the targets via the statistical test strategies. Note that the adaptive weights are interference covariance matrix dependent which can not be easily estimated, and it induces massive computational complexities to compute the weights for all cells with SAR [32].

It has shown an increasing demand for innovative signal processing algorithms from the industry. In 1949, Shannon's pioneering work [33] asserted that a signal could be exactly recovered with uniformly spaced samples as long as the sampling rate was at least twice the highest frequency contained in the original signal. This sampling rate was then termed the Nyquist rate/frequency. This sampling theorem became one of the most important principles in the modern signal processing, and it initialised the trend of digital signal processing systems. However, some tough problems stemming from practical applications remain: the Nyquist rate can be too high, most signals are not band-limited, and it may be impossible to acquire samples at the ideal rate, etc. Compressed sensing is an emerging technique which enables the reconstruction of high resolution signals from undersampled measurements, and it is widely known for the potential to break the Nyquist-Shannon sampling theorem [34]. A major breakthrough in its theory came around 2005 when researchers proved that, by exploiting the sparsities, the original signals

could be reconstructed with just a small amount of samples under certain conditions [35] [36]. Given that signal sparsities exist in particular systems, CS can thus be explored in a number of sensing modalities. During the past decade, CS attracted significant attention all around the world, and it has already made notable impact on a number of applications, such as Radar [37], the single-pixel camera [38], environmental monitoring [39], compressive imaging architectures [40], MRI [41] [42] and compressive sensor networks [43]. As only a small number of moving targets exist in the monitored region of a SAR system, the GMTI tasks of finding the 'sparse' targets coincide with the core idea of CS. Therefore, we are motivated to focus on the exploitation of sparsity in SAR-based GMTI applications. In this chapter, we will review the backgrounds of SAR basics and the sparse reconstruction theory.

2.2 Synthetic Aperture Radar

2.2.1 SAR Basics

In this section we will go through the fundamental properties of a SAR system and establish the mathematical model for SAR signals. We start by presenting the underlying SAR geometry. Then the spatial resolution of SAR is analysed as this property obviously plays a vital role in GMTI applications. We next give an insight into how the range resolution can be refined with the pulse compression technique which is beneficial to GMTI. Then the received signal can be modelled through the dechirping and deskewing procedures. Finally the received phase history can be reformulated in the range frequency and azimuth time domain as a 2-D complex matrix, and the forward projection process can be rewritten into the matrix-vector form.

Conventional SAR systems can work in three different modes, i.e. stripmap, spotlight, and scan. Particularly the stripmap mode (Fig. 2.3) has fixed beam direction and the Radar footprint follows the SAR swath. The spotlight mode steers the beam direction to consistently focus on the same region with time. The scan mode behaves like the mix of stripmap and spotlight to observe multiple subswaths by steering the antenna. In Fig. 2.1 a typical multi-channel SAR system which operates in the spotlight mode is depicted, and the observed scene contains a number of moving targets. Multiple radar channels provide rich information to improve the overall all SAR/GMTI performance and the spotlight mode can significantly improve the imaging resolution which is beneficial to the GMTI applications. A terrain map that contains elevation information on the z direction is associated with the illuminated region. In this thesis we are particularly interested in

the effects of the elevation information in SAR/GMTI. Multiple radar channels are mounted on an airborne platform, and they are equally spaced along the flight path with a distance d. We thus have multiple received phase histories with this system.

In the rest of the thesis, bold letters denote vectors and matrices and non-bold ones denote scalars. Specifically, the non-bold term is the norm of the bold one with the same name. Let $\mathbf{v}_t = (v^{(x)}, v^{(y)}, v^{(z)})$ be the velocity vector of a moving target in the scene, whereas $\mathbf{v}^{(r)}$ and $\mathbf{v}^{(az)}$ denote its corresponding radial and azimuth velocity respectively. τ_n represents the slow (azimuth) time of the transmitted pulses where $n = \{1, 2, ..., N\}$ is the pulse number. We denote $r_i^{(t)}(\tau_n)$ (the norm of $\mathbf{r}_i^{(t)}(\tau_n)$) as the distance between this target and the $i-$th antenna. Similarly $r_i^{(o)}(\tau_n)$ is the distance from the scene center to the $i-$th channel. The differential range is thus $r_i^{(t)}(\tau_n) - r_i^{(o)}(\tau_n)$. The platform velocity v_p is assumed to be a constant within a short enough sub-aperture.
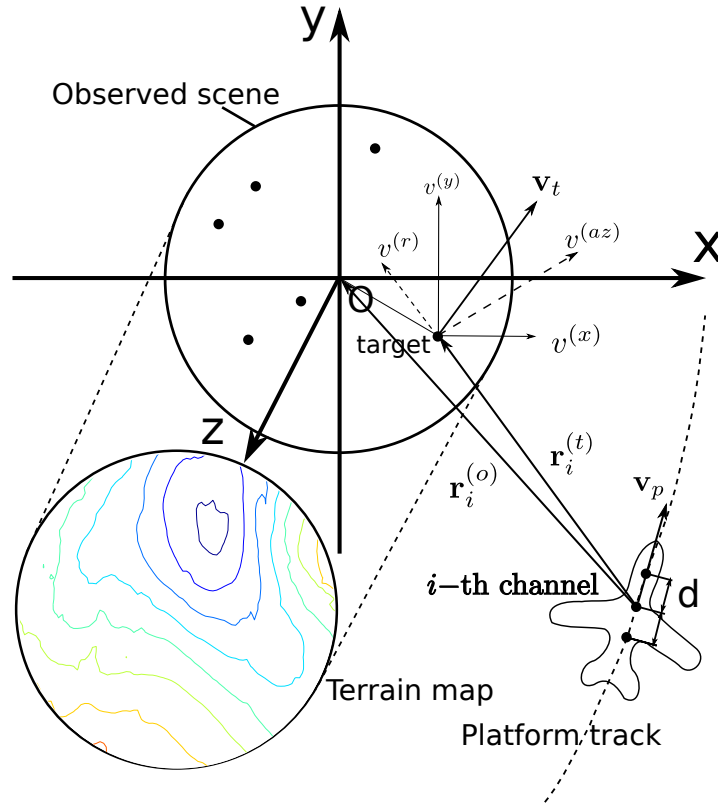
Figure 2.1: The geometry of a typical multi-channel SAR system in the spotlight mode. A number of moving targets are present and the observed scene is associated with a digital elevation map.

9

Spatial Resolution

SAR is widely known to produce high resolution images by moving the small antenna along the flight path to synthesise a large virtual aperture. Following the depicted geometry in Fig. 2.1, in this section, we discuss the spatial resolution of a SAR system in details. The physical resolution in azimuth and range directions reflect the capability of the SAR system to discriminate reflectors. Specifically, the geometric resolution represents the minimum separation to resolve two different targets, and this property is crucial as it is strongly associated with the target indication accuracies. From this perspective, the SAR-based GMTI frameworks are overall bounded by the spatial resolution.

We first consider the spatial resolution in the range direction. As shown in Fig. 2.2, two nearby targets are away from the antenna with the distances R_1 and R_2 respectively. Therefore, to resolve the two targets, the difference on the round-trip echo times of the two targets cannot be less than the effective pulse duration:
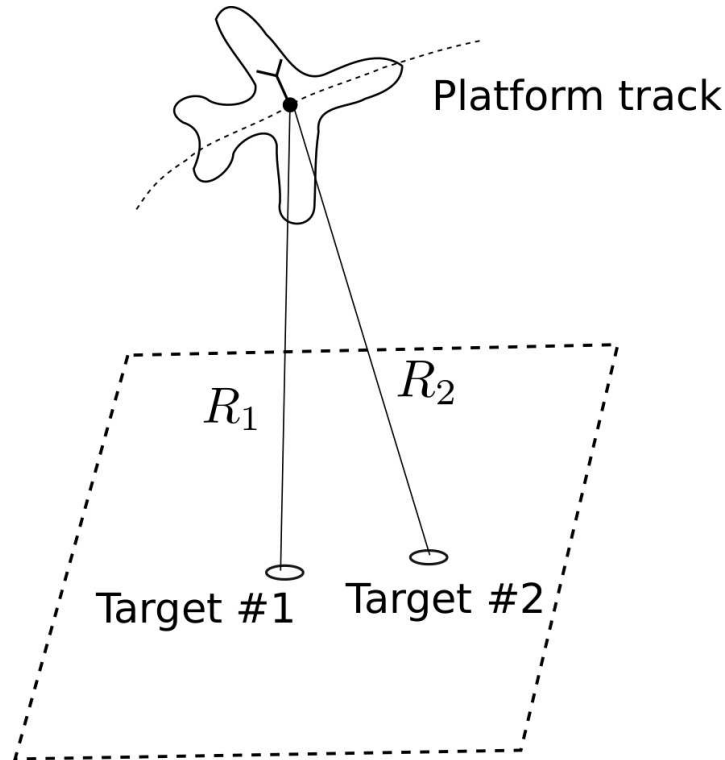
Figure 2.2: The SAR system with two nearby targets that are away from the platform with distances R_1 and R_2 respectively.

$$\frac{|2R_1 - 2R_2|}{c} >= \tau \tag{2.1}$$

where τ is the pulse duration. Given that $B = 1/\tau$ is the transmitted pulse bandwidth, the range resolution Δr is the minimum $|R_1 - R_2|$ in (2.1) which can be expressed as:

$$\Delta r = \frac{c\tau}{2} \tag{2.2}$$

Note that Δr represents the spatial resolution in the range direction, and the resolution within the ground plane can be estimated by projecting the range resolution to the ground considering the incidence angle. We can conclude that the range resolution can be improved by decreasing the pulse duration τ. The τ cannot be too small to generate large enough transmitted energy. As will be shown in the next section, in pulse compression systems, the range resolution Δr can be improved by increasing the bandwidth which makes the very high resolution possible.

Let λ be the wavelength of the transmitted pulses and L be the antenna size, we consider the azimuth resolution of the radar system. For a real aperture Side-Looking Airborne Radar (SLAR), the radar beam covers the angle λ/L in the azimuth direction [44], and different targets cannot be located in the same beam to be resolvable. Therefore, we can derive the azimuth resolution of this system as:

$$\Delta az = R_s \frac{\lambda}{L} \tag{2.3}$$

where R_S denotes the slant range, i.e. the range between the phase center (antenna) and the target. It can be seen from (2.3) that better azimuth resolution can be achieved by increasing the antenna size L. However, in practice, L has to be very large to induce fine azimuth resolution. For example, the antenna length has to be at least 240 m to achieve the 1 m azimuth resolution with the X-band signal ($\lambda = 0.03m$) and 8 km distance to the target. Therefore, the azimuth resolution is not fine enough for distinguishing different targets in practical SAR/GMTI.

This difficulty can be overcame by utilising SAR with the small antenna to synthesise a large virtual aperture. We take a SAR system in the conventional stripmap mode depicted in Fig. 2.3 as an example to give an insight into the azimuth resolution of SAR systems. The antenna and pointing direction are fixed while the platform moves along a path. The monitored region is thus

shaped like a strip pattern on the ground. It can be seen from Fig. 2.3 that a large virtual aperture
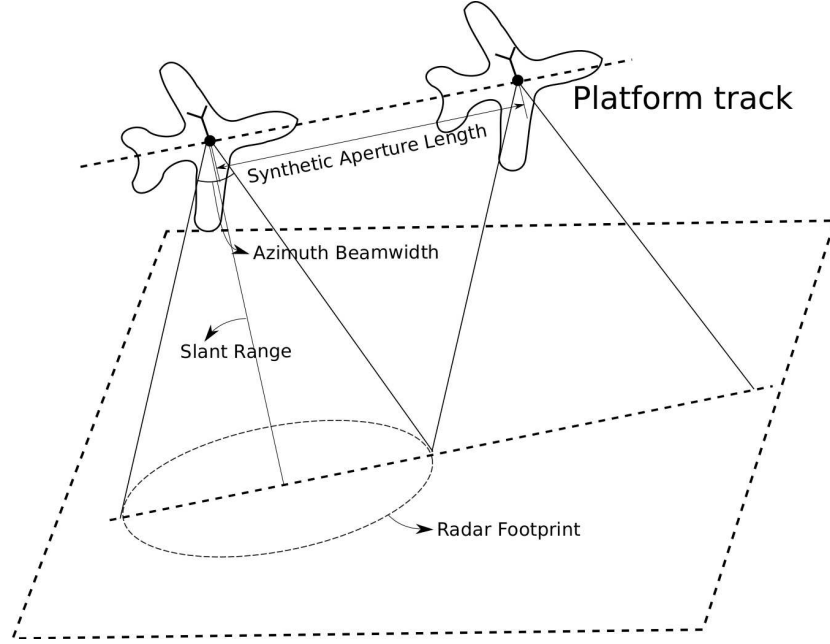
Figure 2.3: The SAR system in stripmap mode.

can be synthesised with the moving platform. However, the synthesised aperture dimension is limited as the synthetic aperture length cannot be larger than the azimuth length of the footprint $R_s\lambda/L$ to keep the target in the monitored range. Given that the beam width of SAR is half that of the real antenna [45], the azimuth resolution can be derived as:

$$\Delta az = R_s \frac{\lambda}{2L_{syn}} = R_s \frac{\lambda}{(2\lambda R_s/L)} = \frac{L}{2} \tag{2.4}$$

where L_{syn} denotes the maximum synthetic aperture length $R_s\lambda/L$ based on Fig. 2.3.

This expression (2.4) proves that smaller antenna can lead to finer resolution within the stripmap SAR. Compared to the conclusion we drew from (2.3), this stands as an opposite conclusion. Practically even larger synthetic aperture (finer azimuth resolution) can be generated by switching the SAR working mode to spotlight (Fig. 2.1) for which the beam direction is steered to focus on the same region. The spotlight mode thus further increases the azimuth resolution by sacrificing the monitoring coverage. Given the decent spatial resolution that spotlight SAR can achieve, this mode is a suitable setting for SAR-based GMTI missions.

Pulse Compression and Refined Range Resolution

In this section we describe how the pulse compression technique is used in SAR systems to significantly improve the range resolution. We start by introducing the motivation of pulse compression techniques with which the Radar propagates the chirp signal, i.e. the linear frequency modulated (LFM) Radar signal. Recalling that the range resolution of a SAR system is directly associated with the pulse duration τ, to guarantee the fine enough range resolution for the SAR processing and further GMTI tasks, the transmitted pulse duration is thus limited. However, a SAR system often requires a long transmitted pulse to generate large enough transmitted energy (considering the requirement on SNR). This contradiction is preventing the SAR system from achieving fine range resolution.

Within this context, pulse compression techniques are employed to meet this challenge. In typical SAR systems, the widely used LFM signal can ensure fine range resolution while retaining narrow pulses. It is working by transmitting a coded long pulse with large time-bandwidth product and compressing the signal during the processing. The effective pulse length after processing can be very small to have fine range resolution. The coding process is also called chirping in the SAR processing.

The transmitted LFM signal is defined as:

$$s_1(t) = \mathbf{rect}(\frac{t}{\tau_l}) \exp\left(j2\pi(f_0 t + \frac{K}{2}t^2) \right) \tag{2.5}$$

where $\mathbf{rect}(t)$ is a rectangular window function that is 0 out of $[-1/2, 1/2]$, τ_l is the LFM pulse duration, f_0 denotes the carrier frequency in Hz, K represents the linear chirp frequency rate in Hz/s.

It can be seen from (2.5) that the instantaneous frequency of $s_1(t)$ with time is:

$$f_{ins}(t) = \frac{d\{2\pi(f_0 t + \frac{K}{2}t^2)\}}{2\pi dt} = f_0 + Kt \tag{2.6}$$

which means that the frequencies of the original signal have been linearly modulated as depicted in Fig. 2.4. The pulse bandwidth of the LFM signal is the frequency span $B = K\tau_l$.

The compression step can be demonstrated by processing the returned data using the matched filtering technique [46]. For a target with the range distance r, the reflected signal from the target
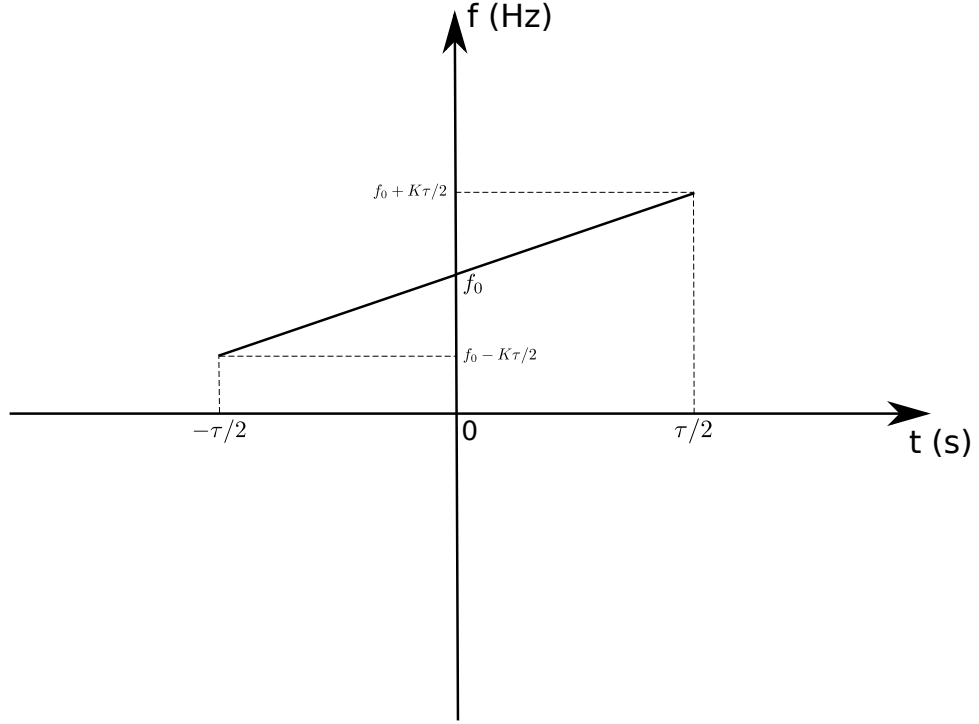
Figure 2.4: The instant frequency of the LFM pulse.

regardless of its reflectivity can be written as:

$$
\begin{aligned}
s_2(t) &= s_1\left(t - \frac{2r}{c}\right) \\
&= \mathbf{rect}\left(\frac{t - 2r/c}{\tau_l}\right) \exp\left(j2\pi(f_0(t - \frac{2r}{c}) + \frac{K}{2}(t - \frac{2r}{c})^2)\right)
\end{aligned}
\tag{2.7}
$$

which is the delayed version of (2.5).

After removing the carrier frequency f_0, the received signal (2.7) can be expressed as:

$$
s_{rece}(t) = \mathbf{rect}\left(\frac{t - 2r/c}{\tau_l}\right) \exp\left(-j4\pi f_0(\frac{r}{c})\right) \exp\left(j\pi K(t - \frac{2r}{c})^2)\right)
\tag{2.8}
$$

To give an insight into the range resolution after processing, the range compression of (2.8) can be done in the temporal or frequency domain. Particularly this processing can be realised either as convolution in the time domain or as multiplication in the frequency domain. Here we first derive this processing in the time domain with details as a showcase. The reference signal $s_{ref}(t)$ to be convolved with (2.8) is defined as:

$$
s_{ref}(t) = \mathbf{rect}(\frac{t}{\tau_l}) \exp\left(-j\pi K t^2\right)
\tag{2.9}
$$

14

and the resulting signal after the convolution can be derived as:

$$
\begin{aligned}
s_{compressed}(t) &= \int \exp\left(-j4\pi f_0(\tfrac{r}{c})\right) \exp\left(j\pi K(t - s - \tfrac{2r}{c})^2\right) \exp\left(-j\pi K s^2\right) \\
&\quad \mathbf{rect}\left(\frac{t - s - 2r/c}{\tau_l}\right) \mathbf{rect}\left(\frac{s}{\tau_l}\right) ds \\
&= \exp\left(-j4\pi f_0(\tfrac{r}{c})\right) \exp\left(j\pi K(t - \tfrac{2r}{c})^2\right) \int \exp\left(-j\pi 2K s(t - \tfrac{2r}{c}))\right) \\
&\quad \mathbf{rect}\left(\frac{t - s - 2r/c}{\tau_l}\right) \mathbf{rect}\left(\frac{s}{\tau_l}\right) ds \\
&= \exp\left(-j4\pi f_0(\tfrac{r}{c})\right) \int \exp\left(-j\pi 2K(s - (t - \tfrac{2r}{c})/2)(t - \tfrac{2r}{c}))\right) \\
&\quad \mathbf{rect}\left(\frac{t - s - 2r/c}{\tau_l}\right) \mathbf{rect}\left(\frac{s}{\tau_l}\right) ds
\end{aligned}
\tag{2.10}
$$

Based on the rectangular window functions, we have that:

$$
\begin{aligned}
-\frac{\tau_l}{2} &\leq s \leq \frac{\tau_l}{2} \\
t - \frac{2r}{c} - \frac{\tau_l}{2} &\leq s \leq t - \frac{2r}{c} + \frac{\tau_l}{2}
\end{aligned}
\tag{2.11}
$$

From the second formula in (2.11) we have that $s - \frac{\tau_l}{2} \leq t - \frac{2r}{c} \leq s + \frac{\tau_l}{2}$. Then we can easily have $-\tau_l \leq t - \frac{2r}{c} \leq \tau_l$ which is essentially a window function $\mathbf{rect}(\frac{t - 2r/c}{2\tau_l})$.

Combining the two formulas in (2.11) gives us:

$$
-\frac{\tau_l}{2} + \frac{|t - 2r/c| + t - 2r/c}{2} \leq s \leq \frac{\tau_l}{2} + \frac{t - 2r/c - |t - 2r/c|}{2}
\tag{2.12}
$$

By considering the $t - 2r/c$ term, (2.12) can be represented as the window function $\mathbf{rect}(\frac{s - (t - 2r/c)/2}{\tau_l - (|t - 2r/c|)})$.

Now the equation (2.10) becomes:

$$
\begin{aligned}
s_{compressed}(t) &= \exp\left(-j4\pi f_0(\tfrac{r}{c})\right) \int \exp\left(-j\pi 2K(s - (t - \tfrac{2r}{c})/2)(t - \tfrac{2r}{c}))\right) \\
&\quad \mathbf{rect}\left(\frac{t - 2r/c}{2\tau_l}\right) \mathbf{rect}\left(\frac{s - (t - 2r/c)/2}{\tau_l - (|t - 2r/c|)}\right) ds
\end{aligned}
\tag{2.13}
$$

Since the equation (2.13) is in the form of the Fourier transform of the a rectangular window,

$s_{compressed}(t)$ can be rewritten as:

$$s_{compressed}(t) = \exp\left(-j4\pi f_0(\frac{r}{c})\right) \mathbf{sinc}\left(K\tau_l(t - \frac{2r}{c})\right) \tag{2.14}$$

where the sinc function is in the normalised form ($\mathbf{sinc}(x) = \dfrac{\sin(\pi x)}{\pi x}$). Note that the target is compressed on the t-axis in (2.14), and t is thus linearly dependent to the target range. The processed signal $s_{compressed}(t)$ represents the range compressed data. The effective pulse length of $s_{compressed}(t)$ is $\dfrac{1}{K\tau_l} = \dfrac{1}{B}$ based on the -3 dB point of this sinc function, and $|t - 2r/c| \ll \tau_l$ holds.

With this effective pulse length, considering (2.2), the range resolution of the SAR system using this pulse compression is

$$\Delta r = \frac{c}{2K\tau_l} = \frac{c}{2B} \tag{2.15}$$

We can conclude that the range resolution is proportional to $1/B$, and the range resolution can thus be improved by increasing $B = K\tau_l$. It can be seen from (2.14) that a point target is imaged as a pattern, and this sinc function is known as the ideal SAR Point Spread Function (PSF).

In practice, one important property of a real Radar system is the Time-Bandwidth Product (TBP) $B\tau_l$. The TBP is coded to be very large which leads to a very large compression ratio, i.e. the ratio of the original pulse length τ_l to the effective pulse length after compression. To explain this, we can derive that the compression ratio of the original pulse length τ_l over the compressed pulse length $1/(K\tau_l)$ as:

$$\tau_l/(\frac{1}{K\tau_l}) = K\tau_l^2 = B\tau_l \tag{2.16}$$

which equals to the TBP. This ratio exactly measures the capability of the SAR system to improve the range resolution. Therefore the linear frequency modulation significantly improves the SAR range resolution which is beneficial to both SAR imaging and GMTI.

Note that the fast-time variable t in the compressed signal (2.14) corresponds to the range variable of the target. The range imaging has been effected in (2.14), and the variable substitution $r' \mapsto t - 2r^{(o)}/c$ can be used to get the expression:

$$s_{compressed}(r') = \exp\left(-j4\pi f_0(\frac{r}{c})\right) \mathbf{sinc}\left(K\tau_l(r' - \frac{2u}{c})\right) \tag{2.17}$$

16

where r' is the scaled range variable, $r^{(o)}$ denotes the distance from the scene origin to the platform, and $u = r - r^{(o)}$ represents the differential range variable that can help calibrate the phase of the spectrum. It can be seen that this equation (2.17) stands for the range imaging of this target.

Range Signal Model in the Frequency Domain

By Fourier transforming (2.17) based on the scaled range variable r' and compensating the constant complex term (the detailed method is described in the signal modelling section), we can formulate the generic normal form of the processed signal in the frequency domain as:

$$s_{norm}(f_r) = \exp\left(-j4\pi f_r \frac{u}{c}\right) \tag{2.18}$$

which represents the fast-time signal of a point scatterer in the frequency domain, and f_r is the range frequency after phase calibration.

We now consider the range processing in the frequency domain. The convolution of $s_{rece}(r')$ and $s_{ref}(r')$ is equivalent to the multiplication of $s_{rece}(f_r)$ and $s_{ref}(f_r)$, where f_r denotes the range frequency, $s_{rece}(f_r)$ is the Fourier transformed $s_{rece}(r')$, and $s_{ref}(f_r)$ is the Fourier transformed $s_{ref}(r')$. The practical implementation of this convolution is usually realised in the frequency domain. To explain this, let $\sigma_f(f_r)$ be the frequency-dependent reflectivity of the target, based on (2.7), the received signal in the frequency domain can be written as:

$$
\begin{aligned}
s_3(f_r) &= \sigma_f(f_r)\mathcal{F}\Big\{s_2(r')\Big\} \\
&= \sigma_f(f_r)\mathcal{F}\Big\{s_1(r' - \frac{2u}{c})\Big\} \\
&= \sigma_f(f_r)s_1(f_r)\exp\left(-j4\pi f_r \frac{u}{c}\right)
\end{aligned}
\tag{2.19}
$$

where $s_1(t)$ is the transmitted LFM signal, $u = r - r^{(o)}$, and $\mathcal{F}$ represents the Fourier transform.

After cancelling out $s_1(f_r)$ with the inverse filter, the processed signal in the frequency domain can be modelled as:

$$s_3(f_r) = \sigma_f(f_r)\exp\left(-j4\pi f_r \frac{u}{c}\right) \tag{2.20}$$

which is consistent with the generic normal form in (2.18). The range compression can be

subsequently realised by performing the inverse Fourier transform on this preprocessed signal. Therefore, we can conclude that the range imaging can be achieved through the Fourier transform, filtering, and the inverse Fourier transform [47].

SAR Signal Modelling

In practice, the engineers usually process SAR tasks by considering the system model (2.20) in the frequency domain. It can be concluded from (2.15) that fine SAR resolution calls for a very large bandwidth, and it brings a significant burden on the A/D converters. A practical solution to reduce the data rates starts by processing the time representation with the deramping technique.

In this section, we first introduce the deramping method based on the received signal (2.8) and present the typical processing procedures. In particular, we deramp the received signal, introduce the target reflectivity, remove the undesirable phase, consider the azimuth sampling, discretize the data, and finally identify the SAR signal model which is consistent with (2.20).

Given the received signal (2.8), the deramping process is converting the linear frequency modulated signal to a flat frequency signal. Particularly, the received signal $s_{rece}(t)$ is mixed with the complex conjugated waveform of the the transmitted ramp (calibrated by the scene origin):

$$
\begin{aligned}
s_{deramp}(t) &= s_{rece}(t) \exp\left(-j\pi K(t - \frac{2r^{(o)}}{c})^2\right) \\
&= \mathbf{rect}\left(\frac{t - 2r/c}{\tau_l}\right) \exp\left(-j4\pi f_0(\frac{r}{c})\right) \exp\left(j\pi K \frac{4(r^2 - r^{(o)2})}{c^2}\right) \exp\left(-j4\pi K \frac{ut}{c}\right)
\end{aligned}
$$

(2.21)

which is known as the deramped signal in time domain [48].

It can be seen that the instantaneous frequency of the deramped signal is $-2Ku/c$ and the signal is a single-tone sinusoid that has a flat frequency spectrum. Therefore, the instantaneous frequency indicates the range distance of the reflector. The bandwidth of the signal is reduced after deramping and the sampling rate can now be lower. By further considering the target reflectivity σ_0, based on (2.21), the deramped signal (2.21) can be rewritten as:

$$
\begin{aligned}
s_4(t) = \sigma_0 \mathbf{rect}\left(\frac{t - 2r/c}{\tau_l}\right) \exp\left(-j4\pi K \frac{ut}{c}\right) \\
\exp\left(-j4\pi f_0(\frac{r}{c})\right) \exp\left(j\pi K \frac{4(r^2 - r^{(o)2})}{c^2}\right)^{\cdot}
\end{aligned}
$$

(2.22)

In (2.22), the phase term $\exp\left(-j4\pi f_0 r/c\right)\exp\left(j\pi K4(r^2 - r^{(o)2})/c^2\right)$ is undesired which is termed the Residual Video Phase (RVP). This term can be approximated in the other domain. Specifically, by performing the inverse Fourier transform along t based on (2.22), we have that:

$$s_5(r_{deramp}) = A_0\mathbf{PSF}\left(r_{deramp} - \frac{2Ku}{c}\right)\exp\left(j\frac{4\pi r_{deramp}r}{c}\right)$$
$$\exp\left(-j4\pi f_0(\frac{r}{c})\right)\exp\left(j\pi K\frac{4(r^2 - r^{(o)2})}{c^2}\right) \tag{2.23}$$

where A_0 denotes a nominal complex constant (scaled target reflectivity), and $\mathbf{PSF}$ is the point spread function in the frequency domain for pulse compression (the Fourier transform of the $\mathbf{rect}$ window which is a sinc function).

As the $\mathbf{PSF}$ is a sinc function and its symmetrical center is $2Ku/c$, the RVP term can thus be compensated with the approximation $r_{deramp} \approx 2K(r - r^{(o)})/c$. After removing the RVP term, (2.23) becomes:

$$s_5(r_{deramp}) \approx A_0\mathbf{PSF}\left(r_{deramp} - \frac{2Ku}{c}\right)\exp\left(j\frac{4\pi r_{deramp}r}{c}\right) \tag{2.24}$$

which stands for the range imaging of this target. Based on the discussions in the last section, we can conclude that the multiplication by the deramping term is equivalent to the Fourier transform and data filtering, and a subsequent inverse Fourier transform will induce the range compressed target image.

By comparing (2.24) to the aforementioned range imaging equation (2.17), the variable substitution $r' \mapsto r_{deramp}/K$ can be used to achieve the consistency. The signal (2.24) can then be rewritten as:

$$s_5(r') \approx A_0\mathbf{PSF}\left(K(r' - \frac{2u}{c})\right)\exp\left(j\frac{4\pi Kr'r}{c}\right) \tag{2.25}$$

in which $u = r - r^{(o)}$ is the differential range. This expression is consistent with the format of (2.17).

To derive the similar representation like (2.20), we can Fourier transform (2.25) to have:

$$s_6(f_r) = \sigma_f(f_r)\mathbf{rect}\left(\frac{f_r - 2Kr/c}{K\tau_l}\right)\exp\left(-j4\pi\frac{f_r u}{c}\right) \tag{2.26}$$

where $\sigma_f(f_r)$ accounts for the frequency-dependent reflectivity of the target, and the the window

function can be deskewed with $r \approx r^{(o)}$ at the scene center [49].

Furthermore, if the duration of the chip is large enough, the window function in (2.26) can be taken as a constant and we have the updated system model as:

$$s_6(f_r) = \sigma_f(f_r) \exp\left(-j4\pi \frac{f_r u}{c}\right) \tag{2.27}$$

which can be directly used as the entries in the (2.20).

If we make the stop-and-go assumption which assumes that the platform is static within the round-trip of the transmitted signal, the system model (2.27) can be expressed with the azimuth time. The phase history is the collection of the received data which can be represented as:

$$s_{ph}(f_r, \tau) = \sigma_f(f_r) w_a(\tau) \exp\left(-j4\pi \frac{f_r u(\tau)}{c}\right) \tag{2.28}$$

where $w_a(\tau)$ denotes the antenna pattern and energy loss with azimuth time τ, and $u(\tau)$ denotes the differential range (target-antenna distance minus origin-antenna distance) with τ.

Therefore, the SAR signal model can be simplified in the range frequency and azimuth time domain as:

$$s_{2d}(f_r, \tau) = A(f_r, \tau) \exp\left(-j\frac{4\pi f_r u(\tau)}{c}\right) \tag{2.29}$$

where $A(f_r, \tau)$ denotes the nominal frequency-dependent target reflectivity with (f_r, τ) and it represents the target signature.

After the discretization process, the SAR phase history can be formulated as:

$$s_{2d}(f_k, \tau_n) = A(f_k, \tau_n) \exp\left(-j\frac{4\pi f_k u(\tau_n)}{c}\right) \tag{2.30}$$

where $\{f_k | k = 1, 2, ..., K\}$ denotes the range frequencies, and $\{\tau_n | n = 1, 2, ..., N\}$ is the discrete slow time with pulse number n.

Based on (2.30), under the multi-channel SAR system as in Fig. 2.1, we consider the signal model of a target with the generic frequency-dependent reflectivity $\sigma(f_k, \tau_n)$ (associated with the Radar Cross Section, antenna gain and beam pattern). The received signal for the $i-$th antenna of

this target is a $K \times N$ complex matrix which can be modelled as:

$$\mathbf{Y}_i(f_k, \tau_n) = \sigma(f_k, \tau_n) \exp\left(-\frac{j4\pi f_k u_i(\tau_n)}{c}\right) \quad (2.31)$$

where $u_i(\tau_n)$ represents the differential range $r_i^{(t)}(\tau_n) - r_i^{(o)}(\tau_n)$ with which the signal phases are calibrated so that the scene origin has zero phase (for scene origin $u_i(\tau_n) = r_i^{(t)}(\tau_n) - r_i^{(o)}(\tau_n) = 0$) [50].

In (2.31), the frequency-dependent reflectivities $\sigma(f_k, \tau_n)$ can be assumed to be constant for isotropic scatterers [51]. Given that $\mathbf{X}_c \in \mathbb{C}^{M \times L}$ is the collection of the reflectivities from all targets (both static and moving) in the scene with the constant antenna gain for the channels, with the Born approximation that the scatterings are driven by the incident beam [52], the received phase history can be assembled by accumulating the reflected signals from all reflectors:

$$\mathbf{Y}_i(f_k, \tau_n) = \sum_{m=1}^{M} \sum_{l=1}^{L} \mathbf{X}_c(m, l) \exp\left(-\frac{j4\pi f_k u_{mli}(\tau_n)}{c}\right) \quad (2.32)$$

where $u_{mli}(\tau_n)$ represents the differential range with respect to the reflector at (m, l). The signal model (2.32) can be rewritten in the matrix-vector form as:

$$\mathbf{Y}_i = \Phi_F(\mathbf{X}_c) \quad (2.33)$$

where $\mathbf{Y}_i \in \mathbb{C}^{K \times N}$ is the 2-D phase history for the $i-$th channel and Φ_F denotes the forward operator that projects the reflectivities to the phase history.

The classical SAR imaging approaches originate from the attempt to approximate the pseudo inverse of the forward projection operator [53]. More generally, for small sub-apertures the distance measure $u_{mli}(\tau_n)$ can incorporate velocities. To avoid ambiguities, we denote $\Phi_F^{\mathbf{V}}$ and Φ_F^0 as the forward operators for all targets with the velocity map described by $\mathbf{V} = (\mathbf{V}^{(x)}, \mathbf{V}^{(y)}, \mathbf{V}^{(z)})$ and the static scene respectively. The $\Phi_B^{\mathbf{V}}$ and Φ_B^0 are the inverse operators of $\Phi_F^{\mathbf{V}}$ and Φ_F^0 which project from the received signals to reflectivities. Further details of the velocity-coded operators will be discussed in Chapter 5.

2.3   Sparsity and Compressed Sensing

Sparse representation, which is closely associated with the compressed sensing theory, emerged with the demand in signal processing field to deal with increasingly complicated sensing systems and large amounts of data. For a long time sensors played a vital role in pervasive sensing and processing systems, especially in the battlefield surveillance and intelligence gathering. The importance of signal processing is due to its tremendous impact on the full data processing chain of extracting, processing, and interpreting the raw data. Shannons classical theory [33] reported that if the sampling rate was at least twice the highest frequency of the original signal, the signal could be recovered. Numerous advanced signal processing algorithms were than developed which significantly stimulated the development of modern sensing systems, and large expenditures had been made to facilitate the development of persistent and efficient sensing. However, the large amount of resource consumption and increasingly sophisticated algorithms, in terms of resource-limited sensor nodes and massive data stream, bring new challenges in the modern sensing systems. This has led in recent years to the exploration of a number of new techniques to efficiently acquire and process the data.

With respect to dealing with massive data processing, we often make use of sparse representation techniques to compress the data, such as the well-known JPEG and MP3 standards [54] which can be traced as far back as 1990s. In the early 2000's Vetterli, Marziliano and Blu proposed the rate of innovation with which a signal coded by k parameters can be reconstructed with only 2k samples [55]. Subsequently, Candès, Romberg, Tao and Donoho made the founding contributions in compressed sensing theory around 2005 [36] [35] [56]. The revolutionary CS theory proposes to directly acquire the data in the compressed form instead of conventionally first sampling the signal at a high rate and then compressing the data. It therefore establishes a new efficient sensing mechanism. Compressed sensing impressed the industry with the potential to break the Nyquist theorem. It then attracted significant attention all around the world and related applications were developed rapidly. Generally the capability of CS in the signal reconstruction enables a number of innovative explorations in various applications, such as single-pixel camera, Radar, and MRI. More recently, Candès extended the techniques to the field of super resolution [57] in 2012. Main theoretical contributions in this area so far focused on how to reconstruct the original signal, how many measurements are needed and how to realise the sensing schemes.

2.3.1 Compressed Sensing Basics

Observation Model and Signal Sparsity

Compressed sensing is directly related to solving inverse problems in linear sensing systems, i.e. the signal reconstruction task with acquired samples. Particularly, suppose that the signal of interest is $\mathbf{x} \in \mathbb{R}^N$, the observation model can be formulated as:

$$\mathbf{y} = \Phi \mathbf{x} \tag{2.34}$$

where $\mathbf{y} \in \mathbb{R}^M$ represents the vector of samples, M denotes the number of samples, and $\Phi \in \mathbb{R}^{M \times N}$ ($M \ll N$ for typical undersampling) is the sensing matrix which projects from the signal to samples. The signal reconstruction task is to implement the inverse projection and estimate the signal $\mathbf{x}$ based on the samples $\mathbf{y}$. Specifically compressed sensing is leveraging the prior information of the signal $\mathbf{x}$ to reduce the required number of samples M in the reconstruction. The required M can be much lower than the classical Nyquist-Shannon sampling rate.
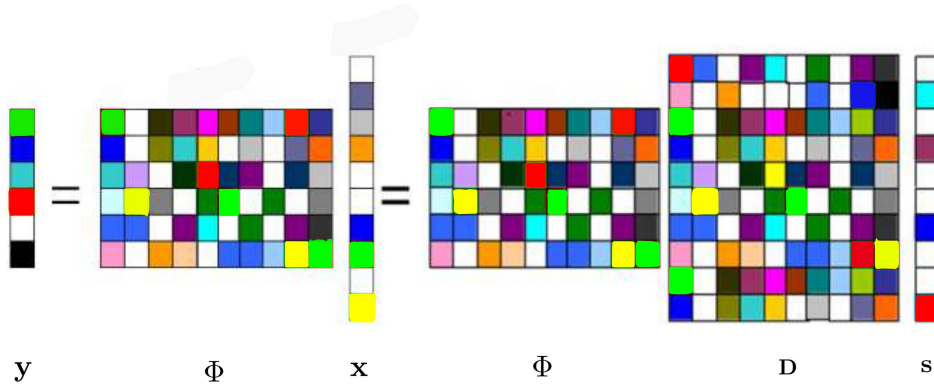
Figure 2.5: The observation model.

The underlying signal sparsity is the prior information used in CS that can be interpreted based on the decomposition of $\mathbf{x}$. Given a dictionary matrix $\mathbf{D} \in \mathbb{R}^{N \times N}$, the signal $\mathbf{x}$ lives in the span of the dictionary elements ($\mathbf{x} = \sum_{i=1}^{N} \mathbf{D}_i s_i$) where N stands for the number of the dictionary atoms and $\{\mathbf{D}_i \in \mathbb{R}^N | i = 1, 2, ..., N\}$ is the basis of $\mathbf{x}$. The equivalent matrix form of this expression is:

$$\mathbf{x} = \mathbf{D}\mathbf{s} \tag{2.35}$$

where $\mathbf{s}$ is the weight vector. With this model the signal $\mathbf{x}$ is said to be k-sparse under this basis

if **s** contains only k non-zero entries ($k \ll N$). The equation (2.35) with the k-sparse **s** stands for the sparse representation of the signal **x**. As only a small dimension k of information is valid, this property of sparse representation is widely exploited in signal compression applications. For example, the JPEG image format keeps only the largest coefficients under specific basis functions [54].

With (2.35), the observation model (2.34) can be rewritten as:

$$\mathbf{y} = \Phi\mathbf{D}\mathbf{s} = \mathbf{A}\mathbf{s} \tag{2.36}$$

where $\mathbf{A} = \Phi\mathbf{D} \in \mathbb{R}^{M \times N}$ is the projection matrix.

The overall observation model can be visualised in Fig. 2.5 in which the signal **x** is decomposed based on a dictionary **D**.

CS Properties

The projections between **y**, **x** and **s** lead to significant dimension reduction in the measurements which are depicted in Fig. 2.6. It can be seen that there exist indefinite solutions for this underdetermined system. Compressed sensing theory proves that, if **x** is approximately sparse under specific basis, the signal can be recovered under certain conditions on A.
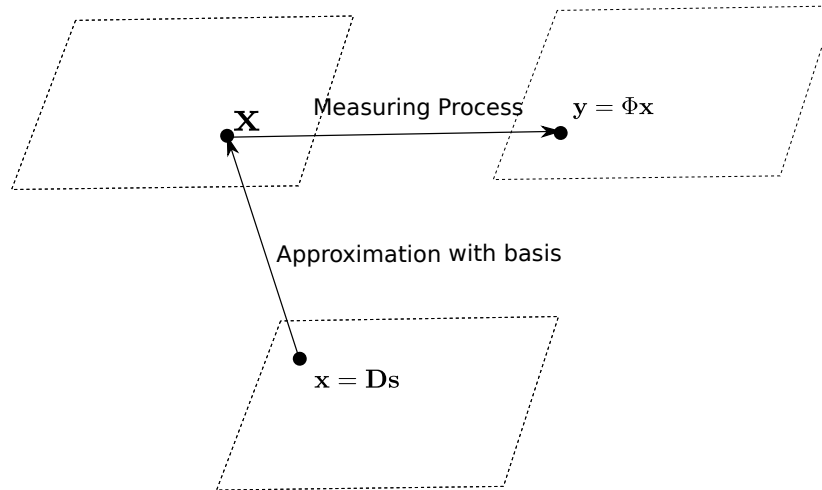
Figure 2.6: The projections between **y**, **x** and **s**

The Restricted Isometry Property (RIP) [58] was introduced to identify sufficient conditions for which the matrix matrix A allows accurate sparse reconstruction. It is defined as:

Definition 1 *If there exists a constant $\delta_k \in (0, 1)$ such that*

$$(1 - \delta_k)\|\boldsymbol{s}\|^2 \leqslant \|\boldsymbol{As}\|^2 \leqslant (1 + \delta_k)\|\boldsymbol{s}\|^2 \tag{2.37}$$

holds for all k-sparse $\boldsymbol{s}$, then the matrix $\boldsymbol{A}$ follows the RIP condition of order k.

The RIP condition allows the matrix **A** to project **s** while approximately preserving the Euclidean distance of pairs of points. Suppose we have two different k/2-sparse vectors $\mathbf{s}_1$ and $\mathbf{s}_2$, the measurements $\mathbf{y}_1$ and $\mathbf{y}_2$ must be different to be able to distinguish them. This means that any $\mathbf{s}_1 - \mathbf{s}_2$ cannot live in the nullspace of **A**. As $\mathbf{s}_1 - \mathbf{s}_2$ can be k-sparse, this essentially prevents k-sparse s from living in the nullspace of **A**. In general the smaller δ_k leads to better signal reconstruction. It has been shown that, if **A** obeys the RIP with the appropriate δ_k, there exist a number of algorithms to reconstruct the sparse signal from noisy measurements [59]. The design of **A** is thus crucial in sparse reconstruction problems. Although it is difficult to verify the RIP condition for matrices, it has been shown that random Gaussian, Bernoulli, and partial Fourier matrices obey the RIP with high probabilities [60].

A more practical recovery guarantee criteria for the matrix design is based on the coherence [61] [62] [63]. The coherence of a matrix **A** is defined as:

Definition 2 *The mutual coherence of a matrix is the maximised cross-correlations between the columns $\boldsymbol{A}_i$, $\boldsymbol{A}_j$ of $\boldsymbol{A}$.*

$$\mu(\boldsymbol{A}) = \max_{1 \leq i,j \leq N} \frac{|\boldsymbol{A}_i^H \boldsymbol{A}_j|}{\|\boldsymbol{A}_i\|_2 \|\boldsymbol{A}_j\|_2} \tag{2.38}$$

Particulary $\mu(\mathbf{A})$ is lower bounded by $\sqrt{(N-M)/M/(N-1)}$ with $N > M$ [64]. This lower bound is known as the Welch bound that can be approximated with $M^{-1/2}$ [65]. The mutual coherence is widely used in compressed sensing field as a measure to reflect the tractability of the signal reconstruction problem. In general the lower mutual coherence leads to less required number of signal measurements.

It has been shown in [66] [67] that exact reconstruction can be realised with a number of reconstruction algorithms when

$$k < \frac{\mu^{-1}(\mathbf{A}) + 1}{2} \tag{2.39}$$

which reflects the crucial role of mutual incoherence in compressed sensing problems.

We have presented some important features on the projection matrix $\mathbf{A}$ in compressed sensing. In addition, it has been shown in a number of investigations that the k-sparse signal can be reconstructed with only a constant times of the sparsity level [68] [69], i.e. $M = \alpha k$ where $\alpha > 1$ is a constant. For example, in [70] [59] the authors presents a lower bound of M:

Theorem 1 *If $M \times N$ matrix $\mathbf{A}$ satisfies the the RIP of order 2k with $\delta_k \in (0, \frac{1}{2}]$, then*

$$M \geqslant Ck \log \left(\frac{N}{k} \right) \tag{2.40}$$

where $C = \frac{1}{2} log(\sqrt{24} + 1) \approx 0.28$.

From the information theory perspective, these investigations assert that αk measurements are enough to preserve all the information in $\mathbf{x}$.

Reconstruction Methods

Based on the aforementioned signal acquisition process and CS properties, the signal reconstruction for (2.36) can be realised via an optimisation problem:

$$\hat{\mathbf{s}} = \underset{\mathbf{s}}{\operatorname{argmin}} \|\mathbf{s}\|_0 \quad s.t. \quad \mathbf{y} = \mathbf{A}\mathbf{s} \tag{2.41}$$

in which $\| \cdot \|_0$ is the $L0$ pseudo-norm operator that counts the non-zero elements. Specifically the Lp pseudo-norm of a vector $\mathbf{s}$ is defined as:

$$\|\mathbf{s}\|_p = \left(\sum_{i=1}^{N} |\mathbf{s}_i|^p \right)^{1/p} \tag{2.42}$$

where $p \geqslant 1$. The infinite norm $\|\mathbf{s}\|_\infty$ is defined as the largest absolute value of the elements.

Furthermore, if the sparsity level is constrained to be k, the approximation of $\mathbf{s}$ can be realised through:

$$\hat{\mathbf{s}} = \underset{\mathbf{s}}{\operatorname{argmin}} \|\mathbf{y} - \mathbf{A}\mathbf{s}\|_2 \quad s.t. \quad \|\mathbf{s}\|_0 \leqslant k \tag{2.43}$$

As practical observation systems contain non-negligible noise, the model (2.36) can be rewritten

as:

$$\mathbf{y} = \mathbf{A}\mathbf{s} + \mathbf{n} \tag{2.44}$$

where $\mathbf{n}$ denotes the noise and it obeys the constraint:

$$\|\mathbf{n}\|_2 \leqslant \varepsilon \tag{2.45}$$

The natural model to reconstruct the signal with the presence of the noise then becomes:

$$\hat{\mathbf{s}} = \underset{\mathbf{s}}{\arg\min} \|\mathbf{s}\|_0 \quad s.t. \quad \|\mathbf{y} - \mathbf{A}\mathbf{s}\|_2 \leqslant \varepsilon \tag{2.46}$$

With the well-known Lagrange multiplier method, (2.46) can be reformulated as:

$$\hat{\mathbf{s}} = \underset{\mathbf{s}}{\arg\min} \|\mathbf{y} - \mathbf{A}\mathbf{s}\|_2 + \lambda \|\mathbf{s}\|_0 \tag{2.47}$$

where the λ is the Lagrange multiplier parameter to control the tradeoff between data fidelity and signal sparsity.

As these $L0$ regularised optimisations are non-convex and computationally NP-hard, solving them directly becomes intractable. On the contrary, the $L1$ pseudo-norm optimization problem is more tractable and it has an analytical solution. The use of $L1$ pseudo-norm can be traced back to the LASSO method in statistics [71] [72]. With sufficient signal sparsity, a number of literatures have shown that by employing the convex relaxation of $L0$-minimisation, i.e. the $L1$-minimisation, the same performance can be achieved [73] [74]. The $L1$ pseudo-norm thus represents a practical measure for signal sparsity in various of applications.

Therefore, two practical optimisation models for solving the sparse approximation problem can be derived:

$$\hat{\mathbf{s}} = \underset{\mathbf{s}}{\arg\min} \|\mathbf{s}\|_1 \quad s.t. \quad \|\mathbf{y} - \mathbf{A}\mathbf{s}\|_2 \leqslant \varepsilon \tag{2.48}$$

and

$$\hat{\mathbf{s}} = \underset{\mathbf{s}}{\arg\min} \|\mathbf{y} - \mathbf{A}\mathbf{s}\|_2 \quad s.t. \quad \|\mathbf{s}\|_1 \leqslant \widetilde{\varepsilon} \tag{2.49}$$

27

where ε denotes the noise level, and $\widetilde{\varepsilon}$ is controlling the sparsity level.

Again with the Lagrange multiplier, (2.49) can be rewritten as the basis pursuit denoising (BPDN) problem:

$$\hat{\mathbf{s}} = \underset{\mathbf{s}}{\operatorname{argmin}} \|\mathbf{y} - \mathbf{A}\mathbf{s}\|_2 + \widetilde{\lambda}\|\mathbf{s}\|_1 \qquad (2.50)$$

where $\widetilde{\lambda}$ is the positive parameter to be tuned.

The history of greedy algorithms can be traced back to several decades ago [75]. The greedy strategies in general compute a local solution in each step and eventually output an approximated global solution. There exist a number of algorithms with the greedy mechnism to reconstruct sparse signals with the aforementioned sensing systems. [76] [77] [78]. These algorithms are normally designed in iterative forms. Widely used algorithms include the matching pursuit (MP) [76] and orthogonal matching pursuit (OMP) [77]. The matching pursuit selects a specific atom from the dictionary to best match the updated residual in each iteration, while the orthogonal matching pursuit orthogonalises the residual and selected atoms during each iteration. A number of research efforts have been made to further improve the MP and OMP [79]. For example the regularised OMP (ROMP) reconstructs sparse signals with noisy measurements under RIP [80], and the compressive sampling matching pursuit (CoSaMP) algorithm employs the pruning approach into the iterative updates [81]. Other variants include the stage-wise orthogonal matching pursuit (StOMP) [82] to implement the algorithm with three stages, i.e. threholding, selecting and projecting, and sparsity adaptive matching pursuit (SAMP) [83] which is motivated by the EM algorithm to alternatively update the sparsity and support. Another widely used greedy algorithm is Iterative Hard Thresholding (IHT) [78] which implements the gradient descent with a thresholding operation iteratively:

$$\mathbf{s}^{n+1} = \mathcal{T}(\mathbf{s}^n + \mathbf{A}^H(\mathbf{y} - \mathbf{A}\mathbf{s}^n), \varphi) \qquad (2.51)$$

which is designed to solve (2.47). The $\mathcal{T}(\mathbf{a}, b)$ operator is the hard-thresholding operator which sets all the elements in $\mathbf{a}$ below b (in magnitudes) to zeros, φ is the constant for thresholding, and $\mathbf{s}^n$ represents the estimated $\mathbf{s}$ at n-th iteration. Here the thresholding operations are sparsifying the estimated variable $\mathbf{s}$.

Note that if the projection matrix $\mathbf{A}$ in IHT is the SAR forward operator, the estimated $\mathbf{s}^{n+1}$ with iterative gradient descent is the SAR image. Within this context, the thresholding

operation is sparsifying the estimated SAR image. This feature establishes the strong links between optimisation, SAR imaging and compressed sensing which inspires us to investigate the practicality of employing sparsity in SAR/GMTI.

2.3.2 Connections between SAR-based GMTI and CS

With compressed sensing there exists the potential to extract crucial information by exploiting the signal sparsities in a variety of sophisticated sensing modalities. For example, the fact that a chemical mixture only consists of a finite number of components can be exploited in the chemical composition analysis [7]. Both qualitative and quantitative chemical analysis can benefit from these additional sparse regularisations. In a number of Radar applications, the signal of interest is normally sparse in the range direction. Therefore, the reflected signals can be taken as sparse in the range dimension. Obviously the range surveillance radars can benefit from this feature. Furthermore, the sparsities can be applied to the high resolution imaging radars especially the observed region only consists of few main scatterers.

Particularly Synthetic Aperture Radar (SAR) imaging systems are based on the assumption of a static scene and thus moving targets get blurred and dislocated in the image. GMTI (Ground Moving Target Indication) is of great value especially in military environments. Given that there are a limited number of moving targets in the observed scene, this sparsity can be explored to help distinguish the moving targets from stationary clutters. We note that the CS reconstruction models are in optimisation forms and SAR image formation is essentially solving an optimisation problem. If we consider the GMTI problems in the image domain, the target detection can be realised via a sparsity-regularised optimisation model.

In addition, the motion parameters of the moving targets can be estimated by introducing the target sparsities. The blurred and displaced targets can be relocated and refocused with correct motion parameters which correspond to the sparsest configuration. We are therefore motivated to explore SAR/GMTI by designing a single optimisation framework which integrates all the conventional SAR/GMTI processing stages with sparsities. The utilisation of sparsity aims to address the need of modern battlefield intelligence and improve the SAR/GMTI performance. The proposed framework in this thesis consists of data pre-processing, incorporation of DEM, target detection, SAR image formation, target imaging and target state estimation which forms a complete pipeline with sparsity. The sparse representations are thus incorporated in signal processing techniques to model SAR/GMTI problems from a unique perspective. We also review

the state-of-the-art sparsity-driven SAR/GMTI approach in section 2.6.2.

2.4   GMTI Techniques

In SAR/GMTI applications, a number of well-known methods have been established. For example, the moving reflectors can be marked through identifying the target signatures in the exo-clutter regions [84], i.e. the area outside the mainlobe clutter. Therefore, single-channel SAR systems are capable of detecting the moving targets in this class. Some other single channel systems are directly exploiting the target reflectivities, e.g. moving targets can be detected through identifying the significant reflectivities against the water in maritime scenarios [85] [86], while another group of researchers have focused on the exploitation of change detection methods in SAR/GMTI [87] [88].

However, for the moving targets buried in the endo-clutter, clutter suppression approaches are required for discriminating the targets from the background. Typical methods include the widely used multi-channel approaches including Displaced Phase Center Antenna (DPCA), Along Track Interferometry (ATI) and Space-time Adaptive Processing (STAP) [89] [90]. In particular, DPCA suppresses the clutter based on magnitudes of different channels in the image domain, ATI reveals moving targets via the interference phases between different radar channels, and STAP is a computational expensive filtering technique based on adaptive weights. These methods have been proven to give acceptable performance in various of SAR/GMTI scenarios. Recently, a number of developments in SAR/GMTI aimed to extend these techniques to achieve better performance. The latest developments include the extended/generalised DPCA algorithm (EDPCA) to enhance the conventional algorithms [91], the hybrid techniques that use DPCA and ATI [92] [93], and the sparsity based approaches [6] [94].

Furthermore, the GMTI techniques for SAR monitoring applications can be divided with two major classes, i.e. the methods that reveals moving targets in the image domain (SAR-based GMTI) and the approaches that indicates dynamic objects utilising the raw data (raw-data-based GMTI). The DPCA and ATI methods fall into the SAR-based GMTI class, and the STAP algorithm falls into the raw-data-based class. The SAR/GMTI framework developed in this thesis aims to establish an end-to-end framework to detect the moving targets in the SAR images, and it closely relates to the conventional SAR-based DPCA and ATI algorithms.

2.4.1 Space-Time Adaptive Processing

Space-Time Adaptive Processing (STAP) is an adaptive array processing algorithm for target indication. It combines the radar signals from different channels to establish a multidimensional filter, and suppresses the interference (e.g. clutter , jammers) and noises to reveal moving targets. Particularly the STAP theory aims to maximise the Signal-to-Interference and Noise Ratio (SINR) at the processor outputs, and the mechanism of STAP is depicted in Fig. 2.7.

Let N be the number of pulses, I be the number of SAR channels, and K be the number of range bins, the adaptive weights can be estimated for each range gate and the detection processor gives the scalar output:

$$z = \mathbf{w}^H \mathbf{Y}_{in} \tag{2.52}$$

where $\mathbf{Y}_{in}$ represents the NI-by-1 space-time data which is vectorized, and $\mathbf{w}$ is the weight vector.

Note that the weight vectors are estimated based on different target states which essentially establish a filter bank for the target detection. The STAP processor output z can be subsequently fed into the Constant False Alarm Rate (CFAR) [95] detectors to be compared with specific thresholds. This procedure needs to be implemented for each cell of interest which makes the STAP algorithm in general computationally intensive .
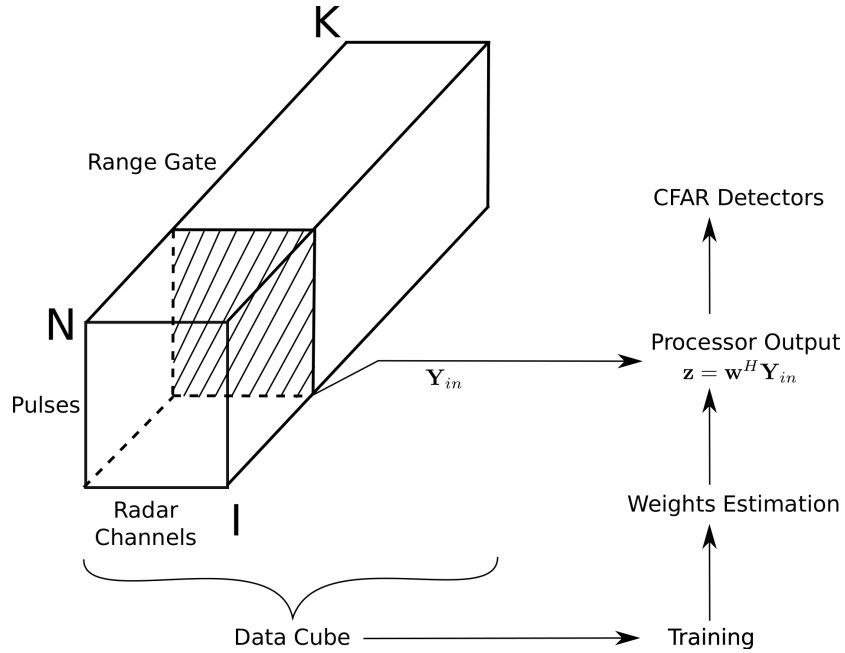
Figure 2.7: The STAP processing pipeline.

Here we consider one simple ideal case with multiple antennas and one pulse as an example

to briefly explain the spatial processing in STAP. We first define $\mathbf{S}_{st}$ as the steering vector to encode the phase differences between different channels and its elements are in the form of $\exp\left(2\pi\langle\frac{\mathbf{v}_p}{v_p}, \frac{\mathbf{r}_i^{(t)}}{r_i^{(t)}}\rangle(i-1)d/\lambda\right)$. With this steering vector, for one interference source, the SAR data $\mathbf{Y}_{in}$ can be expressed with the sum of signal, interference and noise:

$$\mathbf{Y}_{in} = Y_s\mathbf{S}_{st} + Y_{int}\mathbf{S}_{st} + \mathbf{Y}_{no} \tag{2.53}$$

where Y_s is the nominal target signal, $\mathbf{Y}_{no}$ is the noise vector, and the nominal interference signal vector contained in $\mathbf{Y}_{in}$ is $Y_{int}\mathbf{S}_{st}$. The power of noise in $z = \mathbf{w}^H\mathbf{Y}_{in}$ can then be derived as:

$$P_{no} = E\{|\mathbf{w}^H\mathbf{Y}_{no}|^2\} = E\{\mathbf{w}^H\mathbf{Y}_{no}\mathbf{Y}_{no}^H\mathbf{w}\} = \mathbf{w}^H\mathbf{R}_{no}\mathbf{w} \tag{2.54}$$

where $\mathbf{R}_{no} = E\{\mathbf{Y}_{no}\mathbf{Y}_{no}^H\}$ is the noise covariance matrix. Similarly, we can have $\mathbf{R}_{int} = Y_{int}^2 E\{\mathbf{S}_{st}\mathbf{S}_{st}^H\}$ as the interference covariance matrix, and $\mathbf{R} = \mathbf{R}_{no} + \mathbf{R}_{int}$ as the interference-and-noise covariance matrix.

Since $\mathbf{R}$ is positive definite because of the noises in receivers, $\mathbf{R}^{1/2}$ is real [96]. If we define $\mathbf{w}_{aux}$ as $\mathbf{R}^{1/2}\mathbf{w}$, the Signal-to-Interference and Noise Ratio (SINR) can be derived as:

$$\frac{|\mathbf{w}^H Y_s\mathbf{S}_{st}|^2}{\mathbf{w}^H\mathbf{R}\mathbf{w}} = P_s\frac{|\mathbf{w}^H\mathbf{R}^{1/2}\mathbf{R}^{-1/2}\mathbf{S}_{st}|^2}{\mathbf{w}^H\mathbf{R}^{1/2}\mathbf{R}^{1/2}\mathbf{w}} = P_s\frac{|\mathbf{w}_{aux}^H\mathbf{R}^{-1/2}\mathbf{S}_{st}|^2}{\|\mathbf{w}_{aux}\|^2} \tag{2.55}$$

where P_s is the nominal constant for signal power.

Maximising (2.55) leads to

$$\mathbf{w}_{aux} = \rho\mathbf{R}^{-1/2}\mathbf{S}_{st} \tag{2.56}$$

where ρ is a constant, and this result is equivalent to:

$$\mathbf{w} = \rho\mathbf{R}^{-1}\mathbf{S}_{st} \tag{2.57}$$

Therefore, the SINR at processor output z is maximised with this estimated weight vector $\mathbf{w}$. Here the inverse of the interference-and-noise covariance matrix $\mathbf{R}^{-1}$ is essentially performing the clutter suppression, and the steering vector $\mathbf{S}_{st}$ is compensating the channel differences. The target can then be detected after the clutter cancellation. In practice, the interference-and-noise covariance matrix $\mathbf{R}$ can be estimated empirically as shown in [97]. This argument (2.57) is applicable to the cases of multiple pulses and interference sources with adaptive strategies [96]. There exist a variety of extensions and variants for the STAP algorithm [30]. Practically the STAP

algorithm calculates the weights for every element and it is widely known to be hampered by the expensive computational load.

While the DPCA and ATI algorithms are subtractive methods that indicate moving targets through the differences between SAR channels in the image domain, the STAP mechanism is a raw-data-based method as described above. The proposed SAR/GMTI framework follows the route of DPCA and ATI to model the moving targets among SAR images. In this section we do not further more details of STAP.

2.4.2 DPCA and ATI

The widely used DPCA and ATI algorithms (image-based approaches) are typical subtractive GMTI methods which exploit the differences between SAR channels to detect moving targets and suppress the clutter. In particular we will see, DPCA is noise-limited since the noise can corrupt the differential image between different channels and ATI is clutter-limited since the clutter will contaminate the image phases if its energy is comparable to the moving targets. Recently, a hybrid DPCA/ATI algorithm was proposed to benefit from both DPCA and ATI, and it was demonstrated to achieve better GMTI accuracy than DPCA or ATI alone [93].

Let the $\Phi_B^{\mathbf{V}}$ and Φ_B^0 be the inverse operators of $\Phi_F^{\mathbf{V}}$ and Φ_F^0 which project the received signals to reflectivities, and $\widetilde{\mathbf{Y}}_i$ be the pre-processed phase histories of the $i-$th channel (antenna gains have been equalised) where $\widetilde{\mathbf{Y}}_2$ can be taken as the time-shifted version of $\mathbf{Y}_2$, i.e. $\widetilde{\mathbf{Y}}_2(f_k, \tau_n) = \mathbf{Y}_2(f_k, \tau_n + \Delta)$ regardless of the antenna gains. For the i-th channel, the SAR image formation can be realised via $\mathbf{X}_i = \Phi_B^0(\widetilde{\mathbf{Y}}_i)$, where the backward projection operator Φ_B^0 is the Hermitian transpose of Φ_F^0 in the sense of matrices.

As the channel spacing d in the SAR system is along the platform track, the received echo of the aft-antenna (the antenna behind the fore-antenna) can be viewed as the delayed received signal of the fore-antenna, if the observed region does not change over time. We can illustratively assume that $\mathbf{r}_1^{(c)}(\tau_n) = \mathbf{r}_2^{(c)}(\tau_n + \Delta)$ where $\mathbf{r}_i^{(c)}(\tau_n)$ denotes the location of the $i-th$ antenna at time τ_n and $\Delta = d/v_p$ represents the time delay between the neighbouring channels. Here $\tau_n + \Delta$ may not correspond to an exact pulse time. Then the differential range of the second channel at azimuth time $\tau_n + \Delta$ can be written as

$$
\begin{aligned}
u_2(\tau_n + \Delta) &= r_2^{(t)}(\tau_n + \Delta) - r_2^{(o)}(\tau_n + \Delta) \\
&= \|\mathbf{r}_2^{(c)}(\tau_n + \Delta) - \mathbf{r}_t(\tau_n + \Delta)\| - \|\mathbf{r}_2^{(c)}(\tau_n + \Delta)\|
\end{aligned}
$$

$$=\|\mathbf{r}_1^{(c)}(\tau_n) - \mathbf{r}_t(\tau_n + \Delta)\| - \|\mathbf{r}_1^{(c)}(\tau_n)\| \tag{2.58}$$

where $\mathbf{r}_t$ is the instantaneous position vector of the target.

If the targets are isotropic and their reflectivities keep the same over time, the phased histories of the 1st and 2nd channels for the target can be formulated based on (2.31) as:

$$Y_1(f_k, \tau_n) = A_1 \sigma \times$$
$$\exp\left(-\frac{j4\pi f_k(\|\mathbf{r}_1^{(c)}(\tau_n) - \mathbf{r}_t(\tau_n)\| - \|\mathbf{r}_1^{(c)}(\tau_n)\|)}{c} \right) \tag{2.59}$$

$$Y_2(f_k, \tau_n + \Delta) = A_2 \sigma \times$$
$$\exp\left(-\frac{j4\pi f_k(\|\mathbf{r}_1^{(c)}(\tau_n) - \mathbf{r}_t(\tau_n + \Delta)\| - \|\mathbf{r}_1^{(c)}(\tau_n)\|)}{c} \right) \tag{2.60}$$

After the pre-processing stage, the antenna gains A_1 and A_2 are equalised. Thus the DPCA algorithm using only first two channels can reveal the targets via:

$$\mathbf{X}_1(m, l) - \mathbf{X}_2(m, l)$$
$$= \Phi_B^0(\widetilde{\mathbf{Y}}_1) - \Phi_B^0(\widetilde{\mathbf{Y}}_2)$$
$$= \sum_{k=1}^{K}\sum_{n=1}^{N} \widetilde{\mathbf{Y}}_1(f_k, \tau_n) \exp\left(\frac{j4\pi f_k \Delta\mathbf{R}_{mln}}{c}\right)\left(1 - \frac{\widetilde{\mathbf{Y}}_2(f_k, \tau_n)}{\widetilde{\mathbf{Y}}_1(f_k, \tau_n)}\right)$$
$$= \sum_{k=1}^{K}\sum_{n=1}^{N} \widetilde{\mathbf{Y}}_1(f_k, \tau_n) \exp\left(\frac{j4\pi f_k \Delta\mathbf{R}_{mln}}{c}\right)\left(1 - \exp\left(-\frac{j4\pi f_k(\Diamond\mathbf{R}_{mln})}{c}\right)\right) \tag{2.61}$$

where $\Diamond\mathbf{R}_{mln} = \|\mathbf{r}_1^{(c)}(\tau_n) - \mathbf{r}_{ml}(\tau_n + \Delta)\| - \|\mathbf{r}_1^{(c)}(\tau_n) - \mathbf{r}_{ml}(\tau_n)\|$, which is associated with the phase difference between $\widetilde{\mathbf{Y}}_2(f_k, \tau_n)$ and $\widetilde{\mathbf{Y}}_1(f_k, \tau_n)$.

At azimuth time τ_n, the position of the target, which was initially located at (x_m, y_l), is denoted as $\mathbf{r}_{ml}(\tau_n)$. $\Diamond\mathbf{R}_{mln}$ can then be approximated by $v_{ml}^{(r)}\Delta$ where $v_{ml}^{(r)}$ is the radial velocity of this target. Also $\exp(-j4\pi f_k\Diamond\mathbf{R}_{mln}/c)$ can be approximated with a constant if the target remains in the same range resolution cell during the time interval Δ [98]. The equation (2.61) can then be rewritten as:

$$\mathbf{X}_1(m, l) - \mathbf{X}_2(m, l) \approx \mathbf{X}_1(m, l)\left(1 - \exp\left(-\frac{j4\pi f_0(v_{ml}^{(r)}\Delta)}{c}\right)\right) \tag{2.62}$$

where f_0 is denoted as the centre frequency of the transmitted signal chirps.

The DPCA algorithm is calculating (2.62) followed by a thresholding operation. It can be seen from (2.62) that the magnitudes of the DPCA results are controlled by the radial velocities $v_{ml}^{(r)}$. If $v_{ml}^{(r)} = 0$ we have $\mathbf{X}_1(m,l)-\mathbf{X}_2(m,l) \approx 0$. Therefore, the DPCA results can indicate the moving targets based on their radial velocities. Note that the DPCA expressions have ambiguities on the results for the velocities due to the periodic complex exponential. For example, different $v_{ml}^{(r)}$ can result in the same $\exp(-\dfrac{j4\pi f_0(v_{ml}^{(r)}\Delta)}{c})$. The different radial velocities which lead to the same results in (2.62) are termed as the blind velocities in the DPCA algorithm.

Similarly the ATI algorithm is marking moving targets through the phases of different channels. The phase terms are well known to encode the target radial velocities which can be thresholded to reveal the moving targets. The ATI algorithm can be formulated as:

$$\mathbf{X}_1(m,l) \times \mathbf{X}_2^*(m,l) \approx |\mathbf{X}_1(m,l)|^2 \exp\left(\frac{j4\pi f_0 \Diamond \mathbf{R}_{mln}}{c}\right)$$

$$\approx |\mathbf{X}_1(m,l)|^2 \exp\left(\frac{j4\pi f_0(v_{ml}^{(r)}\Delta)}{c}\right) \tag{2.63}$$

It can be seen that the phase of (2.63) is a function of the radial velocity $v_{ml}^{(r)}$ which is zero for stationary targets ($v_{ml}^{(r)} = 0$). Based on the phases in (2.63), the radial velocity map of the scene $\mathbf{V}^{(r)}$ can be estimated.

Overall, the DPCA results are approximately the velocity-scaled reflectivities of the moving targets. DPCA and ATI are utilising different information to realise SAR/GMTI but they do share the similarities. The clutter suppression techniques such as DPCA and ATI enable us to filter out stationary targets. They are followed by detectors such as CFAR detectors [95] to shreshold the outputs. These threshold operations are similar to the operations in CS reconstruction methods which inspires the sparsity-driven SAR/GMTI. Furthermore, it is shown in (2.63) that the target radial velocities $\{v_{ml}^{(r)}|m = 1, 2, ..., M; l = 1, 2, ..., L\}$ can be directly estimated based on the phases of ATI results.

2.4.3 Hybrid DPCA/ATI

The hybrid DPCA/ATI algorithm is designed to integrate the DPCA and ATI algorithms for the multi-channel SAR/GMTI tasks, and its effectiveness against conventional DPCA and ATI has been demonstrated in [93]. In particular, for a three-channel SAR system, the hybrid DPCA/ATI

algorithm first implements the DPCA algorithm pair-wise for the 1st/2nd channel and 2nd/3rd channel respectively, and retrieves two DPCA results. A subsequent stage which applies the ATI algorithm to the two DPCA results is then employed, and the phase of the ATI result is thresholded to reveal moving targets. The hybrid DPCA/ATI algorithm is supposed to benefit from both DPCA and ATI algorithms and enhance the overall SAR/GMTI performance.

The mathematical model of the hybrid DPCA/ATI algorithm for three channels can be formulated as:

$$(\mathbf{X}_1(m,l) - \mathbf{X}_2(m,l)) \times (\mathbf{X}_2(m,l) - \mathbf{X}_3(m,l))^*$$

$$\approx |\mathbf{X}_1(m,l) \left(1 - \exp\left(-\frac{j4\pi f_0(v_{ml}^{(r)}\Delta)}{c}\right)\right)|^2 \exp\left(\frac{j4\pi f_0(v_{ml}^{(r)}\Delta)}{c}\right) \qquad (2.64)$$

It can be seen that the phase of (2.64) is a periodic function of the target radial velocity $v_{ml}^{(r)}$. Similar to ATI, the radial velocities $\{v_{ml}^{(r)} | m = 1, 2, ..., M; l = 1, 2, ..., L\}$ can be estimated based on the phases of (2.64) whithin a periodic interval to avoid the blind velocities, and the radial velocity map for the whole scene can be approximated. The hybrid DPCA/ATI can incorporate the advantages of both DPCA and ATI, and thus significantly improve the clutter suppression performance. As long as the channel balancing in the pre-processing is good enough and the signal is not governed by the noise, this hybrid method is capable of detecting the moving targets and estimating their radial velocities. It has been proved that this method can achieve better GMTI performance than DPCA and ATI in multiple scenarios [92]).

2.5 Channel Balancing for Multi-channel SAR

It can be seen from section 2.4 that a pre-processing stage is required for subtractive SAR/GMTI algorithms to retrieve the same responses for the static reflectors between different SAR channels. In particular, as discussed in section 2.4.2, the pre-processed phase histories $\widetilde{\mathbf{Y}}_i$ for the i-th channel can be approximated with a small azimuth time shift and a scaling constant on the amplitudes. Therefore, the time shift corresponds to a linear phase shift via Fourier transforms. The existing linear fitting algorithms [99] [100] are approximating a linear phase term to compensate the channel imbalances. The two-dimensioinal balancing algorithm [101] is capable of estimating more complicated calibration terms with iterations.

In this section, we review a recent channel balancing algorithm [102] which equalises

the channel imbalances in the image domain. For simplicity, we denote $\mathbf{X}_i^{raw}$ as phase histories for the i-th channel without channel balancing and consider two SAR channels. Therefore, $X_i^{raw}(m, l)$ stands for the reflectivity of the pixel (m, l). We denote $\mathbf{H}^{raw}$ as the calibration matrix in the image domain so that the calibrated 2-nd channel reflectivity of (m, l) is $X_2^{cal}(m, l) = X_2^{raw}(m, l)H^{raw}(m, l)$. It is obvious that $\mathbf{X}_1^{raw} = \mathbf{X}_2^{cal}$ if $H^{raw}(m, l) = X_1^{raw}(m, l)/X_2^{raw}(m, l)$, and all the differences between the two channels are eliminated. To only cancel the differences for the background, we can assume that the background reflectivity of a pixel can be approximated with the average value within a window centered on the pixel.

Let $2N^{win} + 1$ be the window size, $w(m, l)$ be the weight of (m, l) within the window, and $\angle$ be the operator to extract the phases. The calibration can be realised via:

$$|H^{raw}(m, l)| =$$

$$\frac{1}{(N^{all} - N^{zero})} \sum_{k_1=-N^{win}}^{N^{win}} \sum_{k_2=-N^{win}}^{N^{win}} w(k_1, k_2) |\frac{X_1^{raw}(m + k_1, l + k_2)}{X_2^{raw}(m + k_1, l + k_2)}| \quad (2.65)$$

$$\angle H^{raw}(m, l) =$$

$$\angle\left(\frac{1}{(N^{all} - N^{zero})} \sum_{k_1=-N^{win}}^{N^{win}} \sum_{k_1=-N^{win}}^{N^{win}} w(k_1, k_2) \exp(j\angle(\frac{X_1^{raw}(m + k_1, l + k_2)}{X_2^{raw}(m + k_1, l + k_2)}))\right) \quad (2.66)$$

where $|H^{raw}(m, l)|$ and $\angle H^{raw}(m, l)$ are the amplitudes and phases of $H^{raw}(m, l)$ respectively, $N^{all} = (2N^{win} + 1)^2$ is the number of pixels in the window, N^{zero} is the number of zeroes in the window.

Note that the moving target may be significant in the central pixel (m, l). A practical window function is to set the weight coefficients around pixel (m, l) to zeroes. The performance of this image-based channel balancing method significantly depends on the design of the window function and the signatures of moving targets. In Chapter 3, we will present the detailed channel calibration used in this thesis.

2.6 Target State Estimation Algorithms

It is widely known that the moving targets will be displaced and blurred in the formed SAR images [103] [94] [84]. In many scenarios we want to go beyond the simple ground moving target

indication and estimate the target states. There have been a number of investigations on the effects of moving objects [104] [103] and algorithms for motion parameter estimation [104] [91] [18]. For example, [104] analyses how the target shape varies with motion parameters and how different motion types perform in the SAR images. In [105] the constant movement, acceleration, vibration and rotation of moving targets are studied. Recalling that GMTI algorithms can be divided into two classes, i.e. the SAR-based methods and raw-data-based methods. Some conventional GMTI algorithms such as DPCA and ATI are SAR-based methods to indicate moving targets in the image domain and they are not capable of estimating the full moving target states. The EDPCA [91] and ISTAP [18] algorithms are two state-of-the-art GMTI approaches which are capable of cancelling the clutter, and they share the same idea to approximate the motion parameters by maximising the target SNR. Some recent developments in SAR/GMTI involve the exploitation of sparsity. In [94], the sparse reconstruction is applied to the SAR image pixel-wise for the estimation of radial velocities. Particularly, the sparsities are encoded in the veclocities by assuming that each pixel is associated with no more than two radial velocities. In [106], the moving target imaging is compensated by the phase errors, while the sparsities are reflected in the reflectivities and phase errors.

2.6.1 Effects of Moving Targets in SAR

Target Displacement

The moving targets will be defocused and displaced mainly along the azimuth direction in the SAR images. Based on the geometry of the multi-channel SAR system, we first present the displacement effects of moving targets along with a target relocation mechanism in this section.

For a stationary target, its Doppler frequency shift depends on the relative velocity between the target and the platform:

$$f_d = 2v_p \langle \frac{\mathbf{v}_p}{v_p}, \frac{\mathbf{r}_1^{(t)}}{r_1^{(t)}} \rangle / \lambda_0 \qquad (2.67)$$

where v_p is the platform velocity, $\mathbf{v}_p$ denotes the platform velocity, $\mathbf{r}_1^{(t)}$ stands for the vector from the 1st channel to target, and λ_0 represents the central wavelength of the transmitted signal. Let α be the angle between the platform velocity and the vector to the reflector, we have

$\cos(\alpha) = \langle \dfrac{\mathbf{v}_p}{v_p}, \dfrac{\mathbf{r}_1^{(t)}}{r_1^{(t)}} \rangle$. Therefore, the azimuth position of the reflector can be estimated via:

$$\alpha = \arccos\left(\lambda_0 f_d / (2v_p)\right) \qquad (2.68)$$

Similar to (2.67), a moving target with radial velocity $v^{(r)}$ will induce the change in Doppler frequency δf_d:

$$\delta f_d = 2v^{(r)}/\lambda_0 \qquad (2.69)$$

Differentiating (2.67) gives the change in azimuth position:

$$\delta\alpha = -\frac{\lambda_0 \delta f_d}{2v_p \sin(\alpha)} \qquad (2.70)$$

which stands for the azimuth displacement of the target in the SAR image. By considering (2.69) we have that:

$$\delta\alpha = -\frac{v^{(r)}}{v_p \sin(\alpha)} \qquad (2.71)$$

Therefore, (2.71) quantifies the azimuth displacement of a moving target in the SAR image which is depicted in Fig. 2.8. Given v_p, α and the radial velocity $v^{(r)}$, the moving target can be relocated to the correct position in the SAR image by simply shifting the entire target pattern with $-\delta\alpha$. This gives a brief insight into how the target radial velocity impacts the azimuth displacement in the SAR image, and the moving target location can thus be corrected with this model.

Target Blurring

We have analysed how the azimuth position of the moving target changes with the target radial velocity $v^{(r)}$. In this section, we give an insight into the blurring effect of a moving target in the SAR image.

As the phase of the received signal depends on the round-trip distance of the transmitted signal:

$$\begin{aligned} \Theta(t) &= \frac{2\pi}{\lambda_0} 2r_1^{(t)} \\ &= \frac{4\pi}{\lambda_0} r_1^{(t)} \end{aligned} \qquad (2.72)$$
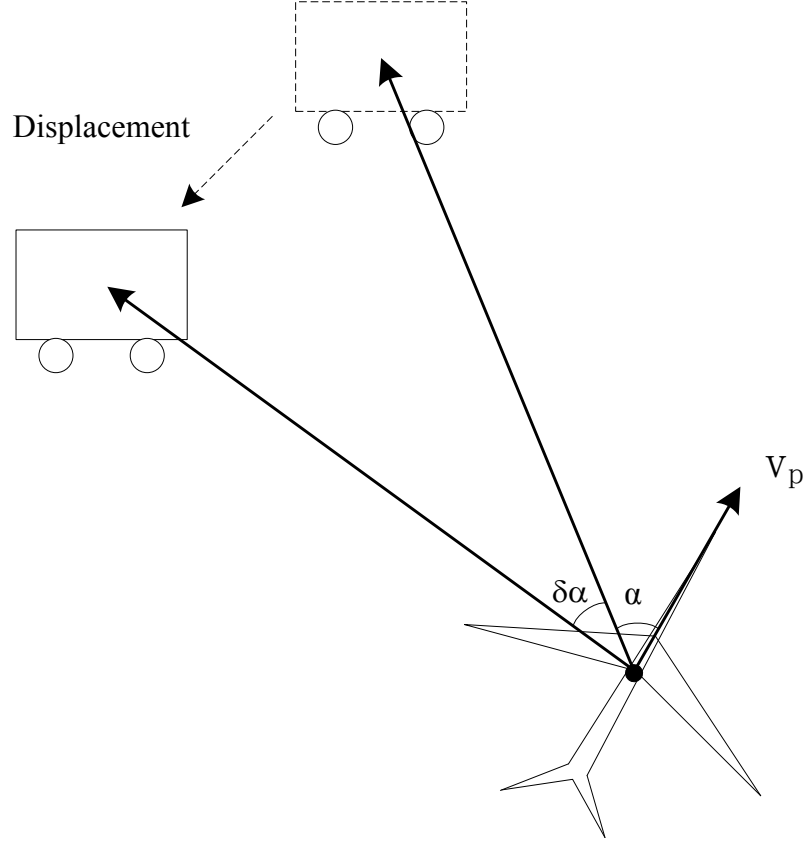
Figure 2.8: The azimuth displacement of a moving target in SAR.

where $2\pi/\lambda_0$ is the wavenumber, and $r_1^{(t)}$ denotes the distance between the target and 1st channel.

Similar to the definition of $v^{(r)}$, we denote $a^{(r)}$ as the acceleration rate of the moving target in radial direction. By employing the Taylor expansion, we can approximate $r_1^{(t)}$ with:

$$r_1^{(t)} \approx r_1^{(0)} + v^{(r)}t + \frac{1}{2}a^{(r)}t^2 \tag{2.73}$$

Therefore, besides the doppler frequency shift introduced by the platform, the doppler frequency shift component introduced by the moving target can be formulated as:

$$\delta f_d = \frac{1}{2\pi}\frac{d\Theta(t)}{dt} \approx 2(v^{(r)} + a^{(r)}t)/\lambda_0 \tag{2.74}$$

By comparing (2.74) to (2.69), (2.74) has an additional term $2a^{(r)}t/\lambda_0$ in the Doppler frequency change δf_d that varies with the time t. Note that the azimuth displacement of the target is proportional to the change in δf_d based on (2.70). Therefore, the varying δf_d leads to the varying azimuth position of the target. The synthetic aperture time t interacts with $a^{(r)}$ to control the change in δf_d which induces the blurring along the azimuth direction. The blurring of

a moving target in the SAR image can then be quantified with $a^{(r)}$. The Doppler frequency shift stretches by:

$$\delta f_d' = \frac{2a^{(r)}}{\lambda_0}T \tag{2.75}$$

where T is the time interval of the synthetic aperture.

Considering (2.70), we have that the azimuth angle α stretches by:

$$\delta\alpha' = \frac{a^{(r)}T}{v_p \sin(\alpha)} \tag{2.76}$$

where $\delta\alpha'$ accounts for the azimuth blurring length of the moving target.

It is shown in (2.76) that the length of blurring is proportional to $a^{(r)}$. It is also discussed in [103] that the blurring will increase with the smaller SAR azimuth resolution and high observation squinted angles.

2.6.2 SAR-based GMTI with Sparsity

While there have been a number of investigations about the sparsity in SAR [94] [107], this field is still in its infancy to be explored. Particularly, [107] is a novel method that searches for the sparsest solution in the target location-velocity space for a single-channel SAR system, and its searching space is limited on a rough grid considering the RIP condition of sparse reconstructions. In this subsection, we review the state-of-the-art investigation on using the compressed sensing algorithms to detect moving targets and estimate the radial velocities via multi-channel SAR systems [108] [109] [110]. This novel method is essentially utilising the sparsity in target radial velocities pixel-wise. To be specific, it is well known that the SAR images of one moving target will have a phase difference $(4\pi/c)f_0 v^{(r)}(d/v_p)$ between two neighbouring channels, in which f_0 denotes the central frequency of the transmitted signal, v_p is the platform velocity, $v^{(r)}$ is the radial velocity of the target, d denotes the spatial distance between the antennas. Therefore, an explicit model can be established to describe the differences of SAR images between different Radar channels with the $v^{(r)}$ and d.

If we assume that there are N_v radial velocity components for the individual SAR pixel, for the radar channel which has the distance d_c from the platform center, the individual SAR pixel

$\mathbf{X}_{d_c}(m, l)$ at (m, l) with this channel can be expressed as the sum of the N_v components:

$$\mathbf{X}_{d_c}(m, l) = \sum_{n_v=1}^{N_v} \mathbf{A}(n_v, m, l) \exp\left(-j\frac{4\pi}{c}f_0 v_{n_v}^{(r)}\frac{d_c}{v_p}\right) \tag{2.77}$$

where $\mathbf{X}_{d_c}(m, l)$ is the (m, l) pixel of the formed SAR image for this channel based on pre-processed data, $v_{n_v}^{(r)}$ is the n_v-th radial velocity component of the pixel (m, l), and $\mathbf{A}(n_v, m, l)$ represents the corresponding amplitude of the n_v-th radial velocity component with respect to the (m, l) pixel.

Note that most SAR pixels are associated with no more than two radial velocity components, i.e. static objects (0 m/s) and a moving target. Therefore, the sparsity in the model (2.77) is reflected in the number of velocity components of individual SAR pixels. By further considering the multi-channel SAR system, (2.77) can be reformulated into the generic form for the i-th channel:

$$\mathbf{X}_i(m, l) = \sum_{n_v=1}^{N_v} \mathbf{A}(n_v, m, l) \exp\left(-j\frac{4\pi}{c}f_0 v_{n_v}^{(r)}\frac{(i-1)d}{v_p}\right) \tag{2.78}$$

in which we assume that the SAR antennas are evenly spaced with the distance d.

Based on (2.78), if we focus on the (m, l) pixel and concatenate the samples from all I channels $\mathbf{X}_{vec}(m, l) = [\mathbf{X}_1(m, l), \mathbf{X}_2(m, l), ..., \mathbf{X}_I(m, l)]^T \in \mathbb{C}^{I \times 1}$, $\mathbf{X}_{vec}(m, l)$ can be modelled with matrices as:

$$\mathbf{X}_{vec}(m, l) = \Theta \mathbf{A}_{vec} \tag{2.79}$$

in which the (i, n_v)-th entry of $\Theta \in \mathbb{C}^{I \times N_v}$ is $\exp(-j\frac{4\pi}{c}f_0 v_{n_v}^{(r)}\frac{(i-1)d}{v_p})$, and $\mathbf{A}_{vec} = [\mathbf{A}(n_v, m, l), \mathbf{A}(n_v, m, l), ..., \mathbf{A}(n_v, m, l)]^T \in \mathbb{C}^{N_v \times 1}$ represents the amplitudes of the radial velocity components at (m, l) which is a sparse vector.

The equation (2.79) stands for a typical sparse approximation model which can be solved via a variety of sparse reconstruction algorithms, and the sparse vector $\mathbf{A}_{vec}$ can be reconstructed. By identifying the non-zero entries of $\mathbf{A}_{vec}$, the moving targets at (m, l) can be detected and the corresponding radial velocities can be selected. We resolve (2.79) repetitively for each SAR pixel to indicate the moving targets for the whole scene, and the corresponding map of radial velocities can be produced. This process is visualised in Fig. 2.9.

This algorithm essentially establishes a sparse reconstruction model to produce a map of target radial velocities. From this perspective, it is similar to the ATI algorithm. This method does not estimate full target states, and the defocusing and relocation of the moving targets are not
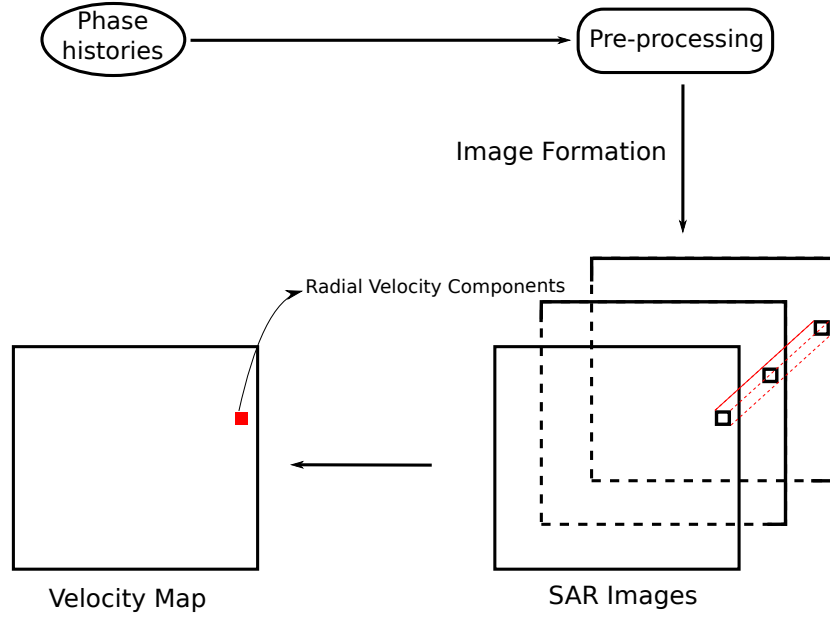
Figure 2.9: The flowchart of the described algorithm in this subsection to estimate the radial velocity map with sparsities.

investigated.

2.6.3 Extended DPCA

The Extended DPCA (EDPCA) [91] is a state-of-the-art GMTI algorithm which is capable of estimating the full target state. The algorithm is motivated to generalise the DPCA algorithm with two channels to multiple channels. The described process in [91] shares significant similarities with the STAP algorithm in range-Doppler domain [97]. In this subsection we briefly explain the core idea of this method. Further details are not included.

The core idea of this algorithm is to utilise all the information from different channels and realise the SAR compression with different ϑ_t (ϑ_t is the motion parameters of a moving target). Note that the responses from static objects are eliminated before the moving target detection. As presented in Chapter 2, the clutter suppression can be realised with the inverse of the clutter-plus-noise covariance matrix. The target state ϑ_t can thus be estimated by maximising the target responses. It is shown in [91] that the generalised likelihood ratio tests (GLRT) on SAR images focused with ϑ_t corresponds to the EDPCA criterion which is defined as:

$$\delta_{EDPCA}(r, T, \vartheta_t) = \frac{|\mathbf{P}_{vec}^H(\vartheta_t)\mathbf{R}^{-1}(\vartheta_t)\mathbf{Z}_{vec}(r, T, \vartheta_t)|^2}{\mathbf{P}_{vec}^H(\vartheta_t)\mathbf{R}^{-1}(\vartheta_t)\mathbf{P}_{vec}(\vartheta_t)} \tag{2.80}$$

In particular, the data are compressed with ϑ_t, and any SAR algorithms can be used. The SAR compressed signal vector $\mathbf{Z}_{vec}(r, T, \vartheta_t)$ in the image domain is associated with the (r, T) pixel, where r denotes the range and T is the slow-time variable. The clutter-plus-noise covariance matrix $\mathbf{R}(\vartheta_t)$ can be estimated from the raw data [97] [91], and the clutter is eliminated with its inverse $\mathbf{R}^{-1}(\vartheta_t)$. Then different SAR channel are coherently added with the steering vector $\mathbf{P}_{vec}^H(\vartheta_t)$. The steering vector compensates the phase difference between different SAR channels. By adopting the definitions in this thesis, we will show in Chapter 4 that $\mathbf{P}_{vec}(\vartheta_t)$ can be approximated by vectorizing the proposed phase correction matrix $\mathbf{P}$, and its entries are the well known ATI phases. The denominator in (2.80) is employed for the normalisation of the $\delta_{EDPCA}(r, T, \vartheta_t)$. With the compensation between different channels and clutter cancellation, it can be seen that maximising (2.80) is essentially maximising the target responses. Finally the EDPCA criterion $\delta_{EDPCA}(r, T, \vartheta_t)$ is compared with a constant using the CFAR detector for each cell (r, T) and target state ϑ_t. The ISTAP method shares the same idea to maximise the GLRT with the clutter cancellation in the Doppler domain [18].

2.7   AFRL GOTCHA GMTI Challenge Dataset

In this section we introduce the AFRL GOTCHA GMTI challenge dataset [4] in details. The effectiveness of the proposed sparsity driven SAR/GMTI framework in the thesis is demonstrated through this dataset. This dataset contains a collection of Matlab files which corresponds to two observation passes with HH polarization three-channel airborne spotlight SAR. The two passes operates above the same urban region for 71 seconds each. While the mission pass is designed with a controlled moving vehicle (GPS device mounted), the reference pass is implemented without this vehicle. Therefore, this dataset raises the SAR/GMTI challenge to detect and track this moving target within the 71 seconds monitoring scenario, and form high resolution SAR images. In this thesis, we focus on the mission pass as a typical multi-channel SAR-based GMTI task, and the performance of the proposed SAR/GMTI framework can be demonstrated through the the target ground truth (based on the GPS) and other SAR/GMTI algorithms.

In general, the dataset contains three types of files, i.e. the raw data files, the SAR auxiliary files and the target auxiliary files. The raw data files are the received phase histories of the SAR channels, the SAR auxiliary files correspond to the SAR system specifications, and the target auxiliary files represent the retrieved information from the portable GPS device. The key system parameters are listed in Table 2.1.

The received phase histories are range gated to mitigate the pressure on saving such a large dataset. The original 5400 range bins are thus trimmed into 384 available range bins which are centred around the target. The offsets of the range bins are provided in the dataset [4]. The 5400-by-154180 phase histories can thus be established by filling the unavailable entries with zeroes, and the formed images are in "slices" with the sub-apertures.

Table 2.1: The system parameters in the AFRL GOTCHA GMTI challenge dataset.

platform start point (m)	(6675.4, 2938.8, 7259.4)
platform end point (m)	(5716.6, -4435.1, 7240.6)
first pulse number	907249
last pulse number	1061428
number of pulses	154180
platform time-of-day	63590-63661
observation duration (s)	71
channel number	3
PRF (Hz)	2171.6
central frequency (Hz)	9.6G
bandwidth (Hz)	640M
phase history size	(5400, 154180)
range gating	384
moving target GPS start point (m)	(7.08, -154.9, 7.8)
moving target GPS end point (m)	(-363.7, 201.5, -10.2)
moving target GPS time-of-day	63575-63676
moving target GPS time offset	-0.9

The airborne SAR system is in the spotlight mode and three channels are mounted on the platform. The system operates in X-band and the signal model can follow the stop-and-go assumption. The controlled vehicle carries a portable GPS device. It first waits for the signal light at a cross, and then accelerates through a downhill road. It finally starts to slow down and turns right at the end of the road. As can be seen from the moving target GPS start and end point in Table 2.1, the monitored scene is associated with non-negligible elevation variations. The GPS configuration follows the right-handed Cartesian coordinate which provides the target velocity magnitude and velocity direction in x-y plane.

The raw data comes from an X-band SAR system with three channels and a number of moving vehicles in a non-homogeneous urban environment. The ground truth data of one vehicle is provided. Its path is along a mountainous road which has significant elevation variations. In

particular, the transmitted chirp is centred at 9.6 GHz, the phase history is collected over a 71 second interval, and the PRF f_{PRF} is 2.1716 kHz. The original data was range-gated from 5400 range samples to 384 bins to decrease the required storage. In [4] the detailed information of the range gating is presented. To preprocess the data, we implement the inverse operation of the the range gating and replace the unknown range gates with zeroes. The phase history after this process is denoted as $\mathbf{Y}_i \in \mathbb{C}^{5400 \times 200}$ for the $i-$th channel. We then apply the channel balancing technique pair-wise as analysed in Chapter 3 and denote the calibrated phase histories as $\widetilde{\mathbf{Y}}_i$.

Unfortunately the AFRL data set does not have all the information we require. Firstly, we do not have any available DEM information. To tackle this issue, we retrieve the coarse DEM data from the United States Geological Survey (USGS) seamless data set [111] (roughly 30 meters resolution). We interpolate the retrieved map on the imaging x-y grid to get the estimated elevations. The method to estimate the calibrated elevation map can be found in section 3.4.1 which is also published in [5]. We apply the DEM to all SAR processing in the experiments.

Secondly, the antenna spacings between channels are unknown in the original data set. Here we estimate the spacings from the raw data. Consider the discrete signals with normalised frequencies, we will introduce the detailed approach to estimate the distance between two channels in section 3.3.2. The three antennas are equally spaced by $d = 0.238m$.

Thirdly, the given ground truth information for the moving vehicle only covers its velocities in the x and y directions. Especially with this data set the monitored region has a non-flat terrain which results in nontrivial velocity components in the z direction. We calibrate the target velocities with a novel method which is presented with details in section 4.4.2.

Furthermore, it can be seen from Table 2.1 that the moving target GPS provides a longer time duration than the platform observation duration. Practically the platform time and moving target GPS time need to be aligned in the SAR/GMTI tasks. The details of the alignment between the target time and platform time are explained in section 5.4.2.

2.8 Conclusion

In this Chapter we have reviewed the mathematical models of SAR systems. Particularly we have analysed the resolution of Radar systems and presented how the SAR systems help improve the resolution. The improved imaging resolution plays a vital role in GMTI applications as targets cannot be well distinguished under low resolution conditions. Furthermore, we introduce the SAR

signal models in details including the pulse compression, dechirping and the approximation of RVP. We then give a brief introduction to the state-of-art GMTI algorithms used in the practical applications. We discuss about the different classes of SAR/GMTI techniques and further analyse their motivations. As the framework proposed in this thesis follows the route of the well known DPCA and ATI, and it aims to leverage the sparsity to establish an optimisation model, we aim to construct an end-to-end framework for SAR-based GMTI in this thesis. The basics of the emerging compressed sensing field are also discussed in this chapter. Specifically we present the origination of CS and its limitations. The key CS properties and the widely used sparse approximation methods are also introduced in this chapter. Finally we link the CS theory to the SAR/GMTI applications and explain in detail about our motivation along with the huge potential of sparsity in SAR-based GMTI processing.

<div align="right">

3

</div>

SAR Pre-processing and DEM-aided SAR

3.1 Introduction

Indicating moving targets among varied scenarios for battlefield reconnaissance is of particular interest to surveillance applications. Note that our focus for SAR/GMTI in this work is on the exploitation of sparsity in SAR-based GMTI applications, and we are motivated by the subtractive algorithms DPCA and ATI. Therefore, for these methods, an important challenge is to understand the differences between SAR channels.

Another challenge arises in the SAR/GMTI processing to mitigate the inaccuracies caused by elevations in the observed area. The effectiveness of conventional approaches has been proven for homogeneous environments (such as vegetated areas). However, the non-homogeneous terrains, such as mountains with large elevation variations and urban areas with significant buildings, are hampering the SAR/GMTI frameworks from many facets: SAR image formation, moving target imaging and state estimation [112]. The injection of the DEM information in SAR/GMTI can help calibrate the SAR images for the monitored region, form the SAR image of moving targets and estimate the target states. Within this work the elevation data is integrated into the proposed SAR/GMTI processing framework.

In this chapter, we present two crucial components in our proposed SAR/GMTI framework, i.e. the pre-processing of phase histories and the exploitation of DEM. We first introduce the general model of multi-channel SAR signals and discuss about the channel balancing methods used for the pre-processing. The calibrations on the phase histories aim to retrieve identical responses from static reflectors for different channels which are crucial in subtractive GMTI methods. Based on the channel balancing approach, The analysis on SAR channel spacing is also included. Secondly, the utilisation of DEM in SAR applications is investigated. The DEM information is integrated into the SAR forward/backward operators which can then be used for the GMTI algorithms. Finally we demonstrate the channel balancing effects in SAR/GMTI tasks

<div align="center">

48

</div>

through the AFRL GOTCHA GMTI challenge data. The exploitation of elevation in SAR/GMTI is also presented via this real dataset.

3.2 Signal Modelling for Multi-channel SAR

Based on the SAR/GMTI geometry as depicted in Chapter 2, we consider a standard multi-channel SAR system in the spotlight mode with a number of moving targets in the observed scene. A terrain map is associated with the monitored region. The phase centres of antennas are equally spaced with a distance d along the flight path of the platform. Let the azimuth time (slow time) of the transmitted pulses be τ_n where $n = \{1, 2, ..., N\}$ is the pulse number; $\mathbf{r}_t(\tau_n)$ be the instantaneous spatial position of one target at τ_n; $r_i^{(t)}(\tau_n)$ and $r_i^{(o)}(\tau_n)$ denote the distance from the target to the $i-$th antenna and the distance from the scene origin to the corresponding antenna position respectively. Within a short sub-aperture, we can assume that the platform velocity is a constant v_p.

The signal model (2.32) can be extended by considering the antenna gain g_i for the i-th SAR channel. If we assume the reflectivity of the target at $\mathbf{r}_t(\tau_n)$ is a constant σ, the discrete received phase histories from the $i-$th channel after the dechirping process (the scene origin is calibrated to have zero phase) and discretization can be formulated as a $K \times N$ complex matrix:

$$\mathbf{Y}_i(f_k, \tau_n) = g_i \sigma \exp\left(-\frac{j4\pi f_k u_i(\tau_n)}{c}\right) \tag{3.1}$$

where $\{f_k | k = 1, 2, ..., K\}$ denotes the range frequencies, c is the speed of light, and $u_i(\tau_n)$ represents the differential range $r_i^{(t)}(\tau_n) - r_i^{(o)}(\tau_n)$.

Given that $\mathbf{X} \in \mathbb{C}^{M \times L}$ is the collection of the nominal reflectivities from all targets (both static and moving) in the scene with antenna gains, similar to (2.32), the received phase history can be assembled by accumulating the reflected signals from all reflectors:

$$\mathbf{Y}_i(f_k, \tau_n) = \sum_{m=1}^{M} \sum_{l=1}^{L} \mathbf{X}(m, l) \exp\left(-\frac{j4\pi f_k u_{mli}(\tau_n)}{c}\right) \tag{3.2}$$

Here $u_{mli}(\tau_n) = r_i^{(m,l)}(\tau_n) - r_i^{(o)}(\tau_n)$ represents the differential range with respect to the reflector at (m, l), in which $r_i^{(m,l)}(\tau_n)$ denotes the distance between the cell (m, l) and platform. The equivalent matrix-vector form of the signal model (3.2) is $\mathbf{Y}_i = \Phi_F(\mathbf{X})$. Note that the $\mathbf{X}$ is

associated with the antenna gains g_i, and these gains need to be equalised via channel balancing techniques to reconstruct the reflectivities and form SAR images. The details of channel balancing can be found in the next section.

Within this signal model, $r_i^{(t)}(\tau_n)$ is the term to indicate how the distance from the antenna to the target varies with time, and it depends on three components, i.e. the platform velocity $\mathbf{v}_p$, the target velocity $\mathbf{v}_t$ and the channel positions.

Let

$$
\begin{aligned}
r_i^{(t_1)}(\tau_n) &= -\langle \mathbf{v}_p, \frac{\mathbf{r}_i^{(t)}}{r_i^{(t)}} \rangle \tau_n \\
r_i^{(t_2)}(\tau_n) &= \langle \mathbf{v}_t, \frac{\mathbf{r}_i^{(t)}}{r_i^{(t)}} \rangle \tau_n \\
r_i^{(t_3)}(\tau_n) &= \langle \frac{\mathbf{v}_p}{v_p}, \frac{\mathbf{r}_i^{(t)}}{r_i^{(t)}} \rangle (i-1)d
\end{aligned}
\tag{3.3}
$$

where the $r_i^{(t_1)}(\tau_n)$, $r_i^{(t_2)}(\tau_n)$ and $r_i^{(t_3)}(\tau_n)$ account for the variations on $r_i^{(t)}(\tau_n)$ induced by the platform velocity, target velocity and channel number respectively.

For a short sub-aperture, the varying range between the target and platform $r_i^{(t)}(\tau_n)$ can be approximated in the form:

$$
r_i^{(t)}(\tau_n) \approx r_1^{(t)}(0) + r_1^{(t_1)}(\tau_n) + r_1^{(t_2)}(\tau_n) + r_i^{(t_3)}(\tau_n)
\tag{3.4}
$$

where the constant $r_1^{(t)}(0)$ corresponds to the distance from the first channel at the initial position of the sub-aperture to the target. Similarly we can decompose the $r_i^{(o)}(\tau_n)$ into three components with an additional constant, and thus implement an expansion on (3.1) given that $u_i(\tau_n) = r_i^{(t)}(\tau_n) - r_i^{(o)}(\tau_n)$. It can be seen from (3.3) and (3.4) that $r_i^{(t_3)}(\tau_n)$ is the dominating channel number related term to be calibrated. These formulations offer us further insight into how different radar channels and the target-platform relative movement function in the signal model, and can be exploited to pre-process SAR data.

3.3   Channel Balancing

3.3.1   Channel Imbalance Calibration

In this section we discuss the pre-processing of the received phase histories based on the aforementioned multi-channel SAR scenario. The task is to implement a channel calibration to acquire the same responses for static reflectors among different channels. An adaptive 2-D channel balancing technique was introduced to tackle this problem in [113]. We adapt this method to mitigate the channel imbalance in the SAR-based GMTI tasks.

Consider the phase terms in (3.1), (3.3) and (3.4), the relative movement between the platform and target will introduce a channel related calibration term to the Doppler transformed signal:

$$
\begin{aligned}
\exp\left(-j\frac{4\pi}{\lambda}\langle\frac{\mathbf{v}_p}{v_p},\frac{\mathbf{r}_i^{(t)}}{r_i^{(t)}}\rangle(i-1)d\right) &= \exp\left(-j2\pi\frac{2v_p}{\lambda}\langle\frac{\mathbf{v}_p}{v_p},\frac{\mathbf{r}_i^{(t)}}{r_i^{(t)}}\rangle\frac{(i-1)d}{v_p}\right) \\
&= \exp\left(-j\omega\frac{(i-1)d}{v_p}\right)
\end{aligned}
\tag{3.5}
$$

where λ is the corresponding wavelength and $\omega = 4\pi\frac{v_p}{\lambda}\langle\frac{\mathbf{v}_p}{v_p},\frac{\mathbf{r}_i^{(t)}}{r_i^{(t)}}\rangle$ is the widely known angular Doppler frequency.

In this section, we adopt the simplified model in Doppler domain (Doppler transformed signal along the azimuth time direction) as reported in [113] to briefly explain the differences between channels. If we put aside the moving targets, we have two channel related facets which influence the Doppler frequency domain signal, i.e. the antenna characteristics g_i and the channel spacing d. The signals in the Doppler domain of the first two channels can be approximated with the equations:

$$
\begin{aligned}
\hat{Y}_1(\omega) &\cong A(\omega)D_1(\omega) \\
\hat{Y}_2(\omega) &\cong A(\omega)D_2(\omega)\exp(-j\frac{d}{v_p}\omega)
\end{aligned}
\tag{3.6}
$$

where $A(\omega)$ is the nominal factor that denotes the complex Doppler dependencies (encoding the varying distance between the platform and the target), $\mathbf{D}_i$ is the antenna pattern vector with the Doppler frequency ω for the $i-$th channel, d is the baseline between two channels and v_p is the platform velocity.

Furthermore, we consider the signals with the range frequencies and extend the equations (3.6) to the Doppler and range frequency domain. The phase histories can be expressed with [113]:

$$\hat{Y}_1(\omega, \Omega) \cong A(\omega)Q_1(\Omega)D_1(\omega)$$

$$\hat{Y}_2(\omega, \Omega) \cong A(\omega)Q_2(\Omega)D_2(\omega)\exp(-j\frac{d}{v_p}\omega) \tag{3.7}$$

where $\mathbf{Q}_i$ is the channel-dependent term (antenna transfer function) for the $i-$th channel with the range frequency Ω.

In the multi-channel SAR settings, based on (3.7), the Fourier transformed signal in the continuous Doppler and range frequency domain (ω, Ω) can be formulated as the following generic form for the $i-$th channel [113]:

$$\hat{Y}_i(\omega, \Omega) \cong A(\omega)Q_i(\Omega)D_i(\omega)\exp(-j\frac{(i-1)d}{v_p}\omega) \tag{3.8}$$

which is the Fourier transformed $\mathbf{Y}_i$ as described in the Chapter 2. This approximation holds when the observed scene is dominated by the stationary background as the motion parameters will be reflected in the varying range between the target and platform.

From (3.8) it is shown that the Doppler related terms are approximately independent to the range frequency related terms [113]. Therefore, the phase histories can be calibrated with two functions in azimuth and range directions, e.g. the $H_{az}(\omega)$ and $H_{rg}(\Omega)$ in (3.9), to acquire the same responses from static reflectors for a pair of channels. The calibration functions for the $i-$th and $k-$th channels can be formulated as:

$$H_{az}(\omega) = \frac{D_i(\omega)}{D_k(\omega)}e^{j(k-i)\omega d/v_p}$$

$$H_{rg}(\Omega) = \frac{Q_i(\Omega)}{Q_k(\Omega)} \tag{3.9}$$

For the $i-$th and $k-$th SAR channels, the phase history for the $k-$th channel can then be balanced via $\hat{Y}_k \odot \mathbf{H}$ where $H(\omega, \Omega) = H_{az}(\omega)H_{rg}(\Omega)$. We therefore have the channel balancing matrix $\mathbf{H}$ as a rank one matrix. The balanced phase histories can be transformed back to the (f_k, τ_n) domain via an inverse Fourier transform, and we denote the pre-processed phase histories of the $k-$th channel as $\widetilde{Y}_k = \mathcal{F}^{-1}(\hat{Y}_k \odot \mathbf{H})$. Therefore, the channel balancing can be performed pair-wise. The channel balancing step plays a vital role in subtractive GMTI algorithms such as DPCA and ATI which pick up moving targets through the coherent differences between channels.

Inaccurate calibrations will lead to imperfect subtractions and increase the false alarm rates. In practice **H** can be estimated via:

$$\min_{\mathbf{H}} \quad \frac{1}{2}\|\hat{\mathbf{Y}}_i - \hat{\mathbf{Y}}_k \odot \mathbf{H}\|_F^2$$
$$s.t. \quad H(\omega, \Omega) = H_{az}(\omega)H_{rg}(\Omega)$$

(3.10)

A viable solution is presented in [113] to tackle (3.10):

$$H_{az}(\omega) = \frac{\int \hat{Y}_k^*(\omega, \Omega)\hat{Y}_i(\omega, \Omega)\, d\Omega}{\int |\hat{Y}_k(\omega, \Omega)|^2\, d\Omega}$$
$$H_{rg}(\Omega) = \frac{\int \hat{Y}_k^*(\omega, \Omega)\hat{Y}_i(\omega, \Omega)\, d\omega}{\int |\hat{Y}_k(\omega, \Omega)|^2\, d\omega}$$

(3.11)

With the equations (3.11), $\hat{\mathbf{Y}}_k$ can be calibrated via $\hat{\mathbf{Y}}_k \odot \mathbf{H}$. This calibration can be implemented iteratively by feeding the updated $\hat{\mathbf{Y}}_k$ into (3.11) again. We keep updating the channel balancing matrix **H** until it does not change significantly. Practically the calibration is realised efficiently within few estimations. Note that more azimuth samples lead to refined accuracy in estimating $H_{rg}(\Omega)$. However, applying this method to the SAR data directly often encounters large azimuth sidelobes. In practice, high fidelity will be preserved only for the azimuth samples in low frequencies as $H_{az}(\omega)$ has significant attenuation in amplitudes with azimuth frequencies. This effect can be visualised in the experimental results of this chapter. The problem can be solved by employing a large sub-aperture to calibrate the channel imbalances, and applying a small subset to implement GMTI each time for rapid responses. In this thesis we estimate $H_{az}(\omega)$ and $H_{rg}(\Omega)$ over sub-apertures, and only utilise a number of low frequency samples in $H_{az}(\omega)$.

3.3.2 Channel Spacing Estimation

Besides the channel imbalance calibration, another challenges arises in practical SAR/GMTI applications to estimate the spacing between different channels. Particularly, this channel spacing information is not available in the AFRL GOTCHA GMTI challenge dataset [4]. It can be seen from (3.9) that the phases of $H_{az}(\omega)$ has a significant linear phase component with ω (can be visualised in the section of experimental results), and the linear slope S_{az} is proportional to the channel spacing d. Therefore, based on the estimated $\mathbf{H}_{az}$ in (3.11), d/v_p can be approximated. Consider the discrete signals with normalised frequencies, if the platform velocity v_p is known,

we can estimate the distance between two channels d via:

$$d = \frac{S_{az} N_D v_p}{2\pi f_{PRF}} \tag{3.12}$$

where N_D denotes the number of azimuth samples. This formulation can be used to approximate the SAR system specification d in SAR/GMTI applications which is crucial in the estimation of moving target states. For example, it is widely known that the radial velocity of a moving target $v^{(r)}$ can be approximated via:

$$v^{(r)} = -P_t \frac{v_p c}{4\pi d f_0} \tag{3.13}$$

where P_t is the phased difference in the SAR image domain between the neighbouring channels which are spatially spaced by d, v_p is the platform velocity, and f_0 is the central range frequency.

3.4 DEM-aided SAR

3.4.1 DEM Extraction

The compatible DEM information has to be extracted in order to match the configurations of specific SAR-based GMTI applications. Therefore, a calibration step is necessary before the exploitation of the DEM in SAR/GMTI processings. Generally the rough DEM data of a regular grid can be retrieved from available DEM sources, and the dataset is usually in the lla (latitude, longitude, altitude) model. This rough DEM model is first translated into meters and we denote the retrieved DEM as $(\mathbf{X}_{coarse}, \mathbf{Y}_{coarse}, \mathbf{E}_{coarse})$ where $(\mathbf{X}_{coarse} \in \mathbb{R}^{N_d}, \mathbf{Y}_{coarse} \in \mathbb{R}^{N_d})$ denotes a grid on the xy-plane, N_d is the dimension of the grid elements, and $\mathbf{E}_{coarse} \in \mathbb{R}^{N_d}$ are the corresponding elevation values.

The task is to find a reference point $(X_{ref}, Y_{ref}, E_{ref})$ for $(\mathbf{X}_{coarse}, \mathbf{Y}_{coarse}, \mathbf{E}_{coarse})$ so that the complete DEM can be estimated with a shift $(\mathbf{X}_{coarse} - X_{ref}, \mathbf{Y}_{coarse} - Y_{ref}, \mathbf{E}_{coarse} - E_{ref})$ followed by the interpolation on the desired grid (x_m, y_l). The complete DEM is thus $\mathbb{G}_{ml} = (x_m, y_l, z_{ml})$ where $m = \{1, 2, ..., M\}, l = \{1, 2, ..., L\}$.

Let us assume that we hold the ground truth GPS information for parts of the terrain map $(\mathbf{X}_t, \mathbf{Y}_t, \mathbf{E}_t)$, where $(\mathbf{X}_t \in \mathbb{R}^{N_d}, \mathbf{Y}_t \in \mathbb{R}^{N_d})$ contains the xy positioning information and $\mathbf{E}_t \in \mathbb{R}^{N_d}$ are the corresponding z coordinates. The reference point $(X_{ref}, Y_{ref}, E_{ref})$ can then be estimated

based on these ground truth data. In particular, we search for the reference point with which the reflectors $(\mathbf{X}_t, \mathbf{Y}_t, \mathbf{E}_t)$ best matches the DEM. Therefore, the estimation of the reference point can be realised via an optimisation problem:

$$\min_{X_{ref}, Y_{ref}, E_{ref}} \frac{1}{2} \|\mathbf{E}_t - \Gamma(\mathbf{X}_{coarse} - X_{ref}, \mathbf{Y}_{coarse} - Y_{ref}, \mathbf{E}_{coarse} - E_{ref}, \mathbf{X}_t, \mathbf{Y}_t)\|_2^2 \quad (3.14)$$

where the operator $\Gamma(\mathbf{X}_{raw}, \mathbf{Y}_{raw}, \mathbf{Z}_{raw}, \mathbf{X}_{new}, \mathbf{Y}_{new})$ linearly interpolates the surface $(\mathbf{X}_{raw} \in \mathbb{R}^{N_d}, \mathbf{Y}_{raw} \in \mathbb{R}^{N_d}, \mathbf{Z}_{raw} \in \mathbb{R}^{N_d})$ at the query points $(\mathbf{X}_{new} \in \mathbb{R}^{N_d}, \mathbf{Y}_{new} \in \mathbb{R}^{N_d})$, and returns the estimated elevation values. Simply speaking, this optimisation is finding the $(X_{ref}, Y_{ref}, E_{ref})$ to best match $(\mathbf{X}_{coarse} - X_{ref}, \mathbf{Y}_{coarse} - Y_{ref}, \mathbf{E}_{coarse} - E_{ref})$ with $(\mathbf{X}_t, \mathbf{Y}_t, \mathbf{E}_t)$.

This optimisation problem (3.14) has limited feasible space and the estimations can be explicitly realised via a local exhaustive search in a specific region. We simply select the $(X_{ref}, Y_{ref}, E_{ref})$ that gives the best match. After the $X_{ref}, Y_{ref}, E_{ref}$ have been computed, we subsequently establish the complete DEM $\mathbb{G}_{ml} = (x_m, y_l, z_{ml})$ through:

$$z_{ml} = \Gamma(\mathbf{X}_{coarse} - X_{ref}, \mathbf{Y}_{coarse} - Y_{ref}, \mathbf{E}_{coarse} - E_{ref}, x_m, y_l) \quad (3.15)$$

3.4.2 DEM-aided Moving Target Imaging

In this section we aim to integrate the DEM into the SAR imaging algorithm. Particularly our investigation focuses on how the DEM interacts with the widely used back-projection SAR imaging. Given the pre-processed phase histories $\widetilde{\mathbf{Y}}_i(f_k, \tau_n)$, the standard back-projection imaging algorithm [51] without DEM works with the equation:

$$\dot{\mathbf{X}}_i(m, l) = \sum_{k=1}^{K} \sum_{n=1}^{N} \widetilde{\mathbf{Y}}_i(f_k, \tau_n) \exp\left(\frac{j4\pi f_k \Delta \dot{\mathbf{R}}_{mln}}{c}\right) \quad (3.16)$$

in which the differential ranges $\Delta \dot{\mathbf{R}}_{mln}$ are formulated as:

$$\Delta \dot{\mathbf{R}}_{mln} = \|\mathbf{r}(\tau_n) - \dot{\mathbb{G}}_{ml}\|_2 - \mathbf{R}_0(\tau_n) \quad (3.17)$$

where $\mathbf{r}(\tau_n)$ refers to the platform position at τ_n (equivalent to the first channel position here as the phase histories have been calibrated based on this channel), $\dot{\mathbb{G}}_{ml} = (x_m, y_l, 0)$ denotes the conventional 2D imaging grid without DEM, and $\mathbf{R}_0(\tau_n) = \|\mathbf{r}(\tau_n) - \mathbf{r}_{ref}\|$ is the distance as a function of azimuth time between the platform and a reference point $\mathbf{r}_{ref}$ (usually the scene

center).

Within this thesis we employ a fast back projection approach with three levels of recursions and decimation in image [1] for the SAR imaging operator Φ_B^0 which is an accurate and efficient approximation of (3.16). With the 5400×400 phase history and 4000×3000 SAR image, we compare the complexities of the forward and backward operators with an Intel Xeon 2.00GHz $\times 32$ machine and Linux Matlab working environment. The results can be found in Table 3.1.

Table 3.1: The complexities of the efficient SAR operators [1] in Elapsed Time (s).

	Forward (re-projection)	Backward (back-projection)
Basic with single-thread (s)	4353	3730
Basic with multi-thread (s)	49	32
Decimation in Image with multi-thread (s)	27	22
Decimation in Phase History with multi-thread (s)	15.5	12.7

It can be seen from Table 3.1 that the acceleration from single-thread to multi-thread is remarkable. With the multi-thread configuration, the fast back projection algorithms furthers the efficiency significantly. Moreover, we implement the decimation-in-image algorithm because it brings higher image quality than the decimation in phase history one. This efficient operator has achieved significant acceleration in the processing which is crucial for a variety of SAR/GMTI applications. Through this thesis, we have adapted all the proposed SAR/GMTI operators to be consistent with this efficient approach to benefit from the significant acceleration.

By injecting the DEM information to the standard back-projection imaging approach (3.16), we can implement an extension to set up the DEM-aided back-projection:

$$\mathbf{X}_i(m,l) = \sum_{k=1}^{K} \sum_{n=1}^{N} \widetilde{\mathbf{Y}}_i(f_k, \tau_n) \exp\left(\frac{j4\pi f_k \Delta \mathbf{R}_{mln}}{c} \right) \tag{3.18}$$

where $\Delta \mathbf{R}_{mln}$ are the DEM-augmented differential ranges:

$$\Delta \mathbf{R}_{mln} = \|\mathbf{r}(\tau_n) - \mathbb{G}_{ml}\|_2 - \mathbf{R}_0(\tau_n) \tag{3.19}$$

in which $\mathbb{G}_{ml} = (x_m, y_l, z_{ml})$ is the estimated DEM with the aforementioned method.

The DEM-aided back-projection can be further extended by considering the moving

reflectors. Given the global M-by-L-by-3 velocity map $\mathbf{V}_{ml} = (\mathbf{V}_{ml}^{(x)}, \mathbf{V}_{ml}^{(y)}, \mathbf{V}_{ml}^{(z)})$ which corresponds to the grid of the monitored region, the equation (3.18) can be extended to the DEM-aided back-projection with the full velocity map:

$$\breve{\mathbf{X}}_i(m,l) = \sum_{k=1}^{K} \sum_{n=1}^{N} \widetilde{\mathbf{Y}}_i(f_k, \tau_n) \exp\left(\frac{j4\pi f_k(\|\mathbf{r}(\tau_n) - \mathbb{G}_{ml} - \mathbf{V}_{ml}\tau_n\| - \mathbf{R}_0(\tau_n))}{c} \right) \qquad (3.20)$$

Note that the differential ranges in equations (3.16) and (3.18) have similar structures and they can be naturally embedded in the fast SAR imaging mechanism [1] for efficient implementation. However, the equation (3.20) is introducing the term $\mathbf{V}_{ml}\tau_n$ which is the function of the physical locations (m,l) and azimuth time τ_n. It is widely known that a moving target at (m,l) will be detected at a different location in SAR/GMTI. In this way the true location of this target is unknown. Before we can employ the back-projection in (3.20), the velocities have to be correctly associated with the physical locations. Practically, it is challenging to establish the exact mappings between them (the target locations change in the SAR images as a function of their velocities).

Furthermore, we aim to benefit from the significant acceleration of the fast back projection algorithm [1] and tend to develop the DEM-aided back-projection with target velocities in a consistent way. Although in general it is not possible to extend the fast back-projection to include arbitrary velocities, for the specific case where we have a single velocity vector, e.g. when we are imaging a single moving target, then the fast back-projection can be modified to incorporate this.

For these reasons, we simplify the DEM-aided back-projection with the full velocity map to the image formation of one moving target. We denote the phase history of the single moving target as $\mathbf{Y}_t(f_k, \tau_n)$ which corresponds to a small subsection of the data that only contains this moving target. Let the velocity vector of this target be $\mathbf{v}_t = (v^{(x)}, v^{(y)}, v^{(z)})$, the DEM-aided moving target imaging can be formulated as:

$$\mathbf{X}_t(m,l) = \sum_{k=1}^{K} \sum_{n=1}^{N} \mathbf{Y}_t(f_k, \tau_n) \exp\left(\frac{j4\pi f_k(\|\mathbf{r}(\tau_n) - \mathbb{G}_{ml} - \mathbf{v}_t\tau_n\| - \mathbf{R}_0(\tau_n))}{c} \right) \qquad (3.21)$$

When we have the velocity vector $\mathbf{v}_t$ of this single target, $\mathbf{r}(\tau_n)$ can be merged with $\mathbf{v}_t\tau_n$ as a function of the azimuth time τ_n. This mathematical structure (3.21) enables the image formation to be consistent with the fast algorithms [51] [1].

When we only have the estimated radial velocity of the target instead of having its full

velocity vector, a variant of the equation (3.21) can be formulated :

$$\mathbf{X}_t(m,l) = \sum_{k=1}^{K} \sum_{n=1}^{N} \mathbf{Y}_t(f_k, \tau_n) \exp\left(\frac{j4\pi f_k \Delta \mathbf{R}'_{mln}}{c}\right) \tag{3.22}$$

in which the enhanced differential ranges $\Delta \mathbf{R}'_{mln}$ is approximated with:

$$
\begin{aligned}
\Delta \mathbf{R}'_{mln} &\cong \|\mathbf{r}(\tau_n) - \mathbb{G}_{ml}\| + v^{(r)}\tau_n - \mathbf{R}_0(\tau_n) \\
&= \|\mathbf{r}(\tau_n) - \mathbb{G}_{ml}\| - \mathbf{R}'_0(\tau_n)
\end{aligned} \tag{3.23}
$$

where $\mathbf{R}'_0(\tau_n) = \mathbf{R}_0(\tau_n) - v^{(r)}\tau_n$, and $v^{(r)}$ stands for the radial velocity with which the target moves away from the platform. This approximation is valid under the assumption that the first term in the differential range represents the varying distance between the platform and the (m, l) cell.

In this thesis the moving target imaging is realised with (3.21) and (3.22). It can be seen that the target velocity can be naturally embedded in the fast SAR imaging mechanism [1] by fixing the differential ranges with pre-calculated constant vectors. The enhanced imaging operator $\Phi_B^{\mathbf{v}_t}$ using the single target velocity vector and the DEM is realised via (3.21), while $\Phi_F^{\mathbf{v}_t}$ is realised via its Hermitian transposes.

3.5 Experimental Results

3.5.1 Channel Balancing using Real Data

We now focus on the AFRL GOTCHA GMTI challenge dataset to demonstrate the performance of this channel balancing method. We start from the pulse number 96017 and extract the phase histories with different number of azimuth pulses (400, 800, 1500, 2000, 3000, and 5000 respectively). The amplitudes and phases of the calibration matrices are shown in Fig. 3.1 and Fig. 3.2.

It can be seen from (3.9) that the phases of the azimuth calibration function change with ω linearly. This feature can be used to estimate the channel spacing as discussed in section 3.3.2. This linearity is clearly depicted in the right column of Fig. 3.1. Moreover, with more azimuth samples, the azimuth calibration does not change significantly as shown in Fig. 3.1. However, more azimuth pulses can smooth the range calibration function as shown in Fig. 3.2. This is
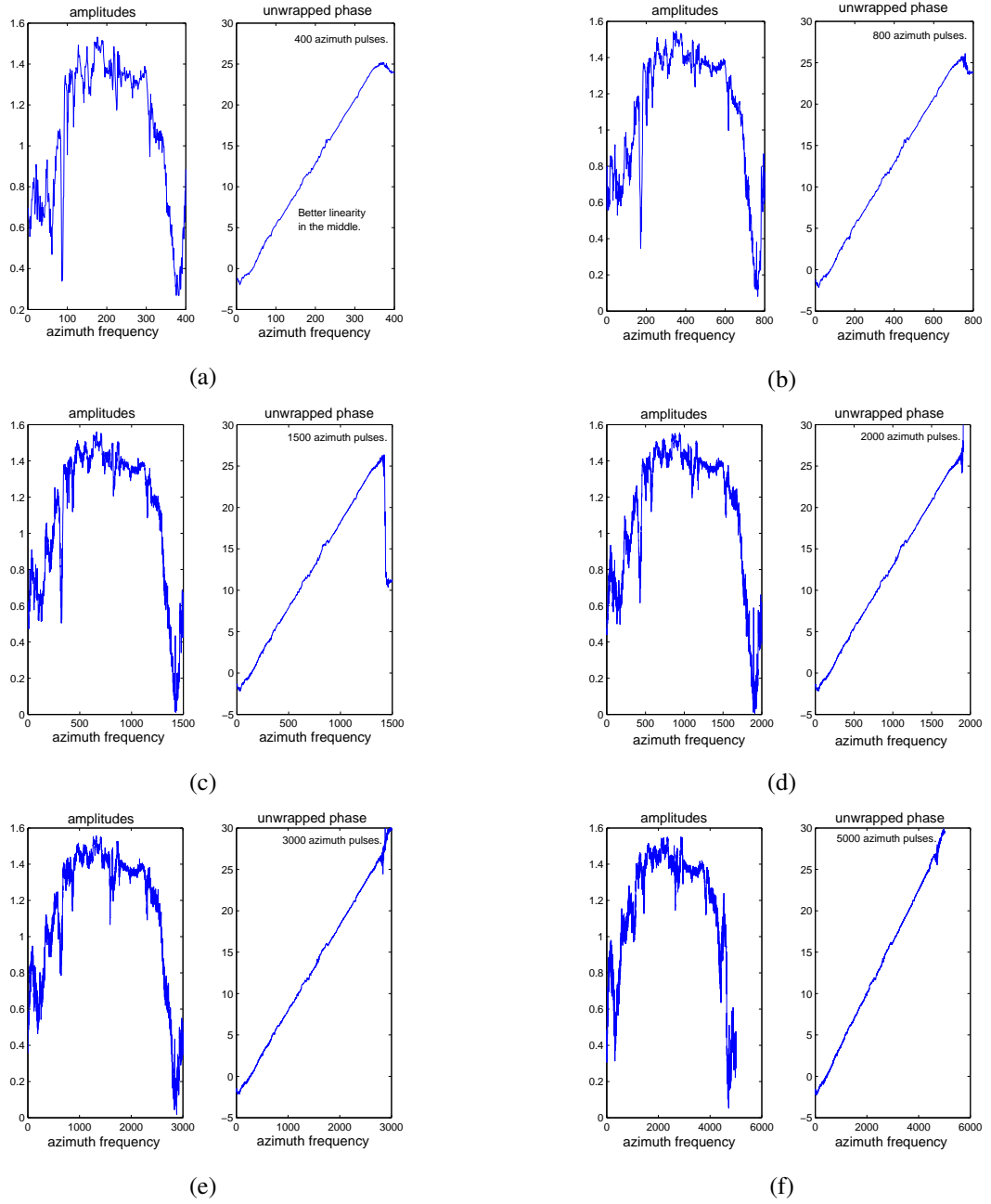
Figure 3.1: The amplitudes and phases of the rank-1 calibration matrix in azimuth direction with a) 400 b) 800 c) 1500 d) 2000 e) 3000 f) 5000 azimuth pulses respectively.
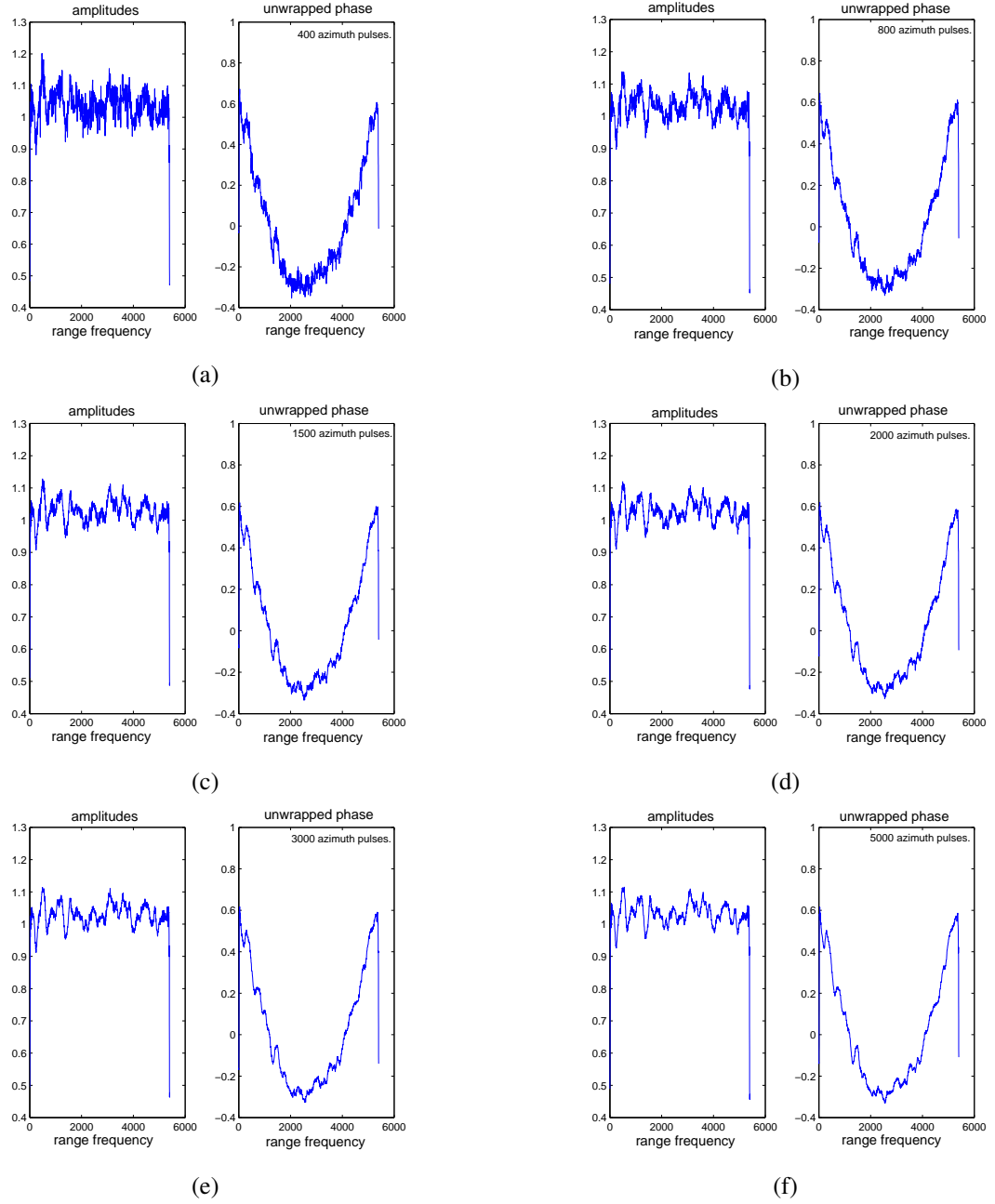
Figure 3.2: The amplitudes and phases of the rank-1 calibration matrix in range direction with a) 400 b) 800 c) 1500 d) 2000 e) 3000 f) 5000 azimuth pulses respectively.
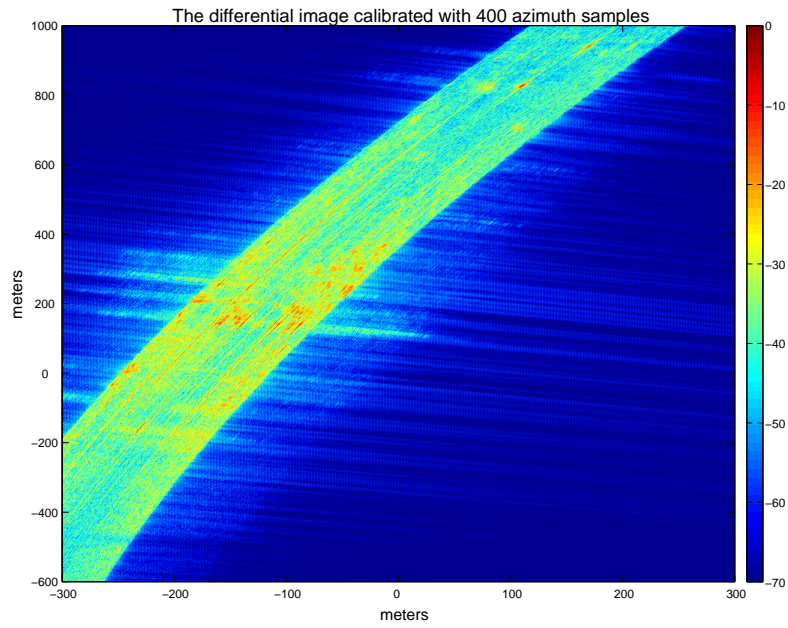
(a)
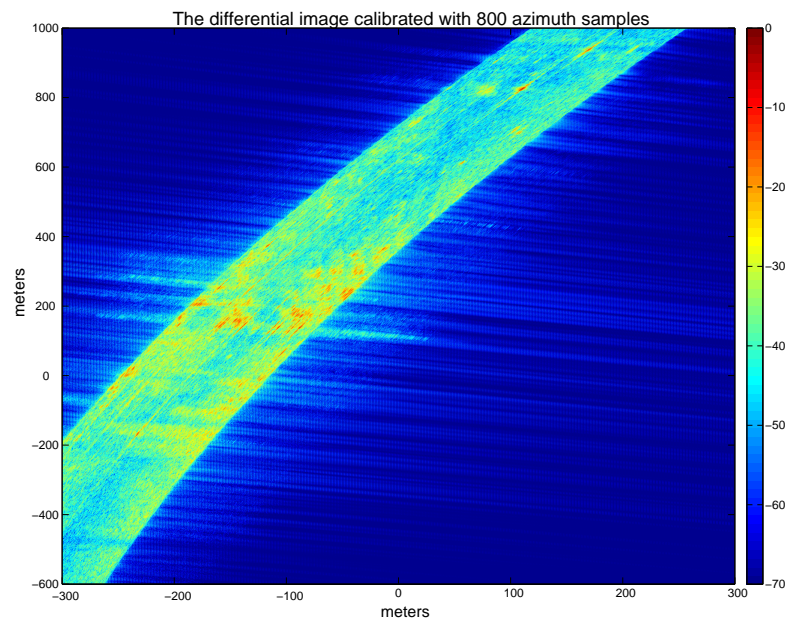
(b)

Figure 3.3: I. Differential image of the first two channels using 400 azimuth samples but calibrated with 400 and 800 azimuth samples. The sidelobes of the reflectors along the azimuth direction are significantly mitigated by calibrating with more azimuth samples.
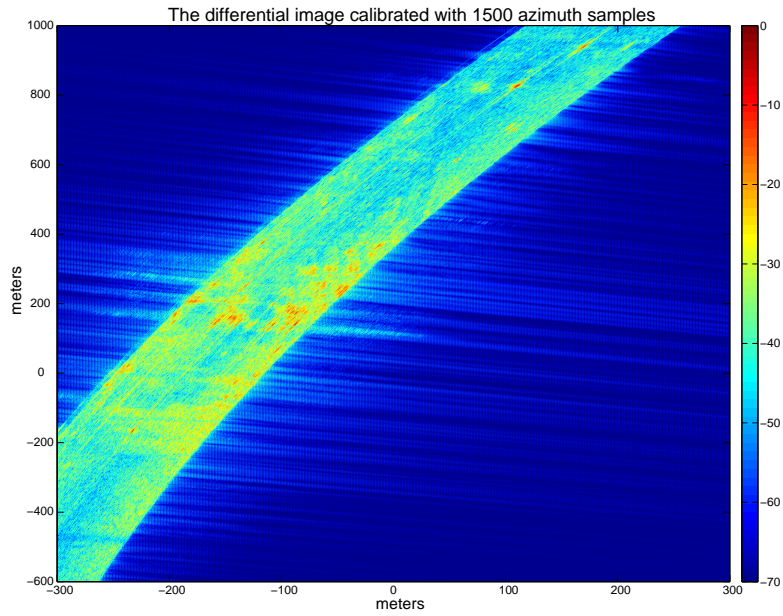
(c)
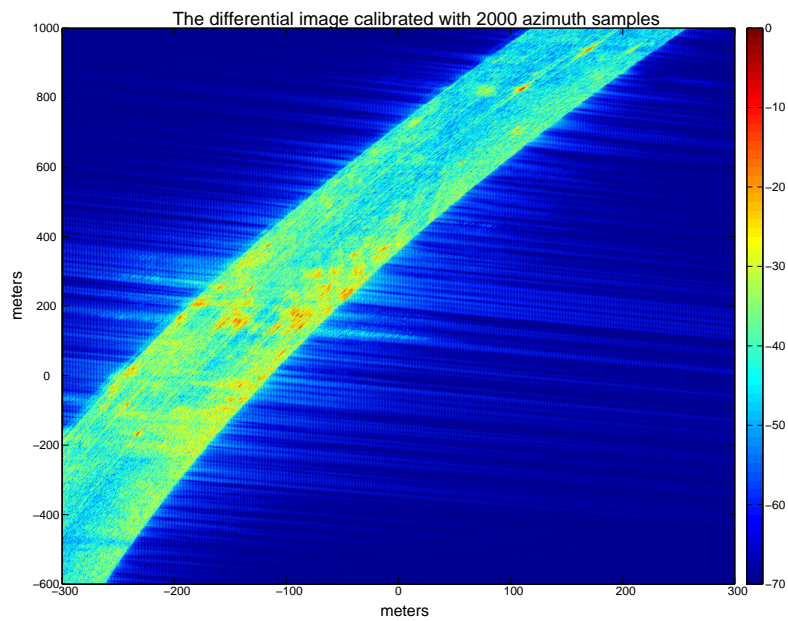
(d)

Figure 3.3: II. Differential image of the first two channels using 400 azimuth samples but calibrated with 1500 and 2000 azimuth samples. The sidelobes of the reflectors along the azimuth direction are significantly mitigated by calibrating with more azimuth samples.

(e)

(f)

Figure 3.3: III. Differential image of the first two channels using 400 azimuth samples but calibrated with 3000 and 5000 azimuth samples. The sidelobes of the reflectors along the azimuth direction are significantly mitigated by calibrating with more azimuth samples.

(a)

(b)

Figure 3.4: The comparison between differential image of first two channels and the first channel image using 400 azimuth samples. (calibrated with 20000 samples)

further validated through Fig. 3.3.

In Fig. 3.3, from I to III, the differential images of the first two channels are visualised with increasing number of azimuth samples for channel calibration. As expected, the sidelobes of the reflectors along the azimuth direction are significantly mitigated by calibrating with more azimuth samples, and the improvements are less significant in the range direction. Moreover, it is well known that conventional DPCA results (differential SAR images) tends to predict moving targets for strong discrete structures such as buildings because of their imbalanced magnitudes between different channels [98]. To demonstrate this effect, we compare the differential image of the first two channels to the formed S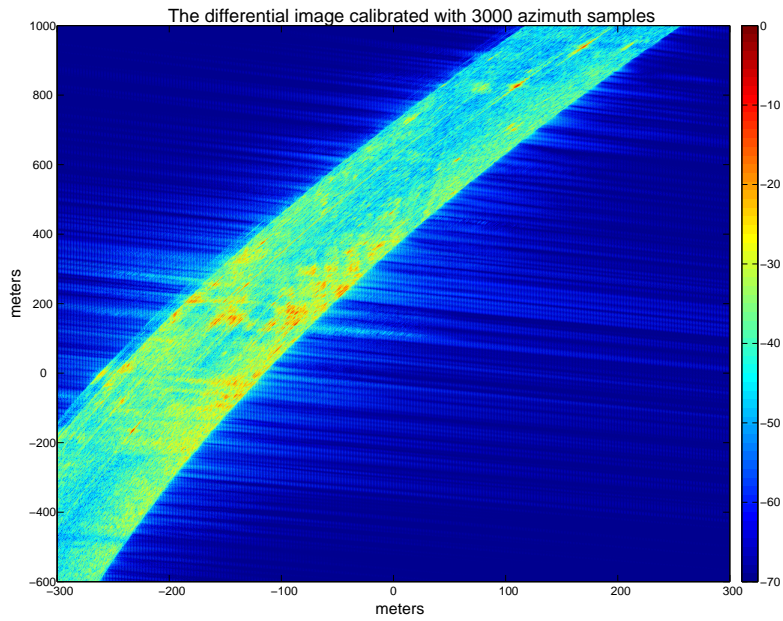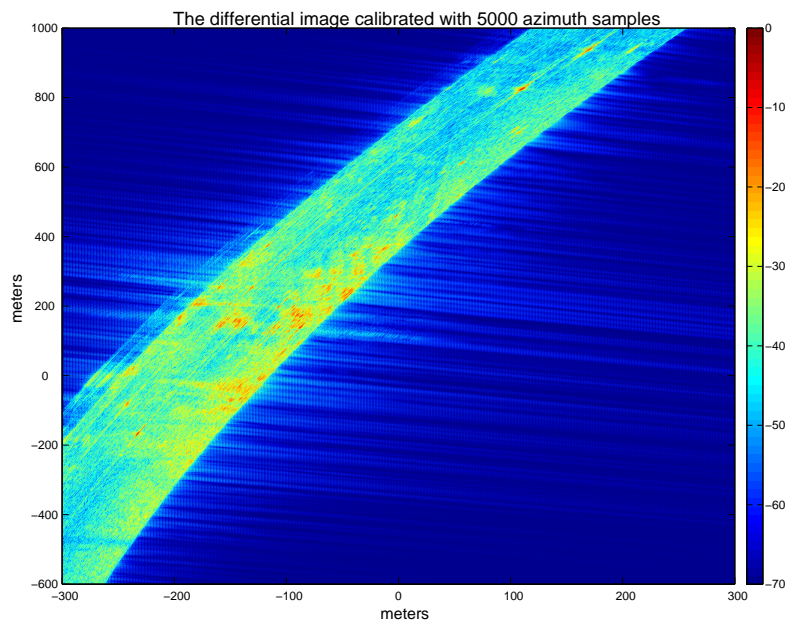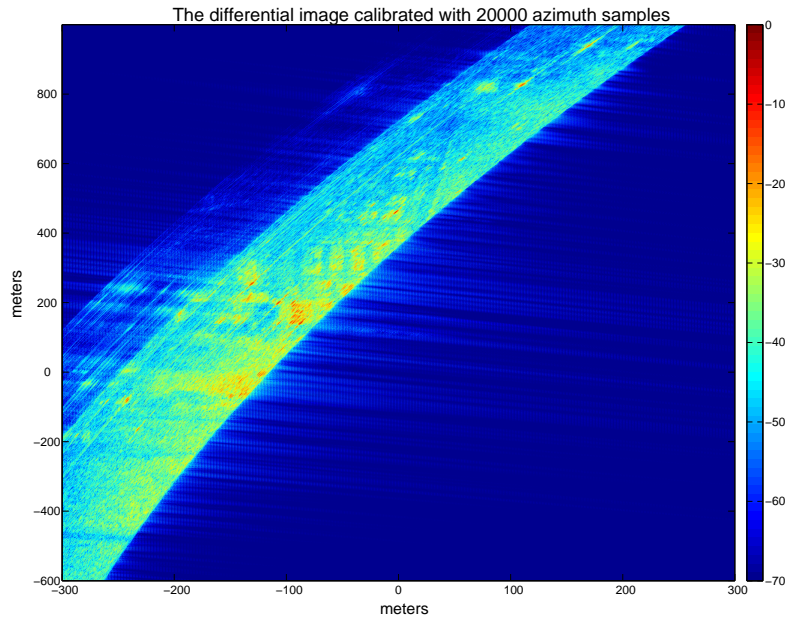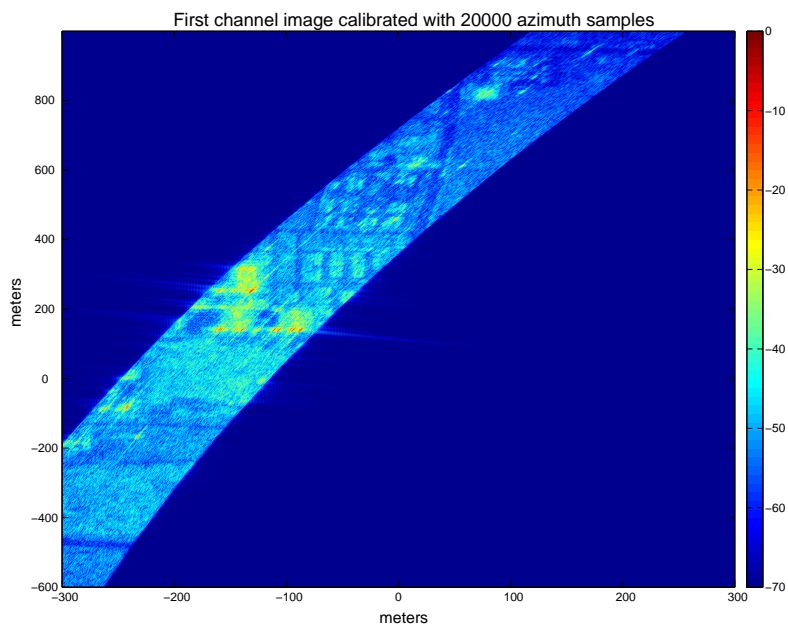AR image of the first channel using 400 azimuth samples but calibrated with 20000 azimuth samples. The comparison is visualised in Fig. 3.4. Note that this comparison is done via the direct implementation of the channel balancing just to show the effects of azimuth pulse numbers and strong discrete reflectors.

It can be seen from Fig. 3.1 that magnitudes in the sidelobes of the calibration matrices have strong degradations, and a viable solution is to only calibrate the low frequencies. The direct implementation of this channel balancing approach thus encounters large azimuth sidelobes. Furthermore, it is shown in Fig. 3.1 that the linearity of the phases of azimuth calibration function is better in the middle part. This issue can be solved by employing a large sub-aperture dataset to calibrate the channels, and applying a small subset to implement GMTI each time for rapid responses. In practice, for the subsequent processing of this dataset, we employ the channel balancing approach with 8000 azimuth pulses and preserve the calibration functions only for the 800 samples in the middle which achieves better calibrations. In addition, this calibration matrix is used along with (3.12) in the pair-wise estimation to estimate the channel spacings of the three channels in this dataset. Our estimations show that the three antennas are equally spaced by $d = 0.238m$, and this result coincides with the similar spacing estimates for the same data in [114].

In general, we expect to detect the moving targets based on the channel differences. It can be seen from Fig. 3.4 that most unexpected strong responses correspond to the imperfect channel balancing on strong static buildings (not isotropic). Especially in urban environment, based on the line-of-sight, strong reflections only happen for the sides and corners of the buildings which meet the wave-front of the transmitted signals. In this scenario, further criteria are required to distinguish the moving targets.

The conventional ATI method presents that a moving target will induce a phase difference

between different channels, which is proportional to its radial velocity. A straightforward criterion to be used here is to eliminate those reflectors which have small phase deviations between channels. By employing both amplitude and phase differences we aim to better locate the moving targets and reduce the false alarm rates. A number of recent developments in SAR-based GMTI applications are investigating the proper strategies to incorporate both amplitudes and phase information [100] [98] [92] [93] which are explained in Chapter 2. However, these methods all first require the accurate calibrations between different SAR channels.

3.5.2   DEM-aided SAR using Real Data

DEM Calibration

As the DEM is absent in the original AFRL GOTCHA GMTI challenge dataset, we have to extract the proper DEM data for the experiments. A coarse DEM on a regular 80×60 grid with latitude and longtitude resolution of 0.0240 and 0.0250 respectively, i.e. latitude 39.771 to 39.795 and longitude -84.1 to -84.075, was obtained from the United States Geological Survery (USGS) seamless dataset (rougly 30 meters resolution) [111]. The coarse DEM coverage was initially chosen to be larger than the observed scene of our SAR system for further processing, and the data is in lla (latitude, longtitude, altitude) model. Based on the geometry, it is about 85.45 m for 0.001 degree longitude and 111.2 m for 0.001 degree latitude at that region. We translated the DEM data into meters and show it in Fig. 3.5.

Since the monitored region does not match the retrieved DEM $(\mathbf{X}_{coarse}, \mathbf{Y}_{coarse}, \mathbf{E}_{coarse})$ at this stage, we have to find a reference point $(X_{ref}, Y_{ref}, E_{ref})$ so that the elevation map can be estimated by shifting the $(\mathbf{X}_{coarse}, \mathbf{Y}_{coarse}, \mathbf{E}_{coarse})$ based on this point $(X_{ref}, Y_{ref}, E_{ref})$, and then interpolating on the imaging grid (x_m, y_l). Given that we have the ground truth GPS information of one moving target $(\mathbf{X}_t, \mathbf{Y}_t, \mathbf{E}_t)$, where $(\mathbf{X}_t, \mathbf{Y}_t)$ contains its xy positioning information and $\mathbf{E}_t$ are the corresponding z coordinates, and they form a path on the terrain surface, we can adopt the method aforementioned in section 3.4.1 to estimate the calibrated elevation map, and then interpolate the map on our imaging x-y grid (x_m, y_l) to get z_{ml}. This approach is also published in [5].

The interpolated DEM shifted with the reference point is shown in Fig. 3.6. As shown in the DEM, the monitored region has significant elevation variations. The elevation variation can be as large as 30 meters. We also depict the calibrated DEM along with the path of a moving target in
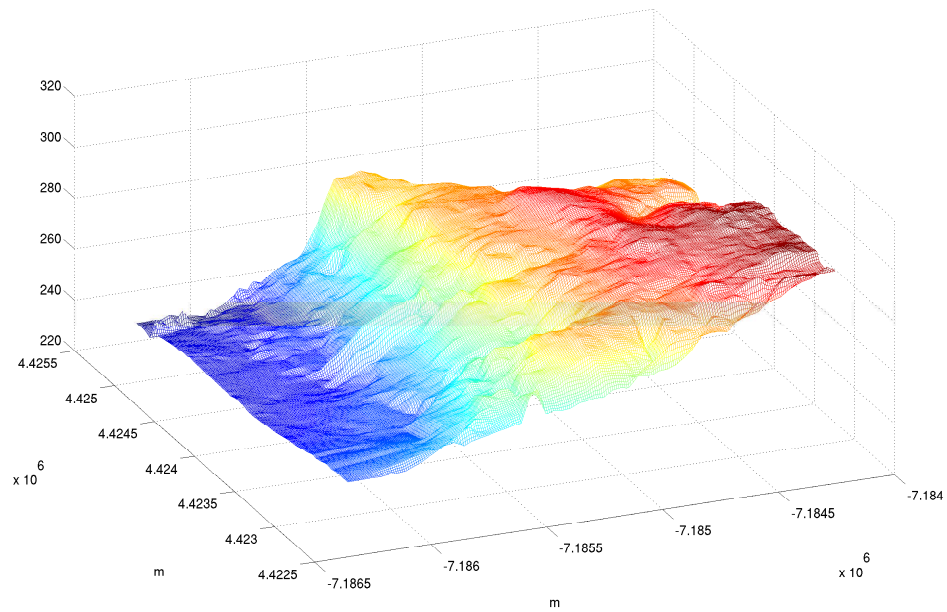
Figure 3.5: The DEM with four times interpolations on both dimensions.
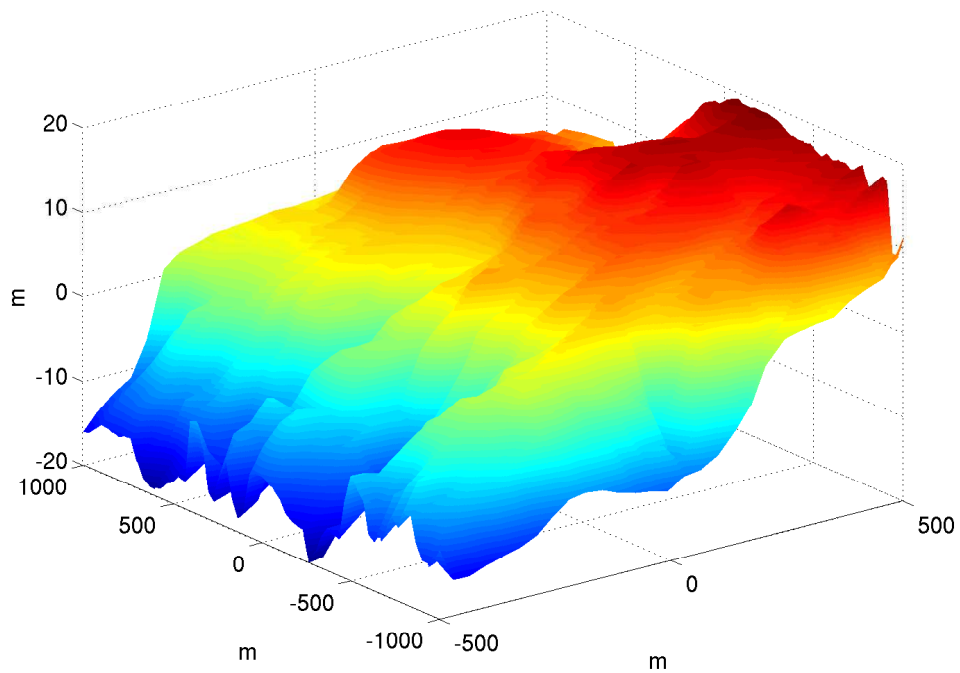
Figure 3.6: The estimated DEM which is associated with the imaging grid.
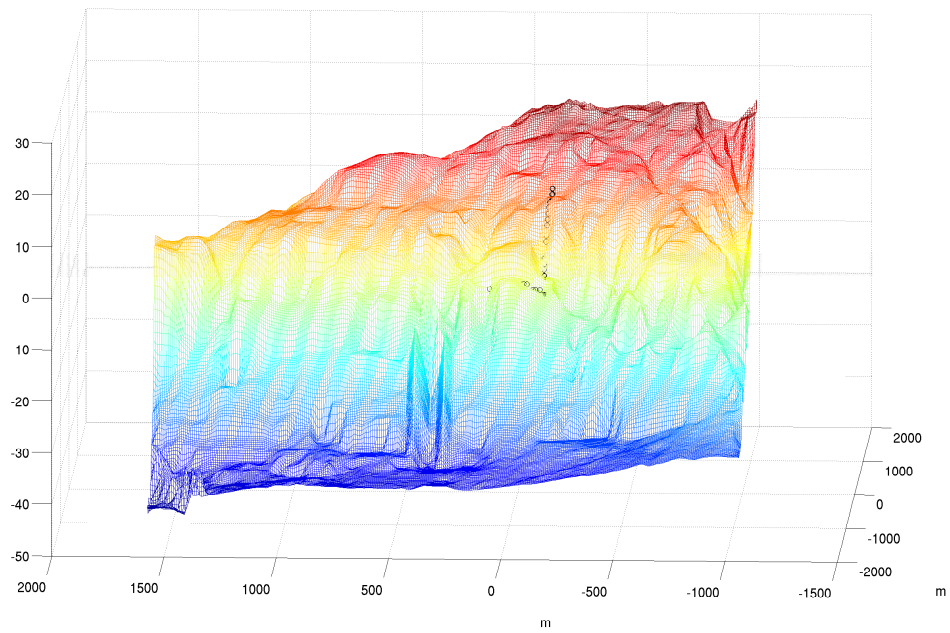
Figure 3.7: The DEM after calibration and the target path. The target path (black circles) match the DEM surface very well.
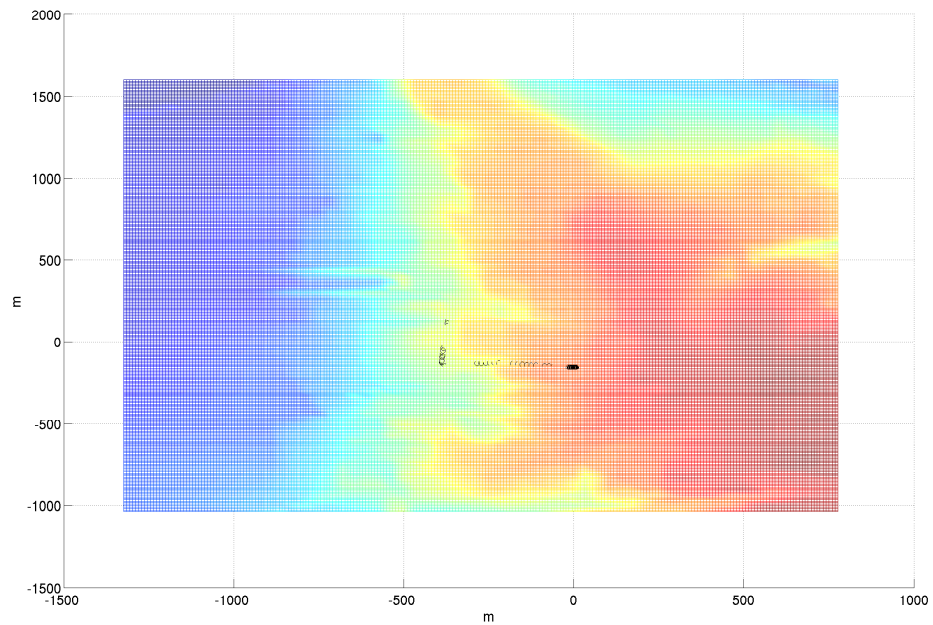
Figure 3.8: The DEM after calibration and the target path. The vehicle goes down a long slope and slows down to turn right. Then it goes across a 'bump'.
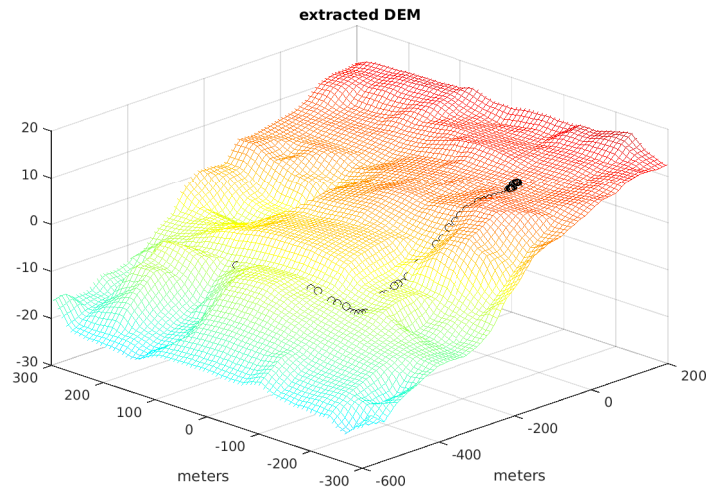
(a)

(b)

Figure 3.9: a) The extracted terrain map. The black circles show the target trajectory. b) The corresponding Google map of this scene. Here we show a roughly extracted map and the coordinates may have small inconsistencies with our formed SAR images.

Fig. 3.7 and Fig. 3.8 from different view angles. It can be seen that the target path matches very well on the surface of extracted DEM. The target path in black circles disappear visually for some segments because that the path is below the estimated DEM surface and the camera is in top-down perspective. The target path corresponds to a slope and a "bump". Furthermore, we compare the reconstructed SAR images without and with the DEM. A further Google map of the monitored region is provides for the visual comparison. The results can be found in Fig. 3.9.
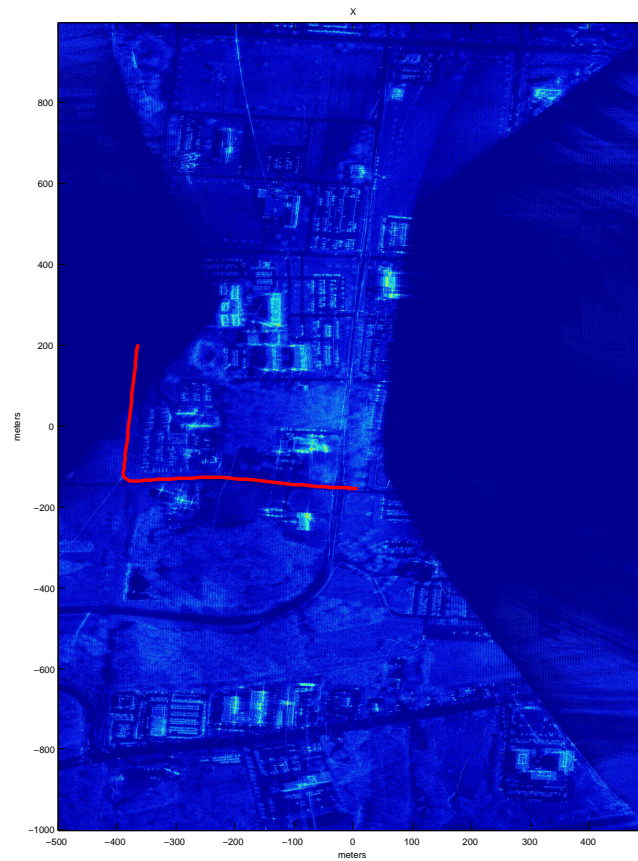
Figure 3.10: The formed high resolution SAR image with the proposed SAR/GMTI framework. The elevation information is utilised. The red path indicates the moving target, and it matches the road very well.

To better explain the illuminated area, we first briefly show the formed high resolution SAR image of the whole scene via Fig. 3.10. This monitored scene is an urban region with significant elevation variations. Based on the ground truth data, the scene is overlaid with the target trajectory illustrated by the red path. With fewer sub-apertures, in Fig. 3.11 and Fig. 3.12, we present the SAR images of the monitored scene without and with the DEM information respectively. They are synthesized using range-gated images generated with (3.18). Here the image quality can be
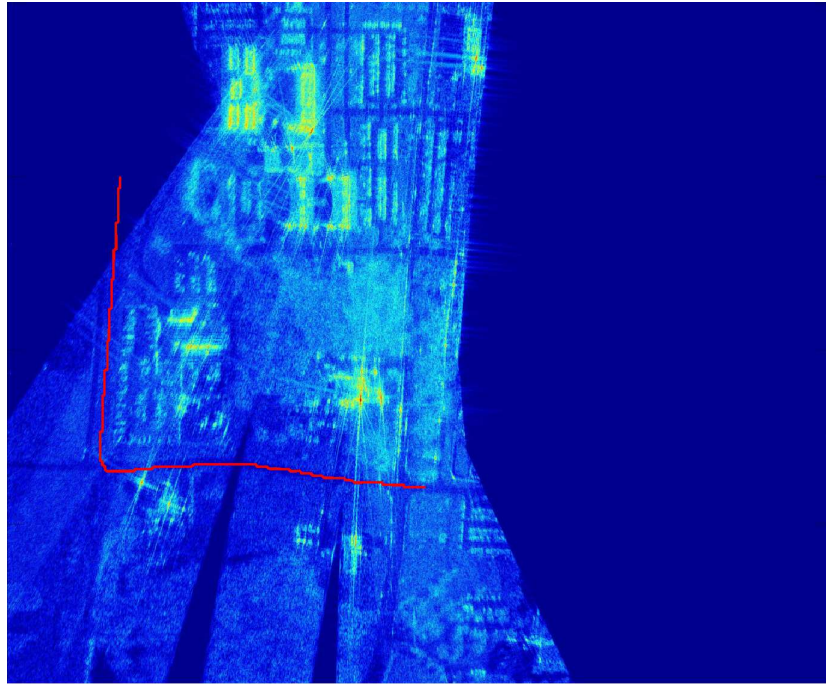
Figure 3.11: The synthesised SAR image of the observed region using the accelerated SAR image formation without DEM correction. The red path indicates a moving target.
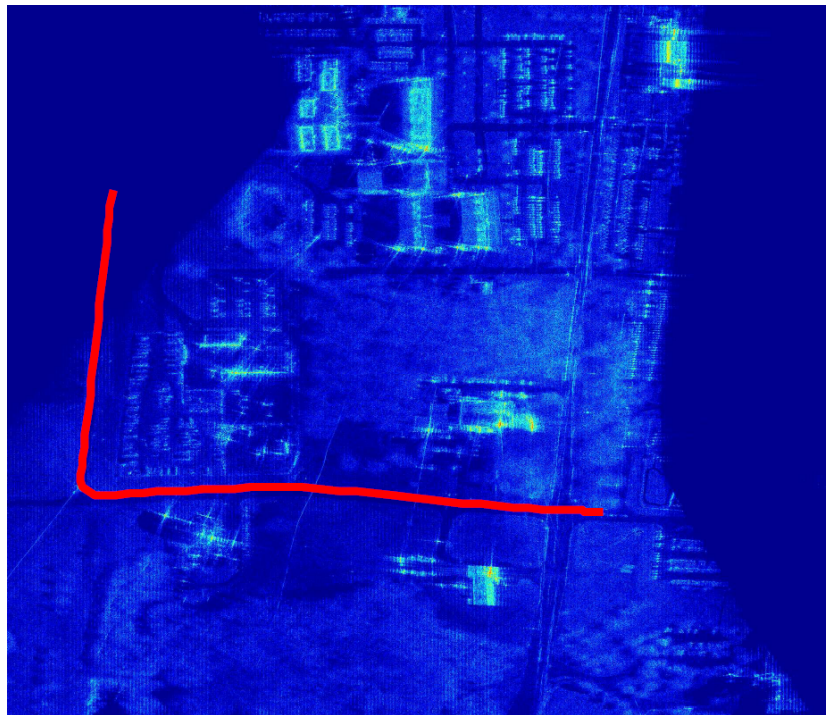
Figure 3.12: The synthesised SAR image of the observed region using the accelerated SAR image formation with DEM correction. The red path indicates a moving target.

(a)

(b)

Figure 3.13: a) and b) The reconstructed SAR image in dB using the range-gated data to show the GMTI scene without and with the DEM respectively. The red path stands for the target trajectory based on the ground truth data.

degraded due to the missing data as described in Chapter 2. It can be seen from Fig. 3.11 that the target path has significant deviations from the road without the DEM data.

To be compared with Fig. 3.11, in Fig. 3.12, we show the formed high resolution image with the proposed SAR/GMTI framework using the extracted DEM information. It can be seen from Fig. 3.12 that the target path matches the road very well. The proposed framework is capable of simultaneously maintaining such high resolution image formation and indicating moving targets. The estimated target states are also very close to the ground truth as will be shown in the experimental results, and the details will be presented through this thesis.

The zoomed-in scenario of Fig. 3.11 and Fig. 3.12 is demonstrated in Fig. 3.13 using seamless sub-apertures. The estimated DEM is employed during the imaging process in Fig. 3.13.b. It can be seen that there can be a displacement of 10 to 20 meters between the road and the target path along the x direction if we do not apply the DEM. It is even demonstrated in Fig. 3.13.b that the moving vehicle is driving by the right side of the road. Also it is shown in Fig. 3.9.a that the observed region has significant elevation variations. We show the corresponding Google map in Fig. 3.9.b. It can be concluded from this figure that the target path is much better aligned with the road in the formed SAR images with the DEM information.

3.6 Summary

In this chapter we addressed two crucial facets in SAR-based GMTI application, i.e. the calibrations between different SAR channels and the exploitation of DEM in SAR/GMTI. We have presented practical channel balancing methods. The effects of the azimuth pulse numbers and strong reflectors are analysed. We also introduce the estimation of channel spacing based on the channel balancing. Furthermore, we present the exploitation of the DEM in SAR-based GMTI applications. Specifically we consider the DEM extraction and DEM-aided moving target imaging in this chapter. We demonstrate the performance of these approaches through the AFRL GOTCHA GMTI challenge dataset. We also discuss about some necessary calibrations with respect to this dataset.

<div align="right">4</div>

Moving Targets and Background Decomposition

4.1 Introduction

Consider a typical airborne SAR scheme, a number of moving vehicles usually exist in the observed scene. The Ground Moving Target Indication (GMTI) techniques can be combined with the SAR imaging approaches discussed in Chapter 3 to pick up moving targets within the formed images. These GMTI methods provide the capabilities of detecting the moving targets within a complex background which are of value for both civil and military applications. The targets can be analysed and their states including the physical positions and velocities can be estimated in the post-processing stages with other advanced signal processing techniques. Given that the background consists of man-made structures, static reflectors, vegetation, moving objects and speckle noise, marking the moving targets especially those buried in the clutter interference is challenging. Furthermore, the basic SAR mechanism assumes a stationary scene, and a moving target will induce displacement and blurring in the formed images.

A multi-channel SAR system gives additional features for GMTI applications compared to single-channel methods. For single-channel approaches, slowly moving targets will result in detection difficulties since their Doppler frequency shifts fall into the endo-clutter spectra, i.e. the Doppler band with non-negligible clutter energy (mainlobe clutter). The multi-channel SAR configuration has better detection capabilities, and it has smaller minimum detectable velocity (MDV) compared to the single-channel mode [93]. It is worth mentioning that conventional multi-channel approaches (such as DPCA,ATI, and STAP) have been proven to work properly under homogeneous clutter. However, for non-homogeneous terrains, such as mountains with large terrain variations and urban regions with strong building scatterers, the aforementioned methods may miss the detections and advanced techniques are needed to be employed [112].

In this chapter we introduce a sparsity based framework for multi-channel SAR-based GMTI applications. A fundamental additive model is assumed, (4.1), such that the SAR image

$\mathbf{X} \in \mathbb{C}^{M \times L}$ can be decomposed into the background image (static reflectors) $\mathbf{X}_s$ and the dynamic image $\mathbf{X}_d$ (moving targets) which is assumed to be sparse.

$$\mathbf{X} = \mathbf{X}_s + \mathbf{X}_d \tag{4.1}$$

By leveraging the sparsities of $\mathbf{X}_d$, i.e. the moving targets are sparse in the monitored scene, the GMTI task can be formulated as a sparsity regularised optimisation problem to separate $\mathbf{X}_d$ from $\mathbf{X}_s$, and estimate the moving target states, i.e. their locations, reflectivities and velocities. Unlike conventional clutter suppression methods such as DPCA and ATI which are mainly based on detecting the moving targets, the presented framework is capable of decoupling the moving target signal and the strong background clutter, and it provides further potential to implement subsequent automatic target recognition (ATR) [17], or even inverse SAR [115] on the extracted moving targets. In addition, the proposed framework is sufficiently versatile to incorporate the DEM which further improves the moving target relocation accuracy, especially when significant elevation variations exist.

Consider the typical SAR-based GMTI tasks of image formation, target indication, and state estimation, the conventional SAR/GMTI systems typically realise these tasks in multiple stages. The proposed sparsity based framework aims to integrate these GMTI goals into an optimisation problem regularised by target sparsities, and it serves as a generic model for tackling these problems which can also incorporate other SAR imaging algorithms. The proposed model thus forms an end-to-end SAR/GMTI framework. Although the integrated model can be established, solving the optimisation problem in practice within one processing stage is very challenging as the target locations change as a function of their estimated velocities. Therefore a practical solution is to employ a compromise and break the problem into a two stage process where we first utilise target sparsities to separate the blurred and misplaced moving targets from the static background scene and subsequently relocate and refocus individual moving targets, again exploiting the sparsity constraint. While the two stage process sacrifices a degree of sparsity (the blurred targets are less sparse than the correctly focused ones), it results in a simpler more tractable problem. We also consider the incorporation of the DEM information throughout the framework and provide solid experimental results via the real AFRL GOTCHA GMTI challenge data. In this Chapter we focus on the moving targets and background separation which can be compared with conventional GMTI algorithms such as DPCA/ATI, and the second stage is subsequently investigated in Chapter 5.

4.2 Moving Targets and Background Decomposition

In this section we introduce the model of the proposed SAR/GMTI framework, and present a practical algorithm for target/background separation and radial velocity estimation. We start by employing the variable splitting approach to the SAR image domain, and denote $\mathbf{X}_s \in \mathbb{C}^{M \times L}$ and $\mathbf{X}_d \in \mathbb{C}^{M \times L}$ as the static background and moving (misplaced and blurred targets) target reflectivities for the first channel respectively. As there are limited number of moving targets in the observed scene, $\mathbf{X}_d$ can be regularised with sparse constraints. Motivated by the fact that the formed images of one moving target between neighbouring channels have a phase difference $(4\pi/c)f_0 v^{(r)}(d/v_p)$ which encodes the target radial velocity (f_0 is the central frequency of the transmitted signal). We can then introduce a phase correction matrix that enables us to describe the dynamic image in the other channels, and specifically $\mathbf{X}_d$ can be assumed to be sparse given that there are typically few spatially localized moving targets in the observed scene ($\mathbf{X}_d$ is assumed to have at most s non-zero entries). Therefore, it is possible to set up a novel sparse-regularised optimization problem for SAR/GMTI tasks, and further auxiliary information (such as the DEM) can be involved in this framework.

Given the pre-processed phase histories $\widetilde{\mathbf{Y}}_i$ and calibrated DEM, the moving targets and background decoupling model is described as:

$$
\begin{aligned}
\min_{\mathbf{X}_s, \mathbf{X}_d, \mathbf{P}} \quad & \frac{1}{2} \sum_i \|\widetilde{\mathbf{Y}}_i - \Phi_F^0(\mathbf{X}_s + \mathbf{X}_d \odot \mathbf{P}^{i-1})\|_F^2 \\
s.t. \quad & \|\mathbf{X}_d\|_0 \le s \\
& \mathrm{supp}(\mathbf{X}_d) = \mathrm{supp}(\mathbf{P}\text{-}\mathbf{1}) \\
& |\mathbf{P}_{ml}| = 1, \ m = 1, \dots, M, \ l = 1, \dots, L
\end{aligned}
\tag{4.2}
$$

where $\mathbf{P} \in \mathbb{C}^{M \times L}$ is the phase correction matrix on $\mathbf{X}_d$ which has element-wise magnitude 1 entries (e.g. the stationary reflectors off the support of $\mathbf{X}_d$ have zero phase shifts $\mathbf{P}_{ml} = \exp(j0) = 1$), the moving target reflectivities in $\mathbf{X}_d$ are assumed to be $s-$sparse, and $\mathrm{supp}(\mathbf{X}_d)$ stands for the support set of $\mathbf{X}_d$ indicating the non-zeros in $\mathbf{X}_d$.

As shown above the radial velocity of the target is encoded in the phase of $\mathbf{P}$. $\mathbf{X}_d$ and $\mathbf{P}$-$\mathbf{1}$ have the same support on the pixels which form the moving targets, and $\mathbf{P}$-$\mathbf{1}$ is thus $s-$sparse as

well. We assume that the channel phase centers are equally spaced and define $\mathbf{P}^i$ as:

$$\mathbf{P}^i = \underbrace{\mathbf{P} \odot \ldots \odot \mathbf{P}}_{i} \tag{4.3}$$

where $i > 0$ and $\mathbf{P}^0 = \mathbf{1}$.

By leveraging the sparsity of the moving targets and maintaining the data fitting fidelity, the presented model (4.2) retrieves the formed images for both moving targets $\mathbf{X}_d$ and background $\mathbf{X}_s$, and simultaneously estimates a phase correction matrix $\mathbf{P}$. Practically $\mathbf{P}$ leads to the direct estimation of the radial velocities of the moving targets (similar to the argument in ATI).

Note that $\mathbf{X}_d$ corresponds to the misplaced and blurred moving targets without considering velocity components. A variant of (4.2) can be formulated by considering full target velocity vectors, and the state estimation of moving targets is thus simultaneously realised in this processing stage. However, the target locations change as a function of their estimated velocities, and we do not have the computational effective forward/backward projection operators [1] to simultaneously image all moving targets. This difficulty drives us to put aside the full target velocity vectors in (4.2) and employ the moving target state estimation in the subsequent processing which we will revisit in Chapter 5. The complete processing pipeline of the proposed SAR/GMTI framework is depicted in Fig. 4.1.
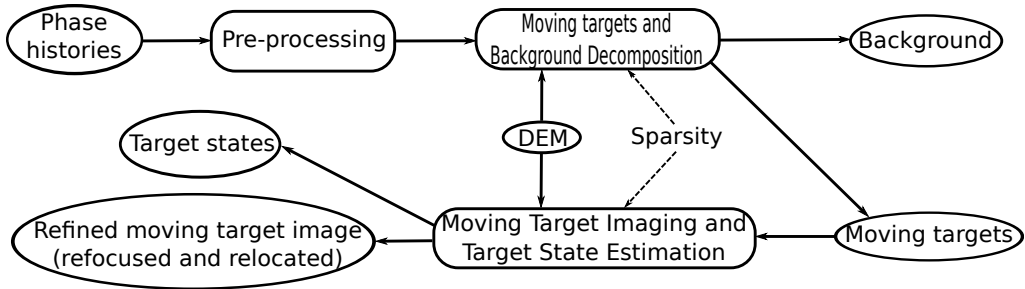
Figure 4.1: The complete processing pipeline of the proposed SAR/GMTI framework.

Since (4.2) is a challenging non-convex optimisation problem, we first reformulate it for a more practical implementation. To simplify tackling this non-convex optimisation, we first introduce the intermediate variables $\mathbf{dX}^1 = \mathbf{X}_d \odot \mathbf{P} - \mathbf{X}_d = \mathbf{X}_d \odot (\mathbf{P} - \mathbf{1})$ and $\mathbf{X}_1 = \mathbf{X}_s + \mathbf{X}_d$. These let us to establish good initialisations with DPCA and ATI algorithms. Particularly $\mathbf{dX}^1$ can be taken as the differences between the SAR images of the $2-$nd and $1-$st channels, and $\mathbf{X}_1$ corresponds to the reconstructed SAR image based on the first channel. Therefore $\mathbf{dX}^1$ and $\mathbf{X}_1$ can be initialised with the DPCA and back-projection algorithms. Now we have the bijective

(both injective and surjective) mapping [116] from the variable set $\{\mathbf{X}_s, \mathbf{X}_d, \mathbf{P}\}$ to $\{\mathbf{X}_1, \mathbf{dX}^1, \mathbf{P}\}$. We then propose an alternating update mechanism on $\mathbf{X}_1$, $\mathbf{P}$ and $\mathbf{dX}^1$ that alternately updates one of them at a time while keeping the others fixed. With I radar channels (4.2) can be rewritten as:

$$
\begin{aligned}
\min_{\mathbf{X}_1, \mathbf{dX}^1, \mathbf{P}} \quad & \frac{1}{2} \|\widetilde{\mathbf{Y}}_1 - \Phi_F^0(\mathbf{X}_1)\|_F^2 + \\
& \frac{1}{2} \sum_{i=2}^{I} \|\widetilde{\mathbf{Y}}_i - \Phi_F^0(\mathbf{X}_1 + \sum_{j=1}^{i-1} \mathbf{dX}^1 \odot \mathbf{P}^{j-1})\|_F^2 \\
s.t. \quad & \|\mathbf{P\text{-}1}\|_0 \leq s \\
& \text{supp}(\mathbf{dX}^1) = \text{supp}(\mathbf{P\text{-}1}) \\
& |\mathbf{P}_{ml}| = 1, \ m = 1, \ldots, M, \ l = 1, \ldots, L
\end{aligned}
\tag{4.4}
$$

Since we have $\|\mathbf{X}_d\|_0 = \|\mathbf{P} - \mathbf{1}\|_0 = \|\mathbf{dX}^1\|_0$ and equal supports, the sparsity constraint can be introduced to assume that $\mathbf{P\text{-}1}$ has no more then s non-zeros.

While we have proposed a more simpler model which only estimates the differential SAR images between channels [10], this evolved model is more complete. Our earlier efforts into approximating the model (4.4) can be found in [6], and the brief idea was leveraging the sparse approximation theory, intermediate variables, and heuristic updates with iterations. However, the heuristic updates do not have the theoretic performance guarantee. To have a more rigorous implementation, we have developed a new algorithm which uses a different intermediate variable set, gradient descent updates and the backtracking mechanism (we re-estimate the variables for an iteration whenever the objective value is not decreased) [117]. We next present the details of the algorithm.

The detailed implementation of the proposed decomposition method can be found in Algorithm 4.2.1. Through the iterations, $\mathbf{X}_1$ is updated along the negative gradient direction, the phase correction matrix $\mathbf{P}$ is updated with gradient decent methods followed by an element-wise projection onto the the unit ball and thresholding operations [118] on $\mathbf{P\text{-}1}$ (the cost function is non-increasing with appropriate step sizes as shown in [119]), and $\mathbf{dX}^1$ is computed using gradient decent methods while its support is limited by $\text{supp}(\mathbf{dX}^1) = \text{supp}(\mathbf{P\text{-}1})$. Throughout the algorithm, the final support of $\mathbf{dX}^1$ and $\mathbf{P\text{-}1}$ are achieved by iteratively thresholding $\mathbf{P\text{-}1}$. As the magnitudes of $\mathbf{P\text{-}1}$ are bounded between 0 and 2, and $\mathbf{X}_d$ has no upper bound for its magnitudes, one advantage of thresholding $\mathbf{P\text{-}1}$ is to prevent the elements of $\mathbf{X}_d$ from having excessive magnitudes, when we estimate $\mathbf{X}_d$ based on $\mathbf{P\text{-}1}$.

To achieve accurate approximations within a few iterations, we initialise $\mathbf{dX}^1$ with the DPCA algorithm using the first two channels, $\mathbf{X}^1$ using the back-projection algorithm on the first channel, and $\mathbf{P}$ with $\mathcal{N}\left(\Phi_B^0(\widetilde{\mathbf{Y}}_3 - \widetilde{\mathbf{Y}}_2) \odot \overline{\Phi_B^0(\widetilde{\mathbf{Y}}_2 - \widetilde{\mathbf{Y}}_1)}\right)$ respectively, where $\mathcal{N}$ is the normalisation operator $(\mathcal{N}(\mathbf{P}) = \mathbf{P} \oslash |\mathbf{P}|)$ to preserve the phases and $\overline{\mathbf{P}}$ indicates the conjugated $\mathbf{P}$. $|^k$ stands for the corresponding variable in the k−th iteration. γ_1, $\mathbf{\Gamma}_2$ and γ_3 are the step sizes in the gradient descent directions. $\mathcal{T}(\mathbf{a}, b)$ is the hard-thresholding operator which sets all the elements in $\mathbf{a}$ below b (in magnitudes) to zeros, and ψ is a threshold value which can be tuned to threshold $\mathbf{X}_d$ for the visualisation purpose. The value of ψ is driven by the level of noise in the data, and in practice it can be 0 or a small value (e.g. $< 0.5\%\|\mathbf{X}_d\|_F$) for subsequent processing.

For the three-channel case, we approximate the step sizes with $\gamma_1 = \|\widetilde{\mathbf{Y}}_1\|_F^2 / \|\Phi_B^0(\widetilde{\mathbf{Y}}_1)\|_F^2$, $\mathbf{\Gamma}_2 = \|\widetilde{\mathbf{Y}}_1\|_F^2 / \|\Phi_B^0(\widetilde{\mathbf{Y}}_1)\|_F^2 \oslash |\mathbf{dX}^1|^2$ and $\gamma_3 = \|\widetilde{\mathbf{Y}}_1\|_F^2 / \|\Phi_B^0(\widetilde{\mathbf{Y}}_1)\|_F^2 / 2$ based on the spectral norm argument given in [120] (the upper bounds of the step sizes are given in [120]). Note that these step sizes play crucial positions in the gradient descent methods. Although these step sizes work well in practice to decrease the objective function, to rigorously guarantee the non-increasing of the cost function, we can employ the following backtracking mechanism at the end of each iteration. Let $f(\mathbf{X}_1, \mathbf{dX}^1, \mathbf{P})$ be the objective function in (4.4). Whenever we find that $f(\mathbf{X}_1|^{k+1}, \mathbf{dX}^1|^{k+1}, \mathbf{P}|^{k+1}) > f(\mathbf{X}_1|^k, \mathbf{dX}^1|^k, \mathbf{P}|^k)$ at the end of each iteration, we restart the k−th iteration with a halved γ_1, $\mathbf{\Gamma}_2$ and γ_3.

Similarly we employ the backtracking mechanism for updating $\mathbf{P}$ because of the complicated constraints on it, i.e. in (4.5) we estimate $\mathbf{P}|^{k+1}$ with the weighted combination of the new estimate and previous estimate $\mathbf{P}|^k$, and $\mathbf{P}|^{k+1}$ is re-estimated with halved λ if $f(\mathbf{X}_1|^{k+1}, \mathbf{dX}^1|^k, \mathbf{P}|^{k+1}) > f(\mathbf{X}_1|^{k+1}, \mathbf{dX}^1|^k, \mathbf{P}|^k)$.

The update equations for $\mathbf{P}$ and $\mathbf{dX}^1$ are defined as followings:

$$\mathbf{P}_{ml}|^{k+1} = \begin{cases} \lambda \times \mathcal{N}(\mathbf{P}_{ml}|^{k+0.5}) + (1 - \lambda) \times \mathbf{P}_{ml}|^k & |\mathcal{N}(\mathbf{P}_{ml}|^{k+0.5}) - \mathbf{1}| > \varphi \\ 1 & \text{otherwise} \end{cases} \quad (4.5)$$

$$\mathbf{dX}_{ml}^1|^{k+1} = \begin{cases} \mathbf{dX}_{ml}^1|^{k+0.5} & \mathbf{P}_{ml}|^{k+1} \neq 1 \\ 0 & \text{otherwise} \end{cases} \quad (4.6)$$

where λ (default value is 1) is used for the backtracking mechanism. φ is an application-based constant for controlling the sparsity of moving targets.

Algorithm 4.2.1: : Iterative algorithm for approximating the solution of (4.4).

1: {Initialisation} $k \leftarrow 1$; $\mathbf{X}_1|^k \leftarrow \gamma_1 \Phi_B^0(\widetilde{\mathbf{Y}}_1)$; $\mathbf{P}|^k \leftarrow \mathcal{N}\left(\Phi_B^0(\widetilde{\mathbf{Y}}_3 - \widetilde{\mathbf{Y}}_2) \odot \overline{\Phi_B^0(\widetilde{\mathbf{Y}}_2 - \widetilde{\mathbf{Y}}_1)}\right)$;

    $\mathbf{dX}^1|^k \leftarrow \gamma_1 \Phi_B^0(\widetilde{\mathbf{Y}}_2 - \widetilde{\mathbf{Y}}_1)$; $\mathbf{X}_d \leftarrow \mathbf{0}$

2: **while** $k < K$ **do**

3:     {Updating $\mathbf{X}_1$} $\mathbf{X}_1|^{k+1} \leftarrow \mathbf{X}_1|^k - \dfrac{\gamma_1}{3} \times$

    $\Phi_B^0\left(\Phi_F^0\left(I \times \mathbf{X}_1|^k + \sum\limits_{i=1}^{I-1}(i \times \mathbf{dX}^1|^k \odot \mathbf{P}^{I-1-i}|^k)\right) - \sum\limits_{i=1}^{I}\widetilde{\mathbf{Y}}_i\right)$

4:     {Updating $\mathbf{P}$} $\mathbf{P}|^{k+0.5} \leftarrow \mathbf{P}|^k - \mathbf{\Gamma}_2 \odot$

    $\sum\limits_{i=3}^{I}\left(\Phi_B^0\left(\Phi_F^0\left(\mathbf{X}_1|^{k+1} + \sum\limits_{j=1}^{i-1}\mathbf{dX}^1|^k \odot \mathbf{P}^{j-1}|^k\right) - \widetilde{\mathbf{Y}}_i\right) \odot \left(\sum\limits_{j=3}^{i}(j-2)\overline{\mathbf{dX}^1|^k} \odot \overline{\mathbf{P}^{j-3}|^k}\right)\right)$

5:     $\mathbf{P}|^{k+1}$ from (4.5)

6:     {Updating $\mathbf{dX}^1$} $\mathbf{dX}^1|^{k+0.5} \leftarrow \mathbf{dX}^1|^k - \gamma_3 \times$

    $\sum\limits_{i=2}^{I}\left(\Phi_B^0\left(\Phi_F^0\left(\mathbf{X}_1|^{k+1} + \sum\limits_{j=1}^{i-1}\mathbf{dX}^1|^k \odot \mathbf{P}^{j-1}|^{k+1}\right) - \widetilde{\mathbf{Y}}_i\right) \odot \left(\sum\limits_{j=2}^{i}\overline{\mathbf{P}^{j-2}|^{k+1}}\right)\right)$

7:     $\mathbf{dX}^1|^{k+1}$ from (4.6)

8:     $k \leftarrow k + 1$

9: **end while**

10: {Output} $\mathbf{P} \leftarrow \mathbf{P}|^K$; $\mathbf{X}_d \leftarrow \mathcal{T}\left(\mathbf{dX}^1|^K \oslash (\mathbf{P} - \mathbf{1}), \psi\right)$ on $\text{supp}(\mathbf{dX}^1|^K)$; $\mathbf{X}_s \leftarrow \mathbf{X}_1|^K - \mathbf{X}_d$

Furthermore, by comparing (4.2) to the EDPCA (2.80), we can summarise the key features (similarities and differences) of them as follows. Firstly, both approaches require the suppression of clutter. While the proposed method is cancelling the clutter with the channel balancing and decomposition model, the EDPCA is cancelling the clutter via the inverse of the clutter-plus-noise covariance matrix. Secondly, both methods are coherently processing the multi-channel data. While the proposed framework encodes the channel differences in the phase correction matrix $\mathbf{P}$, the EDPCA algorithm is compensating the channel differences via the steering vector $\mathbf{P}_{vec}^H(\vartheta_t)$. Thirdly, both models attempt to maximise the target responses. While the proposed framework is estimating the motion parameters by exploiting the target sparsities, the EDPCA algorithm is realising the estimations via the SAR compression with different target states ϑ_t. Finally, both methods are implementing the target indication in the image domain. It can be seen from these features that, various SAR/GMTI algorithms are essentially utilising the similar information and employing similar procedures though they are modelling the GMTI tasks in different ways. The proposed framework is different from others with the exploitation of sparsity and optimisations.

4.3 Required Number of Channels

It is worth mentioning that at least three channels are required to complete the task of decoupling the moving targets and the background. With less channels the feasible set (assuming exact data fidelity) would be the whole space and therefore there would not be enough constraints to identify the sparse moving targets. Consider a simple three-channel SAR system with a single moving target at position (m, l), we denote $\mathbf{X}_i$ $(i = \{1, 2, 3\})$ as the reconstructed reflectivities for the $i-$th channel. Therefore we have the equations:

$$
\begin{aligned}
\mathbf{X}_1(m, l) &= \mathbf{X}_s(m, l) + r \\
\mathbf{X}_2(m, l) &= \mathbf{X}_s(m, l) + rq \\
\mathbf{X}_3(m, l) &= \mathbf{X}_s(m, l) + rq^2
\end{aligned}
\tag{4.7}
$$

where $r \in \mathbb{C}$ is the reflectivity of the target, and $q \in \mathbb{C}$ is the phase correction of the target between channels which lies on the unit ball.

Based on the observations $\mathbf{X}_i$, (4.7) would be enough to retrieve the three unknowns $\mathbf{X}_s(m, l)$, r and q. However, if we are given only the first two channels (the first two equations in (4.7)), we can still estimate r and q as long as $r \gg \mathbf{X}_s(m, l)$ (this is essentially the ATI assumption) via:

$$
\begin{aligned}
r &= \mathbf{X}_1(m, l) \\
\mathbf{X}_s(m, l) &= 0 \\
q &= \mathbf{X}_2(m, l)/\mathbf{X}_1(m, l)
\end{aligned}
\tag{4.8}
$$

However, when $\mathbf{X}_s(m, l)$ is not negligible, (4.8) is inaccurate and we have ambiguities in estimating $\mathbf{X}_s(m, l)$, r and q. Therefore q and the radial velocity of the target can not be accurately estimated when the target is mixed with significant clutter energy. These scenarios are common especially in urban environments.

4.4 Experimental Results

4.4.1 Experiments using Simulations

In this section we first consider a simulated scenario to demonstrate the effectiveness of the proposed model. Within standard Cartesian coordinates, the platform carries a three-channel SAR system in spotlight mode, and the first antenna (fore-antenna) linearly moves from (7000, -25, 7000) m to (7000, 25, 7000) m with velocity $v_p = 200$ m/s. The channels are evenly spaced on the platform track with 0.1 m. The pulse repetition frequency (PRF) is 2000 Hz, the central frequency of the transmitted signal is 10 GHz to simulate an X-band Radar, and the range frequency step size is 800 kHz. The monitored region consists of two moving targets which move from (0, 0, 0) m with (2, 26, 0) m/s and from (-50, 50, 0) m with (-3, -16 , 0) m/s respectively. The key system parameters are summarised in Table 4.1.
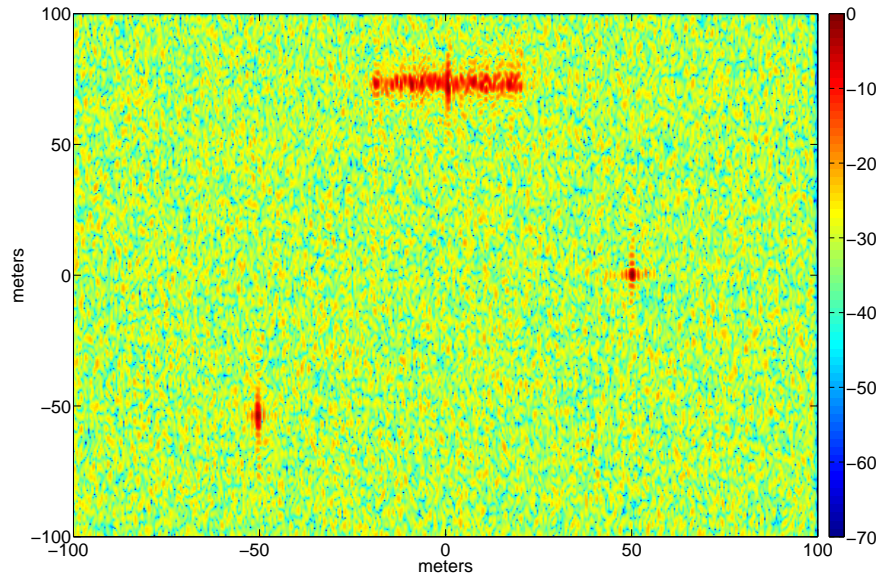
Figure 4.2: The formed image in dB based on the first channel data with the fast back-projection algorithm. The horizontal and vertical axes correspond to range and cross-range directions respectively.

We have obtained the phase histories as 313×500 matrices, and the discrete grid to be considered here is 512×512 which corresponds to -100 m$\sim$100 m in x direction and -100 m$\sim$100 m in y direction. Static targets are distributed on this grid and one stronger static target is located at (50, 0, 0) m. ATI is well known to be hampered by the scenarios where moving targets and clutter are mixed together. Relatively stronger amplitudes and random phases are given to the static clutter

in a rectangular region on purpose to be mixed with one moving target in the image domain and test the performance of the decomposition. Also we add Gaussian random noises (approximately 13 dB SNR) to the raw data. Thus this simulated scenario forms a typical challenging GMTI task which can be visualised in Fig. 4.2. It can be seen that the moving target at (0, 0, 0) m is shifted to the top and mixed with the rectangle, the other moving target at (-50, 50, 0) m is shifted to the bottom, and both of them are defocused along the azimuth direction.

Table 4.1: The system parameters of the simulated scenario

platform start point (m)	(7000, -25, 7000)
platform end point (m)	(7000, 25, 7000)
platform velocity (m/s)	200
channel number	3
channel space (m)	0.1
PRF (Hz)	2000
central frequency (Hz)	10G
range frequency resolution (Hz)	800k
1st moving target start point (m)	(0, 0, 0)
1st moving target velocity (m/s)	(2, 26, 0)
2nd moving target start point (m)	(-50, 50, 0)
2nd moving target velocity (m/s)	(-3, -16 , 0)
phase history size	(313, 500)
SAR image size	(512, 512)
Observed range in x direction (m)	(-100, 100)
Observed range in y direction (m)	(-100, 100)
static target location (m)	(50, 0, 0)
SNR of raw data (dB)	13

We first calibrate the raw phase histories with multiplications in the Fourier domain to realise the delay in time domain. Then the three balanced data sets $\widetilde{\mathbf{Y}}_1$, $\widetilde{\mathbf{Y}}_2$ and $\widetilde{\mathbf{Y}}_3$ are processed with the presented moving targets and background decomposition model. Since SAR applications are essentially high volume data processings, as shown in Algorithm 4.2.1, we start with the presented initialisation to retrieve acceptable results within few iterations, and set φ to 0.005.

The comparisons of the decompositions with different iteration numbers (1, 2, 5, 10) are shown in Figure. 4.3. It can be seen that with proper initialisations we can have the acceptable decomposition performance within few iterations. With iterations, the two moving targets are significantly better removed from the background images and the static target is significantly better
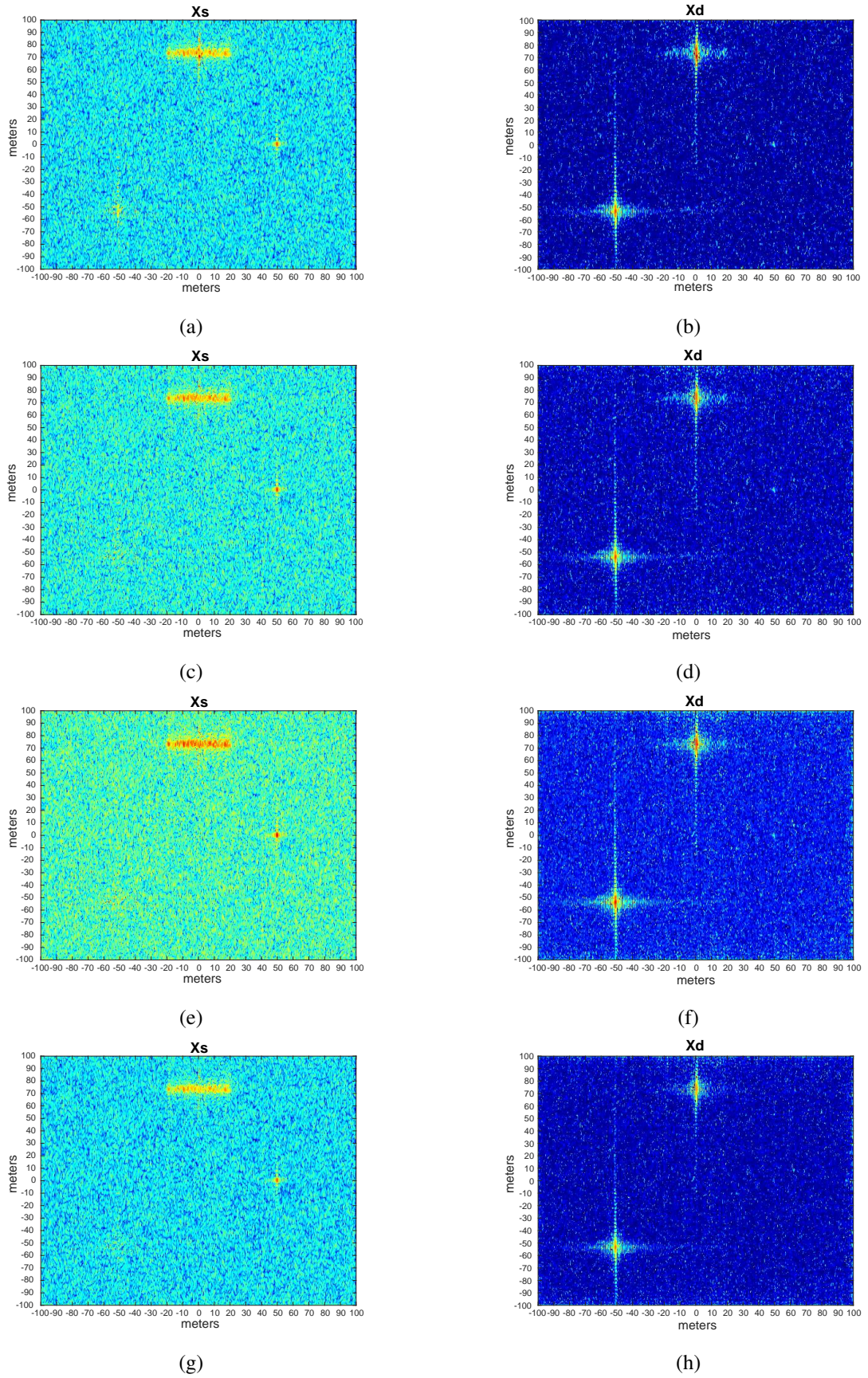
Figure 4.3: The decoupled SAR images displayed in dB using the proposed approach. a) c) e) g) The background images with 1, 2, 5 and 10 iterations respectively. b) d) f) h) The SAR images of the moving objects with 1, 2, 5 and 10 iterations respectively.

84

removed from the images of moving targets. Here the rectangle is well separated from the moving target with 10 iterations. With conventional methods the whole support of the moving targets is cropped, and the amplitudes and phases will not be accurately estimated.
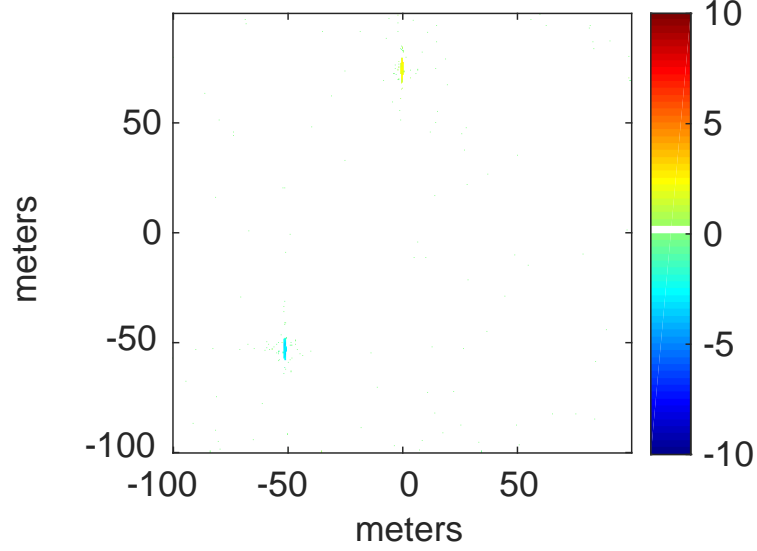
Figure 4.4: The estimated velocity map in x direction which correspond to the estimated $\mathbf{P}$ after 10 iterations with proper initialisations.

The estimated phase correction matrix $\mathbf{P}$ is transferred to the velocities in x direction via $\mathbf{v}_x = \sqrt{2}(c/(4\pi))\angle\mathbf{P}(v_p/(f_0 d))$, where $\angle$ is an operator to extract the phases, and the estimated $\mathbf{v}_x$ is shown in Figure. 4.4 (only valid on the support of the two moving targets). We take the local mean values of $\mathbf{v}_x$ as the estimations for the target velocities and get -2.94 m/s and 2.06 m/s which are close to the ground truths. Here the standard ATI on the first two channels, i.e. $\angle\mathbf{P} = -\angle(\Phi_B^0(\widetilde{\mathbf{Y}}_1) \odot (\Phi_B^0(\widetilde{\mathbf{Y}}_2))^*)$, gives the velocity estimations as -2.87 m/s and 1.5 m/s (local mean values). The ATI results remain consistent for the -3 m/s target but have significant deviations for the target which is mixed with the rectangular clutter.

4.4.2 Experiments using Real Data

In this section, the proposed decomposition framework as described in Algorithm 4.2.1 is implemented to decouple the moving targets and background for the AFRL GOTCHA GMTI challenge. As discussed in Chapter 2, we need to calibrate the ground truth velocities of the moving target for this dataset. Based on the positions of the target in the ground truth, we differentiate its corresponding coordinates to estimate its velocities in the z direction $v^{(z)}$.

Specifically, with the DEM we estimate $v^{(z)}$ based on the differences in z direction and smooth the velocity vector with a five tap moving average filter. The radial velocities of the moving target are are shown in Fig. 4.5. Particularly the blue line indicates the given velocity elements, the red line is estimated completely based on the differentiation of the positions, and the green line is approximated with the given xy velocity components and GPS-based z velocity. We take the green line as the baseline of the radial velocities in the experiments.
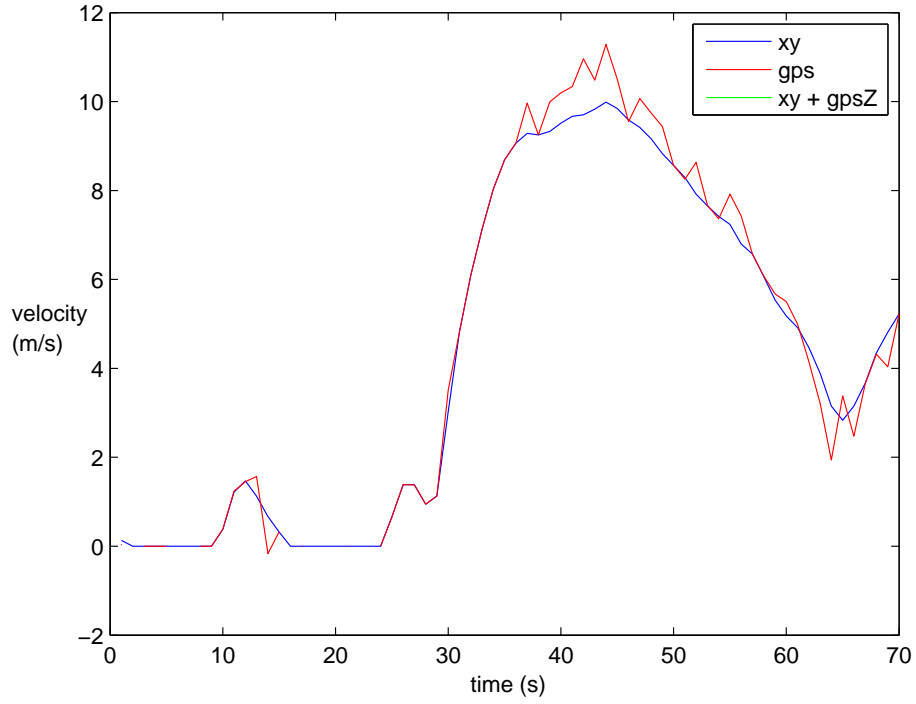
Figure 4.5: The comparison of the estimated radial velocities (m/s) of the target with time based on blue (the given velocity in xy), red (the differences of the GPS) and green (the given velocity in xy and differences of the gps in z direction).

We then directly estimate the radial velocities from $\mathbf{P}$ for all image pixels within nine sub-apertures (centered at the $25-$th, $30-$th, $35-$th, $40-$th, $45-$th, $50-$th, $55-$th, $60-$th and $65-$th second respectively). As we have estimated the velocity map for the whole image, the estimated velocities can vary from pixel to pixel and the accuracies of relocations are very sensitive to the estimated radial velocities. In this section we focus on the moving target for which we have the ground truth with a 15-by-15 window centered on the target in $\mathbf{X}_d$, and extract its phase history with $\mathbf{Y}_{d1} = \Phi_F^0(\mathbf{X}_{d1})$. To have a single velocity estimation $v^{(r)}$ for this target, we need to integrate these pixel-wise velocities. By assuming that the pixels with large magnitudes in $\mathbf{X}_{d1}$ are likely to be the targets, we employ the weighted average within the window to estimate a single radial velocity, using weights proportional to the pixel magnitudes. The pixels which have significant

deviations (larger than 2 m/s) from the estimated velocities are removed.

(a)
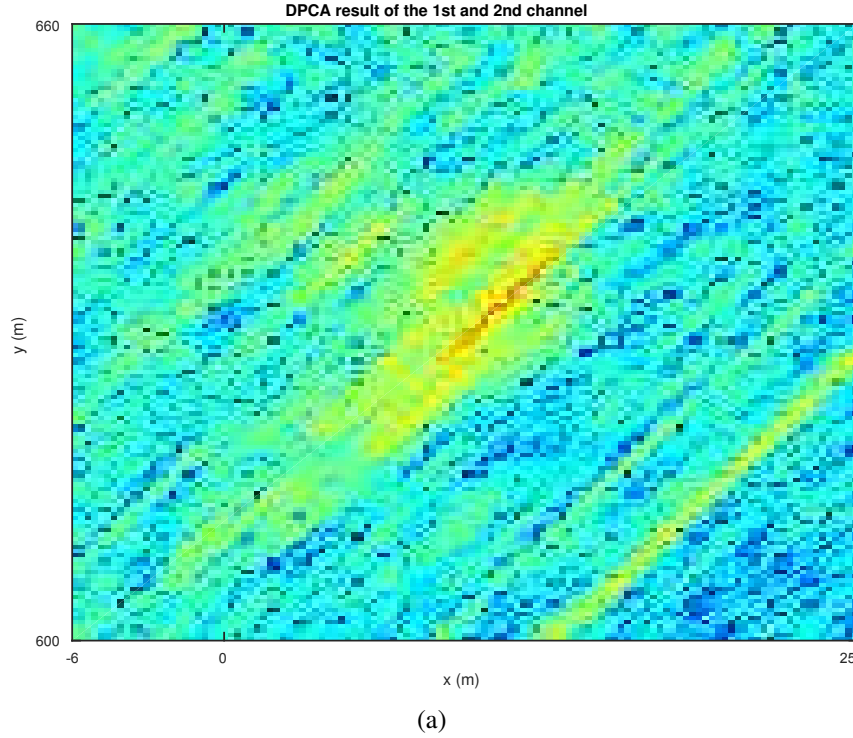
Figure 4.6: The DPCA image between the 1-st and 2-nd channel centered at the target.

With the estimated $v^{(r)}$, we apply the moving target imaging approach (3.22) to $\mathbf{Y}_{d1}$ to localise the relocated target. A hybrid DPCA/ATI method (using pair-wise DPCA and passing the results to ATI) is used as the baseline which was shown to outperform the pure ATI and DPCA [92]. (Note that, for a fair comparison, we employed the fast imaging operators [1] instead of the Doppler processing described in [92].)

A typical decomposition at the $50-$th second is shown in Fig. 4.6 and 4.7. It can be seen that the proposed method decoupled the main energy of the target and the background (here the ψ in Algorithm 4.2.1 is $0.35\%\|\mathbf{X}_d\|_F$ to threshold $\mathbf{X}_d$ for visualisation purpose). Note that we consistently set $\varphi = 0.5$ to control the sparsity of moving targets in Algorithm 4.2.1, regardless of the sparsity of the scenarios among different snapshots, and this threshold controls how we retrieve the support of $\mathbf{X}_d$ which leads to the balance of the energy allocation between $\mathbf{X}_s$ and $\mathbf{X}_d$. Practically φ can be lowered to achieve a better decomposition for this sub-aperture.

In Fig. 4.8 we show how the cost function varies with iterations in the processing of this snapshot, demonstrating the non-increasing property. It is worth mentioning that empirically in all our experiments the Algorithm 4.2.1 works without triggering the backtracking mechanism in our experiments.

(a)

(b)

Figure 4.7: a) The background image centered at the target. b) The SAR image of the moving target.

Figure 4.8: The objective function of (4.4) with iterations.

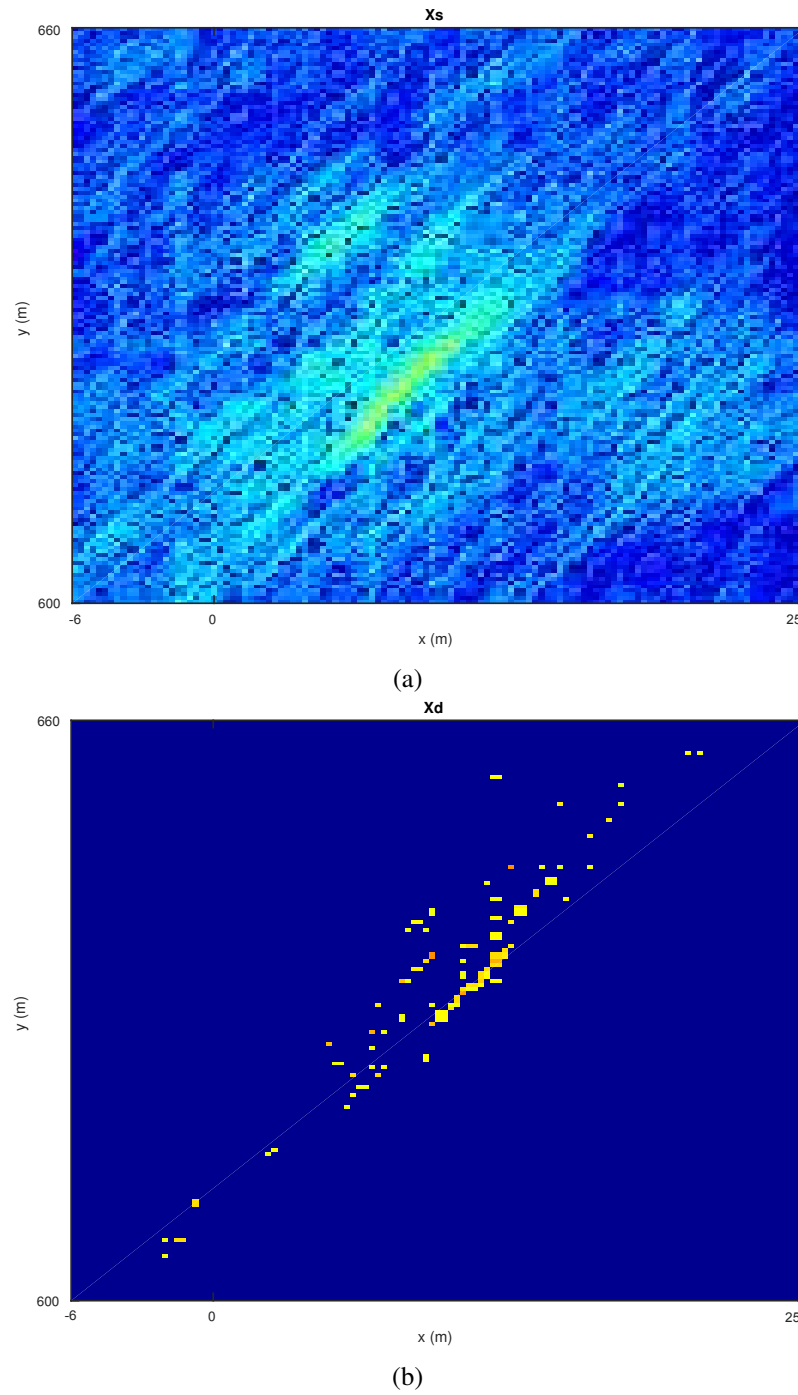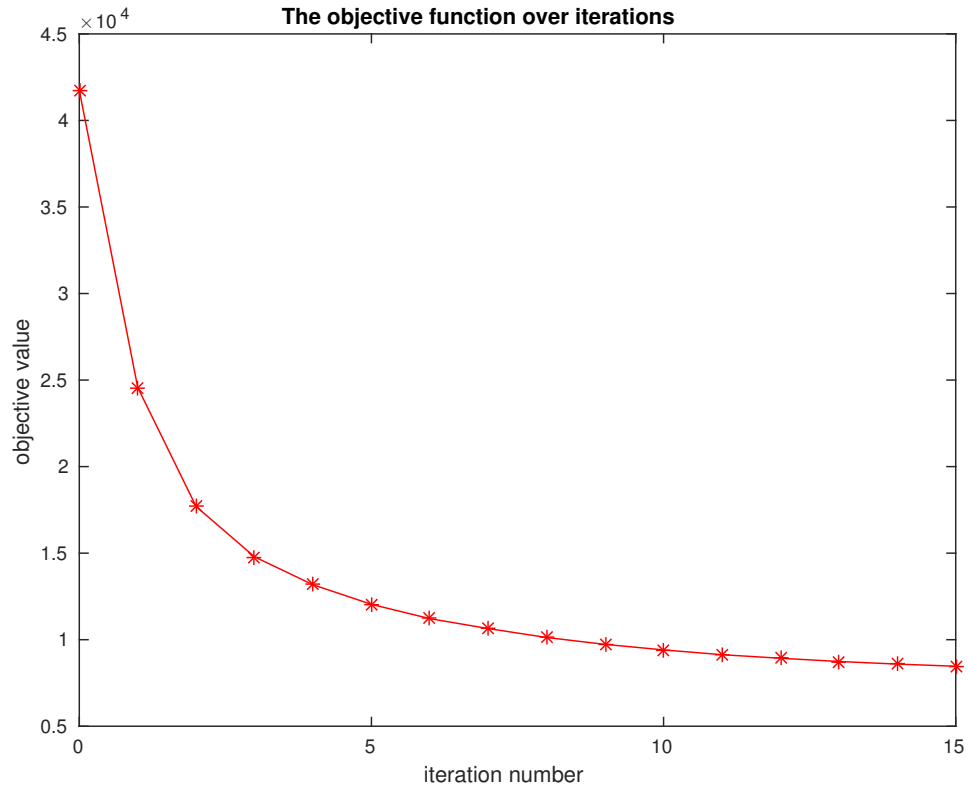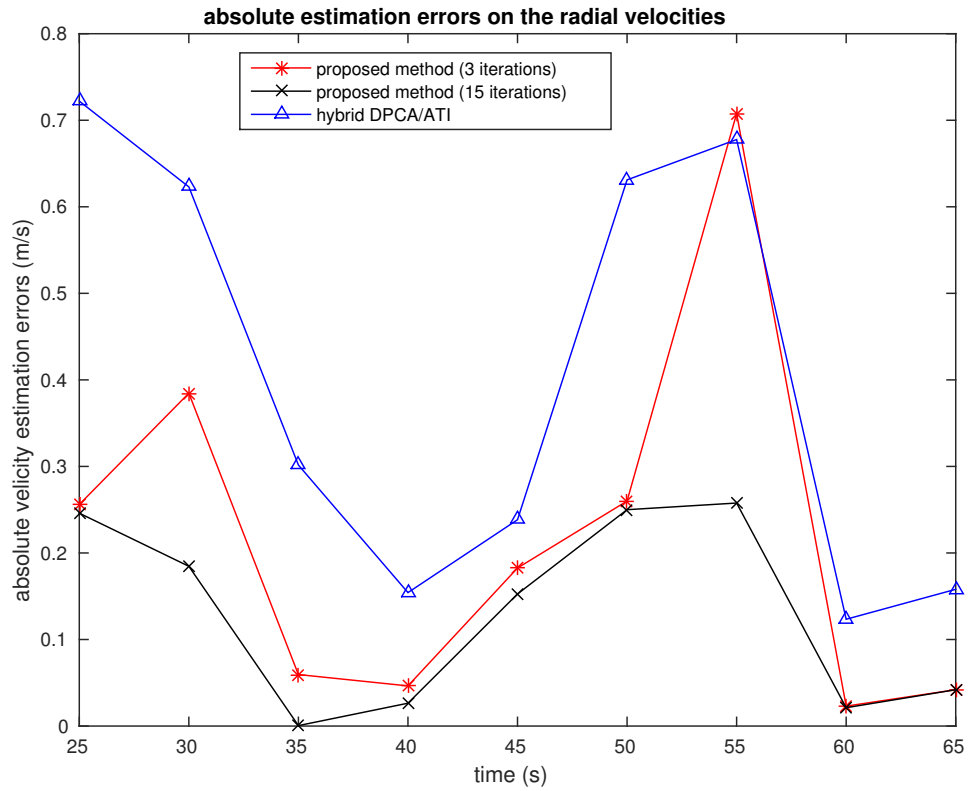Figure 4.9: The comparisons of the absolute estimation error (based on the ground truth) on the target radial velocity with the proposed approach and hybrid DPCA/ATI.

We processed the nine sub-apertures, and compared the estimated radial velocities to the ground truth in Fig. 4.9. Here we employed 3 and 15 iterations in Algorithm 4.2.1 respectively to compare the performance. Each sub-aperture contains 400 azimuth samples (roughly 0.18 seconds). In Fig. 4.9 the proposed method has better accuracy in estimating radial velocities compared to the hybrid DPCA/ATI. With 15 iterations we received a smaller error on the radial velocity estimation. The proposed decomposition method gives better performance on the target/clutter decomposition with more iterations.

Note that at the $55-$th second, the scenario is challenging for conventional SAR-based GMTI techniques. Firstly, this sub-aperture corresponds to the moment that the target is mixed with a strong static clutter (buildings). It significantly hampered the correct estimation. Secondly, at this moment the vehicle is moving away from the antenna with 6.84 m/s. As the pixel-wise radial velocities are estimated based on the phase of $\mathbf{P}$, the phase wrapping leads to an estimation cycle on the radial velocities (the cycle is 6.6 m/s for this sub-aperture). The ground truth is very close to the cycle value which means that it is easily confused with zero velocities and the thresholding operations in (4.5) is likely to threshold certain components of the target which increases the estimation errors.

4.5   Summary

In this chapter we consider the typical SAR-based GMTI challenge with a multi-channel SAR system. We first introduce the conventional GMTI methods DPCA and ATI. A state-of-the-art method hybrid DPCA/ATI is also presented to be the baseline for comparison in this thesis. We further discuss about how we are inspired by the DPCA/ATI and sparsity to design the SAR/GMTI framework. We have proposed a novel sparsity-aided framework to decompose SAR data into dynamic and static portions which correspond to the moving targets and clutter/background respectively. This model is sufficiently versatile to incorporate the DEM information. We give out the details of the proposed framework and a practical implementation of the model in this chapter. The limitations of this model are analysed, and the effectiveness of the proposed model is demonstrated through both simulations and real data (AFRL GOTCHA challenge dataset). We have shown decent background/targets decompositions and accurate radial velocity estimations in the experiments.

<div align="right">5</div>

Moving Target Imaging and State Estimation

5.1 Introduction

With the aforementioned GMTI methods, there still exist a number of problems in the practical SAR/GMTI processing. First of all, some GMTI approaches such as the conventional DPCA and ATI algorithms are not developed to realise the full target state estimation though the radial velocities can be estimated via ATI. Secondly, some methods focus on a specific problem in the SAR/GMTI application with specific assumptions and thus do not tackle all GMTI tasks. Furthermore, typical SAR-based GMTI applications often require to process large volume of data, and they are significantly hampered by the high computational load. While the DPCA and ATI algorithms can be implemented with efficient computations, other statistical test algorithms which calculate weights for each cell and parameter combination are still too computational intensive. Lastly, the recent sparsity-aided GMTI investigations such as [94] [108] focus on the narrow aspects in SAR/GMTI which are not comparable to the conventional whole SAR/GMTI processing chain. Also some latest sparsity driven methods such as [106] encounter difficulties in practical implementations (e.g. can be over-complicated and dealing with simplified scenarios), and they are currently limited to simulations.

By investigating the sparsity driven SAR/GMTI framework in this thesis, we have made attempts to resolve some key problems of the existing methods aforementioned. Following the developed SAR/GMTI models in the Chapter 4, in this chapter, we first analyse the role of DEM in target state estimation. Next, by exploiting the target sparsities, we introduce the sparsity-aided moving target imaging and target state estimation. We implement this algorithm as the final stage of the complete pipeline to benefit from the extracted moving targets using the previous stage and thus significantly decrease the complexity of the target state estimation model. This processing mechanism to estimate target states within a separated stage can thus be directly compared with conventional SAR/GMTI target state estimation algorithms. As it is not straightforward to simulate an elevation map, we directly demonstrate the effectiveness of the DEM-aided target

state estimation approach through real data. The proposed sparsity-aided target state estimation and imaging methods are demonstrated via both simulations and the AFRL GOTCHA SAR/GMTI challenge dataset.

5.2 DEM-aided Target State Estimation

In this section we focus on the role of DEM in moving target state estimation. We will introduce the sparsity-aided target state estimation in the next section. There has been a number of investigations in estimating the states of moving target. For example, it is well known that the radial velocities of moving targets correspond to the phase differences between SAR images from different channels in ATI [121] [122], and the azimuth velocities can be estimated through a bank of filters [123]. It was suggested in [124] that the azimuth velocities of moving targets can be analysed with a Fractional Fourier transform in the time-frequency domain. In [10] it was reported that the estimated velocities can be selected by best focusing the targets to give sharp image patterns and also maintaining the data fidelity.

The utilisation of DEM also give us a direct estimation on the $v_t^{(z)}$ in $\mathbf{v}_t$ by differentiating the elevations, which provides us a further constraint on the velocity estimations. It can also be used as an auxiliary criterion to help calibrate the velocities estimated by other methods. The targets are assumed to follow the surface of the DEM and its trajectory is constrained to a 2D surface in 3D space. In particular, for far-field observation, the target velocity components obey the geometrical restriction Υ which can be defined as:

$$v^{(r)} \approx -\langle v^{(x)}, \frac{\mathbf{r}_1^{(o)}}{r_1^{(o)}}\rangle - \langle v^{(y)}, \frac{\mathbf{r}_1^{(o)}}{r_1^{(o)}}\rangle - \langle v^{(z)}, \frac{\mathbf{r}_1^{(o)}}{r_1^{(o)}}\rangle \tag{5.1}$$

where negative $v^{(r)}$ means that the target is moving away from the platform. As $v^{(z)}$ is in general not too large in most scenarios, with not too large sub-apertures (i.e. not too large observation duration), we can approximate it by differentiating the coordinates of the relocated target at different frames.

Given the estimated $v^{(r)}$ and (5.1), $v^{(x)}$ is a function of $v^{(y)}$. This spatial constraint can thus be described via:

$$\mathbf{v}_t = \Upsilon(v^{(z)}, v^{(r)}) \tag{5.2}$$

$$= \left(\left(-v^{(r)} - \langle v^{(y)}, \frac{\mathbf{r}_1^{(o)}}{r_1^{(o)}} \rangle - \langle v^{(z)}, \frac{\mathbf{r}_1^{(o)}}{r_1^{(o)}} \rangle \right) / \langle \frac{\mathbf{v}^{(x)}}{v^{(x)}}, \frac{\mathbf{r}_1^{(o)}}{r_1^{(o)}} \rangle, v^{(y)}, v^{(z)} \right) \qquad (5.3)$$

where Υ represents the geometrical constraint operator defined by the DEM and platform positions.

In addition, when the targets are moving on roads in urban environments, the geometrical information of the road could be used in combination with the DEM to estimate the target states in three directions $(v_t^{(x)}, v_t^{(y)}, v_t^{(z)})$. The effects of DEM in the estimation of moving target states are demonstrated through the section of experimental results.

5.3 Sparsity-aided Target State Estimation and Imaging with DEM

In this section, we introduce the sparsity driven target state estimation and imaging algorithm within the proposed SAR/GMTI framework in details. By comparing to the method in Section 5.3.1, the proposed algorithm is utilising the sparsity from a different way. Specifically, we will show that, the method in Section 5.3.1 is considering a pixel-wise sparse approximation problem, and the proposed framework is considering the local imaging around a target, and we are processing one moving target at a time. While the method in Section 5.3.1 is exploiting the sparsity in radial velocity components, and the proposed algorithm is exploiting the sparsity in the SAR images of moving targets. Furthermore, we have separated out the zero velocity component from the dynamic part and hence it is reasonable to assume that in each cell there is likely to be only a single target.

The task of estimating the target states requires us to consider the problem in a higher dimensional parameter space instead of the conventional physical coordinates space (x-y-z space). Therefore, by combining the full velocity map of the whole observed scene $\mathbf{V}$ with the physical space, we can generate an extended SAR processing space, and estimate the target states (positions, velocities, etc.) that correspond to the sparsest configuration in the space. As illustrated in Fig. 5.1, the moving target imaging task is equivalent to a search problem in a higher dimensional space. We are able to solve this since the at the correct velocity the target should be better focused, and therefore sparser in the extended space.

Based on this motivation, the moving target state estimation can be naturally realised within the proposed sparsity-regularised SAR/GMTI framework. As explained in Chapter 4, the more complete framework of the sparsity regularised model (4.2) can be derived to simultaneously
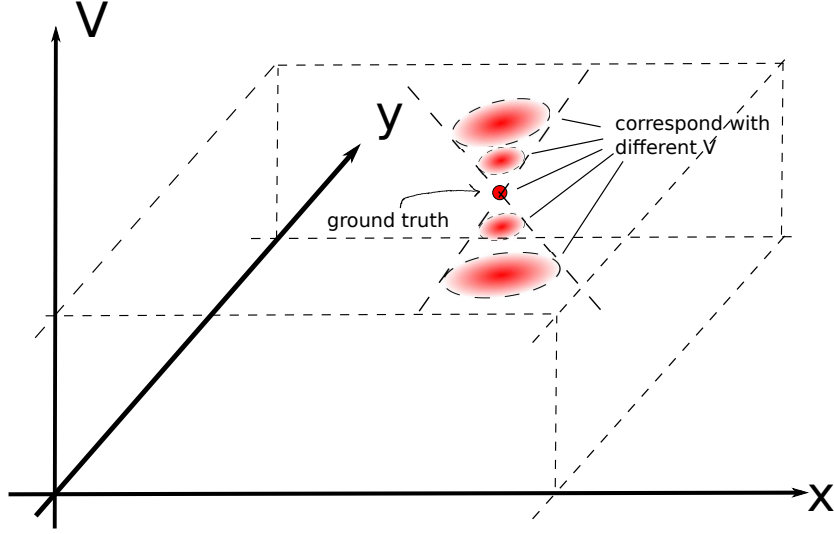
Figure 5.1: The high dimensional space for the moving target imaging and estimation. The target states correspond with the sparsified image of this target.

realise all SAR/GMTI tasks including SAR imaging, target detection, target state estimation, and moving target imaging with relocation and refocusing:

$$\min_{\mathbf{X}_s, \mathbf{X}_d, \mathbf{P}, \mathbf{V}} \quad \frac{1}{2} \sum_i \|\widetilde{\mathbf{Y}}_i - \Phi_F^{\mathbf{V}}(\mathbf{X}_s + \mathbf{X}_d \odot \mathbf{P}^{i-1})\|_F^2$$

$$s.t. \quad \|\mathbf{X}_d\|_0 \leq s$$

$$\mathrm{supp}(\mathbf{X}_d) = \mathrm{supp}(\mathbf{P}\text{-}\mathbf{1}) \tag{5.4}$$

$$\mathbf{P} = \exp\left(-j\frac{4\pi}{c}f_0\mathbf{V}^{(r)}\frac{d}{v_p}\right)$$

$$\mathbf{V} = \Upsilon(\mathbf{V}^{(z)}, \mathbf{V}^{(r)})$$

where $\Phi_F^{\mathbf{V}}$ denotes the DEM-aided forward-projection operator with the full velocity map, the constraint on $\mathbf{P}$ is an element-by-element function, and Υ is the geometrical restriction that constrains the velocity components in different directions (5.3).

However, it can be seen from (5.4) that the model corresponds to a very large search space with a complex and non-separable constraint set. It is very challenging to directly solve this problem with such a large feasible set and multiple variables. Furthermore, as explained in Chapter 3 and 4, the target locations (the support of $\mathbf{X}_d$) change as a function of the target velocities and we do not have the efficient implementation for the projection operator $\Phi_F^{\mathbf{V}}$ with full velocity map $\mathbf{V}$. As the compromise, we are able to present the efficient projection operator for one moving target with its velocity vector $\mathbf{v}_t$ (3.21) which is also consistent with the efficient algorithm in [1]. Considering these difficulties in the practical implementation, we thus break this complete model

(5.4) into a two stage process where we first resolve (4.2) without the full target velocities (as described in Chapter 4) and then focus on the target state estimation.

Given the estimated reflectivities of the decoupled moving targets $\mathbf{X}_d$, we now extend the analysis to selected targets in order to estimate their full states and enhance the target image formation with relocation and refocusing. Here we consider the integration of target velocities and the DEM into the SAR imaging of the moving target. The SAR image formation with the DEM can be realised via (3.20). Let us focus on a single moving target of interest and use a local rectangular window to capture its reflectivities $\mathbf{X}_{d1}$. We denote the target velocity vector as $\mathbf{v}_t = (v^{(x)}, v^{(y)}, v^{(z)})$ and the measurements associated solely with the imaging contribution of the target as $\mathbf{Y}_{d1} = \Phi_F^0(\mathbf{X}_{d1})$. The image formation of this moving target with the DEM and known velocities can be formulated as (3.21).

In this work the moving target imaging is realised with (3.21) and (3.22). It can be seen that the target velocity can be naturally embedded in the fast SAR imaging mechanism [1] by fixing the range histories with pre-calculated constant vectors. Therefore, the velocity estimation problem can be tackled by utilising the efficient projection operators and target sparsities:

$$
\begin{aligned}
\mathbf{v}_t &= \underset{\mathbf{v}^\dagger}{\operatorname{argmin}} \, \|\Theta^{\mathbf{v}^\dagger}(\mathbf{Y}_{d1})\|_1 \\
s.t. \quad \mathbf{v}^\dagger &= \Upsilon(\mathbf{v}^{(z)}, \mathbf{v}^{(r)}) \\
\operatorname{supp}(\Theta^{\mathbf{v}^\dagger}(\mathbf{Y}_{d1})) &= \kappa
\end{aligned}
\tag{5.5}
$$

where $\Theta^{\mathbf{v}^\dagger}$ is the approximated velocity compensated backward operator for the moving target, κ is the support set (a 10-by-10 window in this work) of the relocated target centered at the stongest pixel, and the target velocity obeys the geometrical constraint, $\mathbf{v}^\dagger = \Upsilon(\mathbf{v}^{(z)}, \mathbf{v}^{(r)})$, which represents the spatial constraint defined by the DEM and platform positions. $\mathbf{v}^{(r)}$ can be estimated directly from $\mathbf{P}$, and $\mathbf{v}^{(z)}$ can be estimated by differentiating the DEM based on target positions between neighbouring sub-apertures.

It can be seen from (5.5) that we are considering locally in a neighbourhood of the target position and the goal is to adapt the velocity components to refine the image. Given the estimated $\mathbf{v}^{(r)}$ and $\mathbf{v}^{(z)}$, we can have $\mathbf{v}^{(x)}$ as a function of $\mathbf{v}^{(y)}$ and this optimisation problem becomes a simple one dimensional line search problem. Thus we are essentially employing the exhaustive search for $\mathbf{v}^\dagger$. Here $\Theta^{\mathbf{v}^\dagger}$ is calculated with the LSQR algorithm [125] to approximate the pseudo-inverse of the velocity compensated forward operator. In particular the LSQR algorithm is

employing the developed fast projection operators with iterations to improve the data fidelity. We form the moving target image $\Theta^{\mathbf{v}^\dagger}(\mathbf{Y}_{d1})$ for each target velocity vector $\mathbf{v}^\dagger$ as measured in (5.5), and then select the $\mathbf{v}^\dagger$ through the $L1$ pseudo-norm on the reconstructed image. Note that the DEM may have limited accuracy, but the estimated $\mathbf{v}^{(z)}$ can still be used as an auxiliary parameter in (5.5). Finally $\Theta^{\mathbf{v}^\dagger}(\mathbf{Y}_{d1})$ is the formed SAR image of the moving target with relocation and refocusing.

5.4 Experimental Results

5.4.1 Experiments using Simulations

In this section we first consider the simulated scenario as presented in Chapter 4. By retrieving the states of the two moving targets and forming their SAR images, the aim is to demonstrate the effectiveness of the sparsity-aided target state estimation through this simulated scenario. Note that we choose the 10-iteration results from the previous processing stage to estimate the background image $\mathbf{X}_s$, dynamic image $\mathbf{X}_d$ and the phase correction matrix $\mathbf{P}$. The estimated velocities in x direction for the two targets are 2.06 m/s and -2.94 m/s respectively as described in Chapter 4. The reflectivities of the two moving targets are then extracted by focusing the detected moving targets with 30-by-30 rectangular windows, and the phase histories of the targets are estimated via $\mathbf{Y}_{d1} = \Phi_F^0(\mathbf{X}_{d1})$. Given that this simulation contains no elevation information ($v^{(z)} == 0$), based on the estimated $\mathbf{v}^{(x)}$ and (5.5), we line search for the velocity in y direction $\mathbf{v}^{(y)}$ with 0.5 m/s searching intervals in this work.

In particular, the target image $\Theta^{\mathbf{v}^\dagger}(\mathbf{Y}_{d1})$ for each $\mathbf{v}^\dagger$ is formed using two iterations of LSQR to obtain a least squared match between $\mathbf{Y}_{d1}$ and the forwarded image. We limit the support of each moving target with a 25-by-25 window centered at the strongest pixel. The velocities are estimated to minimise the objective function of (5.5). For this simulated scenario, we show the results with the proposed approach in Fig. 5.2 and Fig. 5.3. It can be seen from Table 5.1 that the estimated velocities in y direction for the two targets are 27.5 m/s and -15.5 m/s respectively which are very close to the ground truth (26 m/s and -16 m/s). With less clutter mixed with the second target, we achieved relatively better estimation accuracy on this target.

With the estimated target velocities, we now apply the moving target imaging method to the two moving targets. In Fig. 5.4 and 5.5, we compare the original SAR images of the moving targets
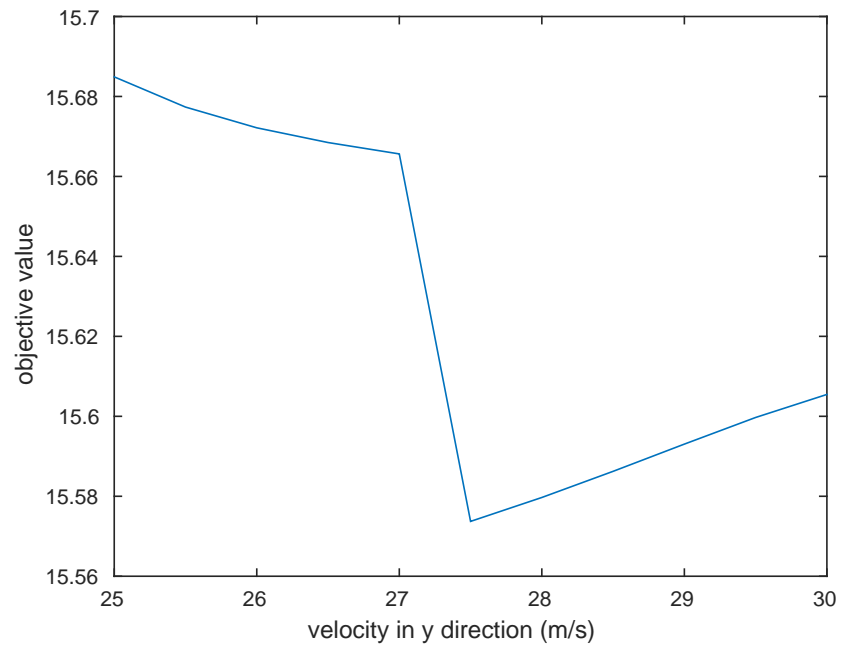
Figure 5.2: Objective values with respect to different $v^{(y)}$ for the 1st target.
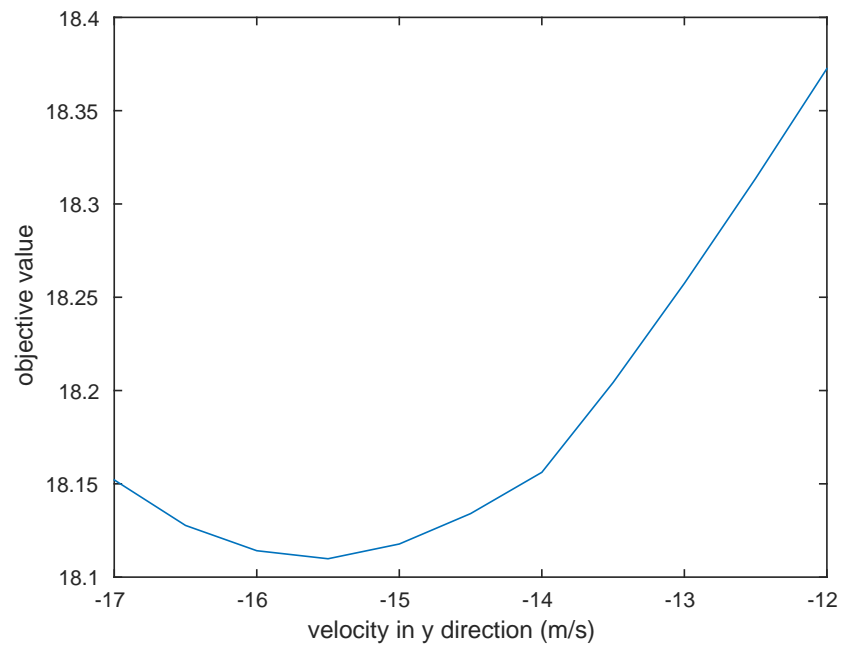

Figure 5.3: Objective values with respect to different $v^{(y)}$ for the 2nd target.

Table 5.1: The estimated velocity components of the simulated scenario

ground truth velocity for the 1st moving target (m/s)	(2, 26, 0)
estimated velocity for the 1st moving target (m/s)	(2.06, 27.5, 0)
ground truth velocity for the 2nd moving target (m/s)	(-3, -16, 0)
estimated velocity for the 2nd moving target (m/s)	(-2.94, -15.5, 0)

to the formed images after employing the proposed state estimation and imaging algorithm. It can be seen from the sidelobes that the formed SAR images of the moving targets have significant visual improvements in terms of both focusing effects and physical locations. The reason that the image formation of the second moving target achieves better performance is very likely to be due to the clutter mixed with the first target.

5.4.2 Experiments using Real Data

In this section, we first employ the approach described in Section 5.4 with the AFRL GOTCHA GMTI challenge dataset to analyse the role of DEM in target state estimation. Next, by utilising the target sparsities, we demonstrate the effectiveness of the sparsity-aided target state estimation within the proposed SAR/GMTI framework through the AFRL GOTCHA GMTI challenge dataset.

DEM-aided Moving Target Analysis

In this subsection, based on the calibrated DEM, we demonstrate the image formation and state estimation of the moving target from the AFRL GOTCHA GMTI challenge dataset with the aforementioned method.

For this dataset, the ground truth GPS data of the target is not aligned with the raw phase histories, and we have to find out a shift value Δ for the raw data to match the GPS of the target. We extract two tracks (pulse number 94001 to 108000 and pulse number 144001 to 148000) among the whole path to realise the calibration. With different shift values, we employ the green line in Fig. 4.5 and relocate the target, and search for the optimal match between the ground truth target path and relocated target path. For example, given that the PRF is 2171.6 Hz and we employ 400 azimuth samples for each sub-aperture, the sub-aperture centred at T_p corresponds to the azimuth time $T_p/2171.6 + \Delta$. For $\Delta = 17$ we first show the moving target relocation results without the DEM using the 46-th second data (0.2 seconds sub-aperture) in Fig. 5.6 where the relocated target
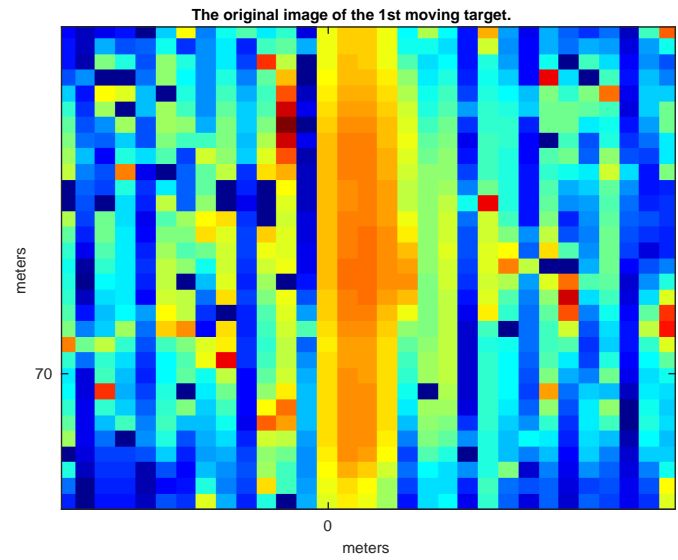
(a)
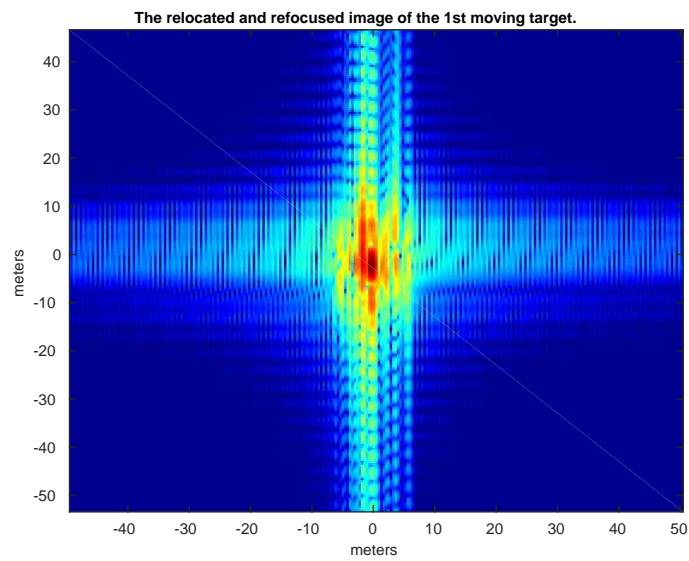
(b)

Figure 5.4: a) The original image of the 1st moving target. b) The relocated and refocused image of the 1st moving target.

The original image of the 2nd moving target.

(a)

The relocated and refocused image of the 2nd moving target.

(b)

Figure 5.5: a) The original image of the 2nd moving target. b) The relocated and refocused image of the 2nd moving target.
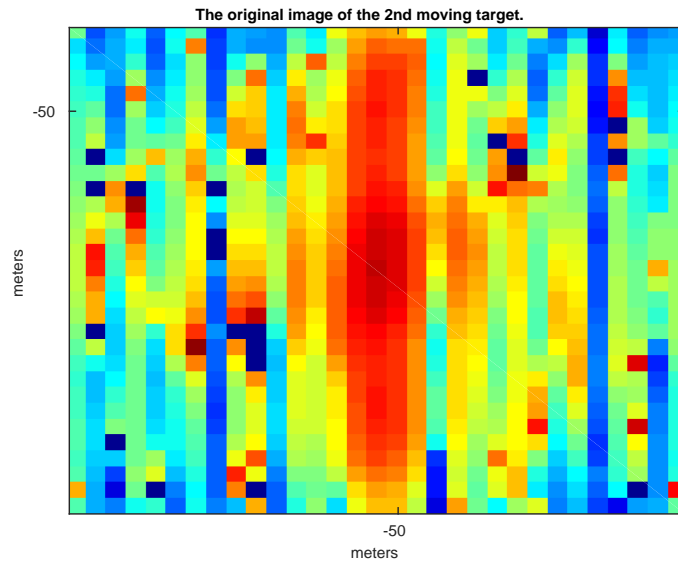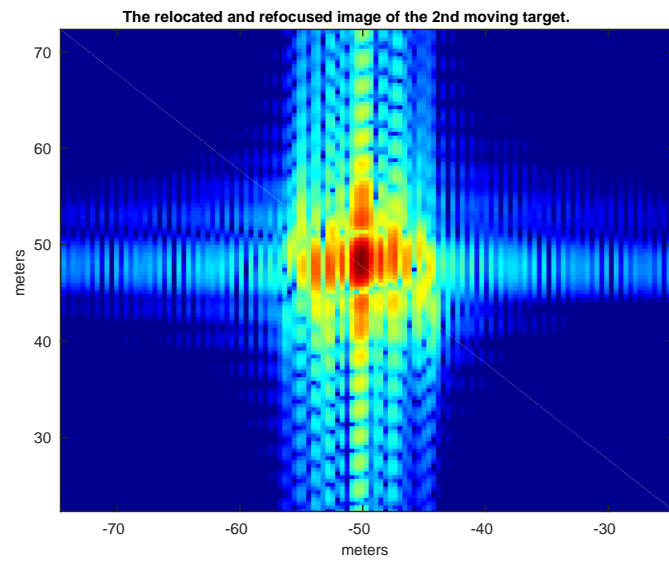
is overlaid to the gray background SAR image.
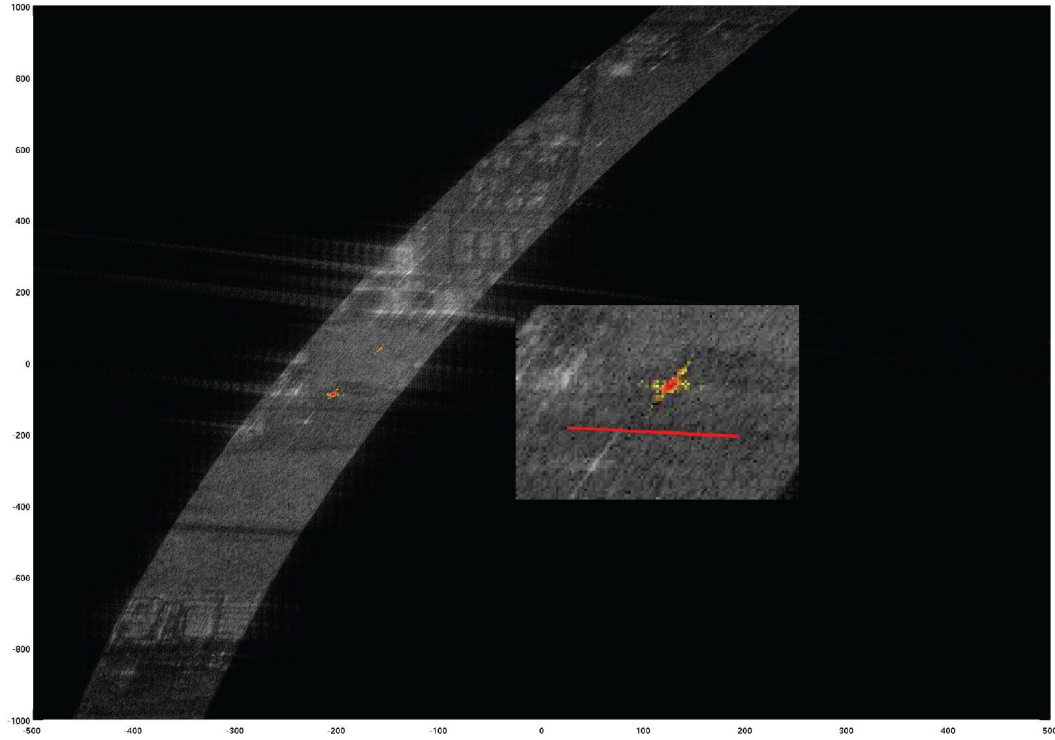
Figure 5.6: Overlaid background (black and white) and relocated moving targets (coloured) without the DEM. Significant deviation of the coloured target from the road can be found in the image.

It can be seen from the zoomed-in image of Fig. 5.6 (the road is coloured) that he estimated target location is not far from the ground truth. However, the moving target should be running on the road below the estimated location. The significant deviation is likely due to the image formation distortions which are caused by the missing of DEM (digital elevation model) information.

We now present the target relocation results with the DEM of the two sub-apertures in Fig. 5.7 (the targets are extracted based on the ground truth). It can be seen that the targets are very well relocated with the extracted DEM.

The DEM can be further exploited in the estimation of moving targets velocities. We take another example to show the DEM-aided moving target state estimation performance. Given the estimated DEM and pre-processed phase histories, we focus on the processing of the GOTCHA data from azimuth number 144001 to 146000. The data is divided into five sub-apertures and each sub-aperture contains 400 azimuth samples.

We employ the presented GMTI technique [6] and estimate the radial velocities of the moving
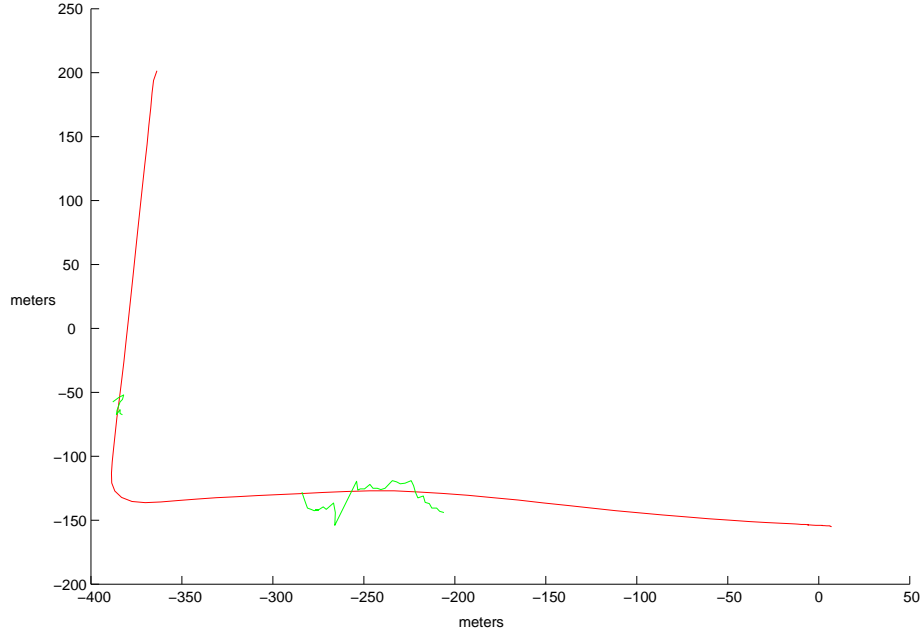
Figure 5.7: The ground truth path of the target is marked in red. The relocated tracks of the two selected sub-apertures are marked in green.

targets for the five sub-apertures. Here other GMTI techniques which are able to give estimations on radial velocities can also be used. Note that our purpose here is to justify the effects of the DEM. As we have estimated the velocity map for the whole image, the estimated velocities can vary from pixel to pixel and the accuracies of relocations are very sensitive to the estimated radial velocities. Instead of giving a single estimation on the radial velocity, we consider a small 30×30 window around the target for which we have the ground truth. In this way we have 900 possible radial velocities of this target.

Since the target is likely to move slowly in the z direction, $v_t^{(z)}$ can be estimated by differentiating the positions of the moving target. It gives us an additional constraint on the velocities to help estimate the full state of the target. Particularly in the urban environment, the moving target is likely to move on the roads. The direction of the road gives us another restriction on the velocity estimates. Furthermore, the velocity estimates can be calibrated by allowing errors in radial velocity estimates, i.e. relocating the moving target to the intersection of the road and its possible locations. Calibrated relocated positions of the target are associated with the calibrated radial velocity estimates which improve the accuracy of the estimated target radial velocity. We could also include other priors such as the inability for a vehicle to suddenly change direction or velocity.

In this experiment, suppose that the target is moving on the road, we first select the radial velocity estimate within the 30×30 window (empirical window size based on the specific application) to relocate the moving target to the road. Next, based on the road direction in the formed image, we can leverage this equation:

$$v_t^{(y)} = 14.1 \times v_t^{(x)} \tag{5.6}$$

where the constant 14.1 represents the road direction measured from the SAR image.

Then its velocity in z direction $v_t^{(z)}$ can be estimated by differentiating its relocated positions. The accuracy on estimating $v_t^{(z)}$ is thus limited by the accuracy of the DEM. Specifically, the $(v_t^{(x)}, v_t^{(y)}, v_t^{(z)})$ and $v_t^{(r)}$ follow this restriction (5.1).

Based on the geometrical restriction (5.1) and road information (5.6), we can estimate the target velocities $(v_t^{(x)}, v_t^{(y)}, v_t^{(z)})$. We compare our estimates to the ground truth and show the results in Table 5.2. It can be seen that the estimates on the target velocities match the ground truth with high accuracies. In practice, the geometrical information and DEM can be used as the auxiliary restrictions on other velocity estimation approaches to give SAR/GMTI applications better robustness.

Table 5.2: Comparisons between the ground truth and estimates.

sub-aperture number	1	2	3	4	5
estimated $v_t^{(x)}$ (m/s)	0.88	0.9	0.94	0.95	1.0
ground truth $v_t^{(x)}$ (m/s)	0.99	1.03	1.07	1.1	1.14
estimated $v_t^{(y)}$ (m/s)	12.4	12.72	13.2	13.4	14.1
ground truth $v_t^{(y)}$ (m/s)	12.9	13.1	13.3	13.5	13.7
estimated $v_t^{(z)}$ (m/s)	0.1	0.12	0.2	0.17	0.38
ground truth $v_t^{(z)}$ (m/s)	0.32	0.28	0.25	0.21	0.2

The results have shown the performance of using DEM and road prior information without sparsity in the target state estimation. Obviously the role of DEM in SAR/GMTI applications are crucial especially in the environments with significant elevation variations. The details about the target state estimation in combination with the exploitation of sparsity can be found in section 5.5 and related experiments are shown in the next subsection.

Sparsity-aided Moving Target Analysis

For the AFRL GOTCHA GMTI dataset, we have focused on the moving target with the 15-by-15 window centered at the target, extracted the phase history of this target $\mathbf{Y}_{d1}$, and estimated its radial velocity. Now we estimate its full velocity vector $\mathbf{v}_t$ and further image the target based on the estimated $\mathbf{v}_t$. The model (5.5) is first introduced to estimate the $\mathbf{v}_t$. In particular, for far-field observation, the target velocity components obey the geometrical restriction Υ which can be transformed into (5.1).

The retrieved 15-iteration results of the extracted moving targets are used here for the moving target state estimation and imaging. As $v^{(z)}$ is in general not too large in most scenarios, we can approximate it by differentiating the coordinates of the relocated target at different frames. Given the estimated $v^{(r)}$ and (5.1), $v^{(x)}$ is a function of $v^{(y)}$. The estimation of the velocity components can then be solved via the exhaustive search. In (5.5), we simply traverse $v^{(y)}$ from 0 m/s to line search for our estimations. The target image $\Theta^{\mathbf{v}_t}(\mathbf{Y}_{d1})$ for each velocity vector $\mathbf{v}_t$ is formed via two iterations of LSQR to obtain good data fidelity, and its support is bounded with a 10-by-10 window centered at the strongest pixel of the target. By searching for the minimised $\|\Theta^{\mathbf{v}_t}(\mathbf{Y}_{d1})\|_1$, we find the estimated $\mathbf{v}_t$ that gives the sparsest image.
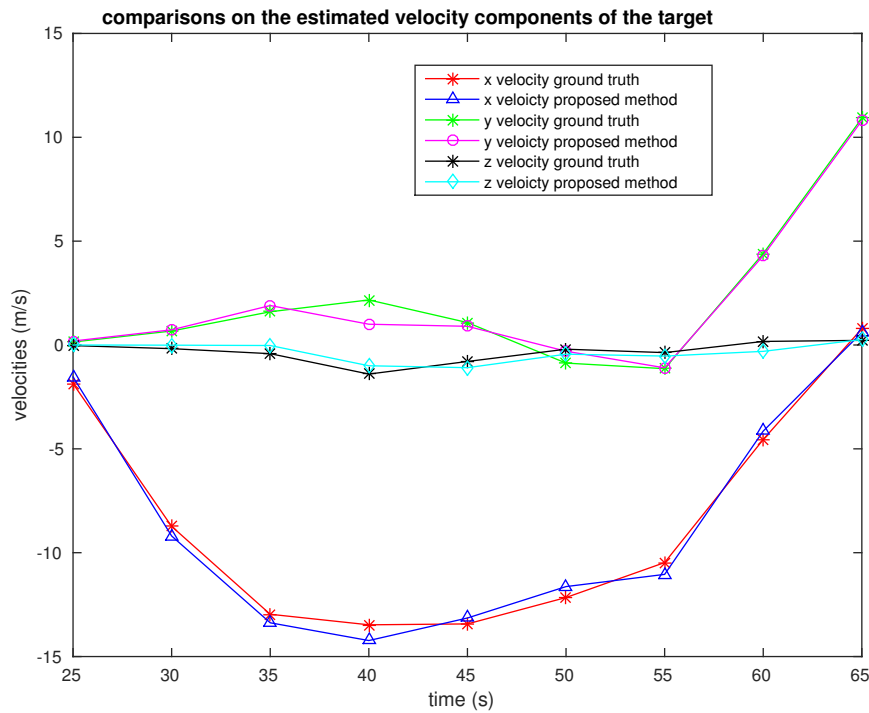

Figure 5.8: The comparisons of the target velocity components with the ground truth.

The positions of the target are tracked at nine sub-apertures with the moving target imaging

method and the estimated target velocities. We compare the estimated target velocities to the ground truth in x, y and z directions respectively, and show the estimated velocity components in Fig. 5.8. It can be seen from Fig. 5.8 that the velocity components in the z direction is generally not too large, and they can be roughly estimated by differentiating the physical coordinates. Although direct differentiation has limited accuracy, the estimation on $v^{(z)}$ matches the ground truth in most scenarios. The estimates on $v^{(x)}$ and $v^{(y)}$ rely on the proposed method and the insertion of geophysical information. We also achieved good matches against the ground truth. We compare the target locations after relocations to the results using hybrid DPCA/ATI algorithm and show their performance in Fig. 5.9. The proposed method has shown better accuracy in localising moving targets with 15 iterations compared to the hybrid DPCA/ATI.
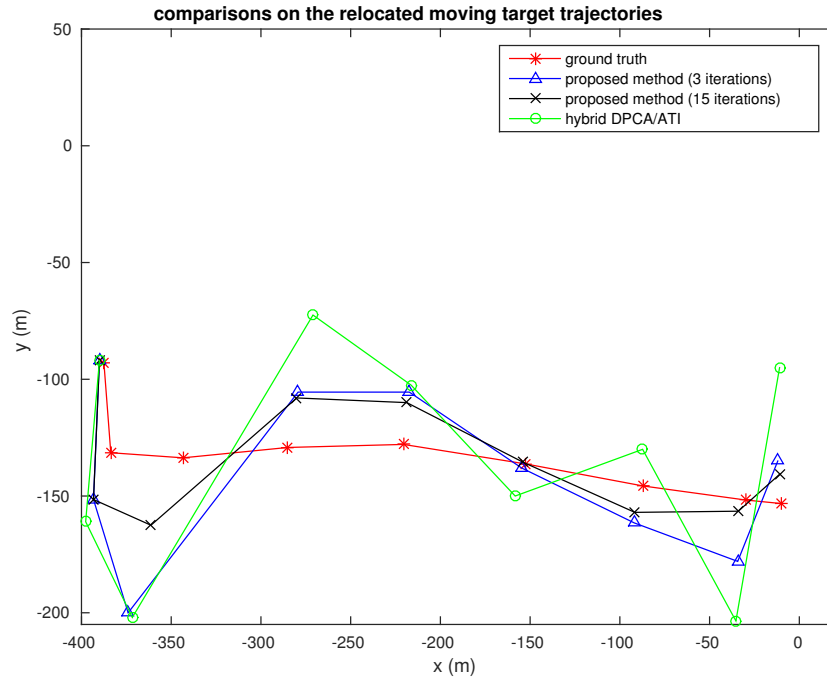
Figure 5.9: The comparisons of the target relocations with the proposed approach and hybrid DPCA/ATI.

Furthermore, the relocated and refocused target image of the $50-$th second is visualised in Fig. 5.10. As can be seen from this figure, the pixels of the moving target in Fig. 5.10 a) are refocused and relocated in in Fig. 5.10 b). Significant imaging improvements have been achieved for this moving target.

Note that the target state estimation methods in the state-of-the-art algorithms EDPCA [91] and ISTAP [18] are maximising the generalised likelihood ratio tests (GLRT) for image pixels. They are essentially searching for the motion parameters to best focus the moving targets pixel-wise in the image domain. We adopt this idea to maximise the target response on the relocated
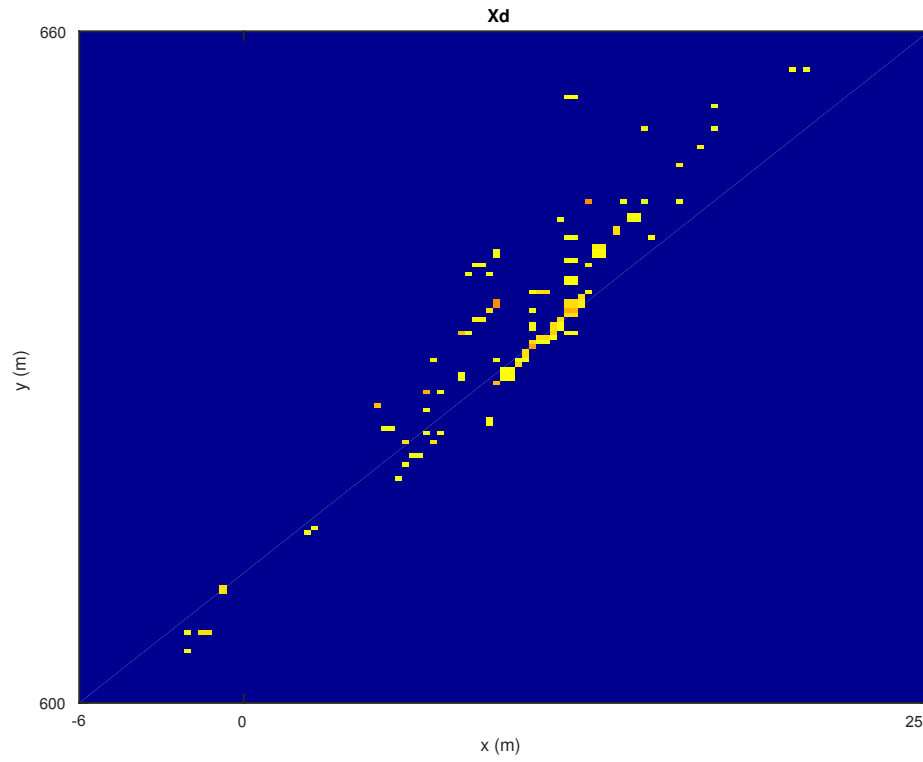
(a)
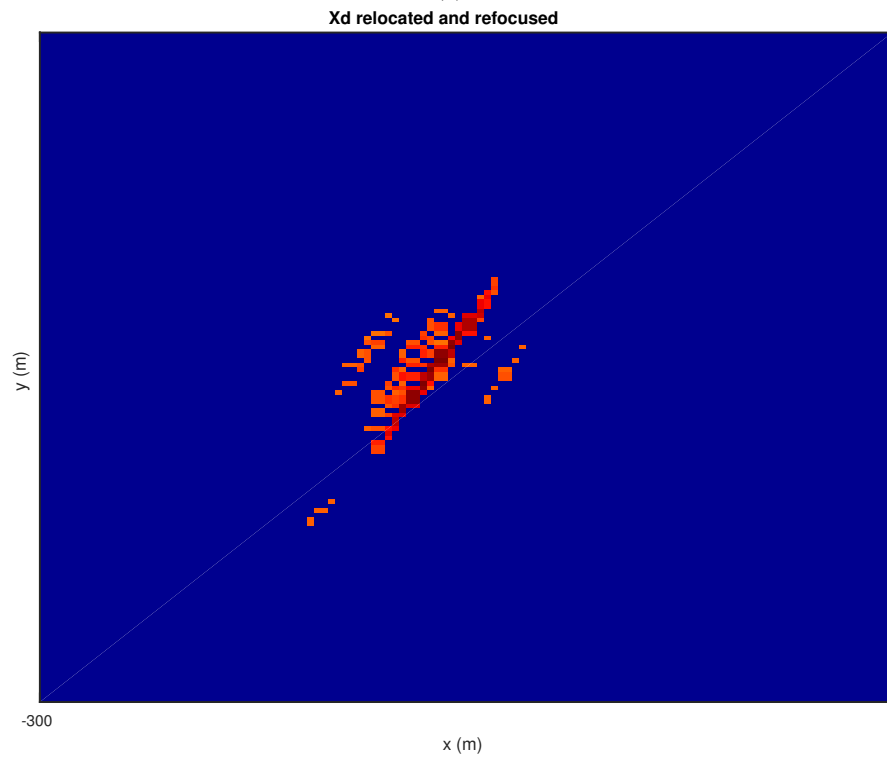
(b)

Figure 5.10: a) The SAR image of the extracted moving target in Chapter 4. b) The SAR image of the moving target after relocation and refocusing.

target spot, and search for the target state that gives the maximised energy. The results are presented in Fig. 5.11 for comparisons.
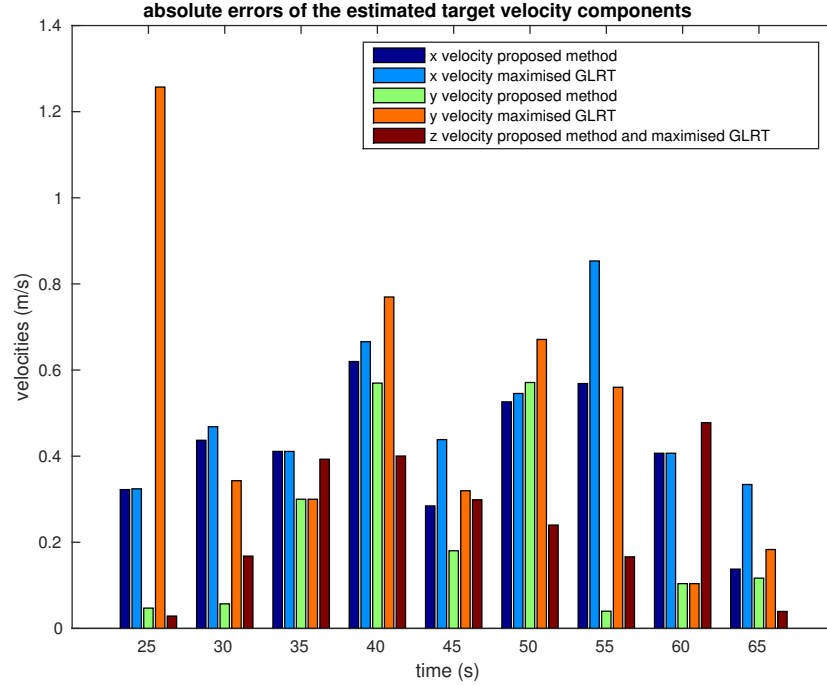
Figure 5.11: The comparisons on the absolute estimation errors of target velocity components.

It is shown in Fig. 5.11 that the proposed sparsity-aided algorithm has achieved better estimation accuracies in estimating the motion parameters of moving targets $v^{(x)}$ and $v^{(y)}$ than the maximised GLRT method. The proposed state estimation has further practical potential to be combined with the previous processing stage as they are both exploiting the target sparsities.

5.5 Summary

In this chapter we have investigated the utilisation of sparsities in moving target state estimation, target refocusing, and target relocations for practical multi-channel SAR-based GMTI application. We first explain the effects of moving targets in SAR/GMTI with details. Next, the recent developments in moving target state estimation and imaging are presented in this chapter. Particularly, one of the latest investigations in compressed sensing based GMTI is presented and the state-of-the-art EDPCA algorithm is briefly introduced. We then present the proposed novel algorithm for moving target state estimation and imaging. Within the proposed SAR/GMTI processing framework, for practical considerations, this algorithm is implemented as the final stage of the complete pipeline to accurately estimate target states, and form moving target images.

Furthermore, the DEM information can be flexibly incorporated into the processing. It is shown through simulations that the proposed methods have realised decent target states estimations and imaging. By comparing the proposed method to the state-of-the-art algorithms, we further demonstrate the effectiveness of the model through the real AFRL GOTCHA GMTI dataset on these challenging GMTI tasks.

6

Conclusions and Future Work

6.1 Conclusions

Within this thesis we have investigated the SAR-based GMTI approaches by utilising target sparsities. We are motivated by the state-of-the-art compressed sensing theory and conventional SAR/GMTI methods to design an end-to-end SAR-based GMTI framework which is capable of simultaneously forming high resolution SAR images, separating moving targets from the background, estimating target states, and forming moving target images. The utilisation of the DEM information is also incorporated into the proposed framework. The developed methods aim at tackling typical SAR/GMTI missions such as the AFRL GOTCHA GMTI challenges [4] to indicate a controlled moving vehicle (GPS device mounted) in a mountainous region using the acquired SAR data. The experiments in this thesis is limited to the single real dataset, i.e. the AFRL GOTCHA GMTI challenge dataset, and numerical simulations.

Conventional SAR imaging algorithms, such as the matched filtering and back-projection algorithms [51] [126], are essentially approximating the solution of an optimisation problem to achieve the best data-fitting. In general, the SAR/GMTI algorithms can be classified into two classes, i.e. the raw-data-based algorithms such as STAP and the image-based algorithms such as DPCA and ATI. Particularly, DPCA and ATI are widely used subtractive methods to compare the differences between SAR channels in the image domain, and they are closely related to the SAR image formation algorithms. Within this context, there exists the potential to reformulate the GMTI algorithms into optimisation tasks. This motivation is presented in Chapter 2. In Chapter 2, we analyse the Radar system features, such as the resolution and pulse compression, and present the mathematical signal model of SAR systems. The commonly used GMTI algorithms including STAP, DPCA, ATI, and hybrid DPCA/ATI are briefly introduced. We also explain the similarities and differences between different GMTI methods and the proposed SAR/GMTI methods within Chapter 2.

Compressed sensing is a revolutionary signal acquiring technique which had a breakthrough in its theory around 2005 [36]. It has been proved that, with significantly under-sampled projection data, the original signal can be reconstructed with high probabilities if the signal has inherent sparse prior information. The achieved sampling rate can be lower than the well-known Nyquist-Shannon sampling rate. Based on the theoretic foundations, a number of sparse approximation algorithms have been developed in this field. These approaches can be extended to the applications that aim to reconstruct the signals using sparse structures. Note that the SAR moving targets are approximately sparse in the observed scene. Furthermore, the conventional DPCA approach followed by a thresholding process is very similar to the iterative procedures in greedy CS algorithms. We are thus motivated to utilise the sparse information in SAR/GMTI applications.

Considering the SAR-based GMTI applications, some essential parts have to be investigated. Firstly, the multi-channel SAR systems can reveal moving targets through the differences between different channels. As the received signal of the aft-antenna can be viewed as the delayed received signal of the fore-antenna, only moving targets will induce significant differences through the subtractions. We thus need to calibrate the phase histories before the GMTI process to produce the same responses between different channels for stationary reflectors. This channel balancing is analysed in Chapter 3. Secondly, the SAR-based GMTI process will have significant estimation errors when the observed scene contains large elevation variations. We investigated the utilisation of the DEM information in Chapter 3. The DEM-aided moving target imaging is also presented. We demonstrate the effects of channel balancing and DEM in details with real data in Chapter 3.

By considering the SAR image formation from the optimisation perspective and leveraging multi-channel models, we can establish a sparsity-regularised model for simultaneous SAR imaging and moving target indication. In Chapter 4, we have explained the proposed model. However, solving this optimisation problem within one processing stage is very challenging as the target locations change as a function of their estimated velocities. Therefore a practical solution is designed to break the problem into a two stage process where we first utilise target sparsities to separate the blurred and misplaced moving targets from the static background scene and subsequently relocate and refocus individual moving targets, again exploiting the sparsity constraint. While the two stage process sacrifices a degree of sparsity (the blurred targets are less sparse than the correctly focused ones) but results in a simpler more tractable problem. This two-stage implementation architecture is also more comparable to the conventional SAR/GMTI processing chain. In Chapter 4, the practical implementation for target detection is discussed in details. The performance of the proposed model is also analysed. We demonstrate the effectiveness

of the proposed method through comprehensive experiments including simulations and real data tests.

Following the moving target extraction described in Chapter 4, we again utilise the target sparsities in Chapter 5 for moving target imaging and moving target state estimation. The proposed method focuses on individual moving targets to employ the moving target analysis. We compare its performance to that of the state-of-the-art algorithms EDPCA [91] and ISTAP [18]. The estimation of targets states has achieved high estimation accuracy based on the ground truth. The DEM information can be leveraged to enhance this process, and the DEM-aided target state estimation is explained in Chapter 5. We therefore establish a complete SAR/GMTI framework for separating moving targets from the background, estimating the states of the targets, and relocating and refocusing the targets under multi-channel SAR scenarios.

Overall, the proposed framework is motivated by integrating SAR/GMTI tasks into an sparsity regularised optimisation problem. The proposed methods are able to implement decompositions of moving targets and the background instead of simple targets detection. The extracted targets can be imaged and their motion parameters can be estimated. We also consider pre-processing and the DEM information in this framework. In practice, a two stage process is designed to resolve the framework considering the difficulties in computational load and forward/backward operators. Throughout this thesis, a number of experiments have been conducted based on the AFRL GOTCHA GMTI challenge dataset [4] to demonstrate the developed algorithms. The numerical simulations are also provided to prove the effectiveness of these approaches. Note that the real data tests of this thesis are limited to the single AFRL GOTCHA GMTI dataset. In the future, other real datasets can be used to further justify the proposed methods.

6.2 Future Work

We have proposed a complete SAR/GMTI processing framework by utilising moving target sparsities in this thesis. Based on the practical problems we noticed in the implementations, we hereby list six future research directions.

First of all, the channel balancing technique employed in this thesis is a very efficient algorithm for practical applications. We have analysed its performance in Chapter 3. However, this fast balancing technique is based on the fact that static reflectors are dominating in the observed

scene. Although it provides well balancing performance for the whole region, the balancing effects for specific targets are not optimal. Especially the imperfect channel balancing on strong static buildings will lead to the false alarms in the subsequent GMTI processing. How to better calibrate the strong reflectors in the pre-processing step is an open challenge to be investigated in the future. The behaviours of different types of objects in the pre-processing are also of our interest.

Secondly, SAR algorithms are associated with huge volume data processing. Typical SAR forward/backward operators are often computational intensive. The proposed SAR/GMTI framework requires multiple times of these operators in each iteration. The overall computational load is high though efficient algorithms have been leveraged to significantly accelerate the processings. Furthermore, we do not have the efficient SAR forward/backward operators for the SAR image formation with a global velocity map. To conclude, more efficient SAR operators and fast operators with the global velocity map are of interest to us in the future research.

Thirdly, we break the practical implementation of the end-to-end SAR/GMTI framework into a two stage processing. We first utilise target sparsities to separate the blurred and displaced moving targets from the static background scene and subsequently relocate and refocus individual moving targets, again exploiting the sparsity constraint. This is partially driven by the second future research direction as we have difficulties in designing efficient SAR operators. The target locations change as a function of their estimated velocities, and the SAR imaging with a global velocity map is very computational expensive. Another reason for two processing stages is that this pipeline is consistent with the conventional SAR/GMTI to first detect the moving targets, and then estimate their states. As both the two stages are essentially exploiting the target sparsities, there exist the potential to combine them into one processing step if efficient implementation can be designed.

Fourth, the target states estimation in this thesis is associated with the velocity components in x, y and z directions, i.e. the first order terms among the target motion parameters. In practice, the targets often have complicated movements and higher order motion terms need to be estimated. For example, a typical uniform acceleration will induce a constant change rate in velocities. Therefore, in this thesis, we are employing a simplified motion model of the moving targets, and the accuracies of target states estimation are limited. Further investigations can be done in the future to incorporate more complicated target movements into the proposed SAR/GMTI framework.

And fifth, the design of the proposed SAR/GMTI framework is based on a typical scenario

with moving targets in the scene, and typical tasks include target detections and target states estimation. There exists the potential to exploit the change detection methods [87] with different sub-apertures to aid the SAR/GMTI algorithms. Furthermore, in a number of SAR/GMTI scenarios, the SAR observation missions are implemented without moving targets to provide the reference data. The acquired reference data is essentially monitoring a background, and it can then be used in the change detection algorithms to be compared with the data that contains moving targets.

Lastly, SAR systems are typically complicated system engineering works. The SAR-based GMTI is associated with various considerations such as the blind velocities in radial velocity estimations (the complex exponential functions are periodic), the too strong background and target patterns (target often consists of multiple pixels). The SAR/GMTI estimation accuracy is thus limited by multiple factors. There have been a number of investigations in tackling these issues. The systematic solution of these problems to be combined with the proposed SAR/GMTI framework is of interest to us in the future.

Bibliography

[1] S.I. Kelly and M.E. Davies. A fast decimation-in-image back-projection algorithm for SAR. In *Radar Conference, 2014 IEEE*, pages 1046–1051, May 2014.

[2] W. M. Brown. Synthetic aperture radar. *IEEE Transactions on Aerospace and Electronic Systems*, AES-3(2):217–229, March 1967.

[3] A. Moreira, P. Prats-Iraola, M. Younis, G. Krieger, I. Hajnsek, and K. P. Papathanassiou. A tutorial on synthetic aperture radar. *IEEE Geoscience and Remote Sensing Magazine*, 1(1):6–43, March 2013.

[4] Steven M. Scarborough, Curtis H. Casteel, Jr., LeRoy Gorham, Michael J. Minardi, Uttam K. Majumder, Matthew G. Judge, Edmund Zelnio, Michael Bryant, Howard Nichols, and Douglas Page. A challenge problem for SAR-based GMTI in urban environments. *Proc. SPIE*, 7337:73370G–73370G–10, 2009.

[5] Di Wu, M. Yaghoobi, and M. Davies. Digital elevation model aided SAR-based GMTI processing in urban environments. In *Sensor Signal Processing for Defence (SSPD), 2016*, pages 1–5, Sept 2016.

[6] Di Wu, M. Yaghoobi, and M. Davies. A new approach to moving targets and background separation in multi-channel SAR. In *2016 IEEE Radar Conference*, 2016.

[7] D Wu, M Yaghoobi, SI Kelly, ME Davies, and R Clewes. A sparse regularized model for raman spectral analysis. In *Sensor Signal Processing for Defence*, Edinburgh, 2014.

[8] Mehrdad Yaghoobi Vaighan, Di Wu, and Michael Davies. Fast non-negative orthogonal matching pursuit. *IEEE Signal Processing Letters*, 22(9):1229–1233, 1 2015.

[9] Mehrdad Yaghoobi Vaighan, Di Wu, Rhea Clewes, and Michael Davies. *Fast Sparse Raman Spectral Unmixing for Chemical Fingerprinting and Quantification*. SPIE Security + Defence, 9 2016.

[10] Di Wu, M. Yaghoobi, and M. Davies. Sparsity based ground moving target imaging via multi-channel SAR. In *Sensor Signal Processing for Defence (SSPD), 2015*, pages 1–5,

Sept 2015.

[11] G.L. Charvat. *Small and Short-Range Radar Systems*. Modern and Practical Approaches to Electrical Engineering. CRC Press, 2014.

[12] Carl A Wiley. Synthetic aperture radars. *IEEE Transactions on Aerospace and Electronic Systems*, (3):440–443, 1985.

[13] C. W. Sherwin, J. P. Ruina, and R. D. Rawcliffe. Some early developments in synthetic aperture radar systems. *IRE Transactions on Military Electronics*, MIL-6(2):111–115, April 1962.

[14] R. Jordan and D. Held. The SEASAT - a synthetic aperture RADAR. In *1979 IEEE MTT-S International Microwave Symposium Digest*, pages 547–547, April 1979.

[15] I. Cumming and J. Bennett. Digital processing of Seasat SAR data. In *ICASSP '79. IEEE International Conference on Acoustics, Speech, and Signal Processing*, volume 4, pages 710–718, Apr 1979.

[16] R. Bamler. A comparison of range-Doppler and wavenumber domain SAR focusing algorithms. *IEEE Transactions on Geoscience and Remote Sensing*, 30(4):706–713, Jul 1992.

[17] Z. Jianxiong, S. Zhiguang, C. Xiao, and F. Qiang. Automatic target recognition of SAR images based on global scattering center model. *IEEE Transactions on Geoscience and Remote Sensing*, 49(10):3713–3729, Oct 2011.

[18] D. Cerutti-Maori, I. Sikaneta, and C. H. Gierull. Optimum SAR/GMTI processing and its application to the radar satellite radarsat-2 for traffic monitoring. *IEEE Transactions on Geoscience and Remote Sensing*, 50(10):3868–3881, Oct 2012.

[19] W. M. Boerner. Basics of SAR polarimetry. *RTO SET Lecture Series*, 2004.

[20] R. GENS and J. L. VAN GENDEREN. Review article sar interferometry — Issues, techniques, applications. *International Journal of Remote Sensing*, 17(10):1803–1835, 1996.

[21] P. A. Rosen, S. Hensley, I. R. Joughin, F. K. Li, S. N. Madsen, E. Rodriguez, and R. M. Goldstein. Synthetic aperture radar interferometry. *Proceedings of the IEEE*, 88(3):333–382, March 2000.

[22] K. Eldhuset. Principles and performance of an automated ship detection system for SAR images. In *12th Canadian Symposium on Remote Sensing Geoscience and Remote Sensing Symposium,*, volume 1, pages 358–361, July 1989.

[23] M. J. Minardi, L. A. Gorham, and E. G. Zelnio. Ground moving target detection and tracking based on generalized SAR processing and change detection. volume 5808, pages 156–165, 2005.

[24] J. J. Thiagarajan, K. N. Ramamurthy, P. Knee, A. Spanias, and V. Berisha. Sparse representations for automatic target classification in SAR images. In *2010 4th International Symposium on Communications, Control and Signal Processing (ISCCSP)*, pages 1–4, March 2010.

[25] F. Zhou, R. Wu, M. Xing, and Z. Bao. Approach for single channel SAR ground moving target imaging and motion parameter estimation. *IET Radar, Sonar Navigation*, 1(1):59–66, Feb 2007.

[26] E. Chapin and C. W. Chen. Preliminary results from an airborne experiment using along-track interferometry for ground moving target indication. In *IEEE International Radar Conference, 2005.*, pages 343–347, May 2005.

[27] M. Gabele and I. Sikaneta. A new method to create a virtual third antenna from a two-channel SAR-GMTI system. In *2007 International Waveform Diversity and Design Conference*, pages 433–437, June 2007.

[28] F.R. Dickey Jr. and M.M. Santa. Final report on anti-clutter techniques. *General Electric Co., Heavy Military Electron. Dep., Rep. no. R65EMH37, Syracuse, NY*, 1953.

[29] Shen Chiu and Chuck Livingstone. A comparison of displaced phase centre antenna and along-track interferometry techniques for RADARSAT-2 ground moving target indication. *Canadian Journal of Remote Sensing*, 31(1):37–51, 2005.

[30] T. J. Nohara. Comparison of DPCA and STAP for space-based radar. In *Proceedings International Radar Conference*, pages 113–119, May 1995.

[31] J. Ward. Space-time adaptive processing for airborne radar. In *Space-Time Adaptive Processing (Ref. No. 1998/241), IEE Colloquium on*, pages 2/1–2/6, Apr 1998.

[32] J.H.G. Ender. Space-time adaptive processing for synthetic aperture radar. In *Space-Time Adaptive Processing (Ref. No. 1998/241), IEE Colloquium on*, pages 6/1–618, Apr 1998.

[33] C. E. Shannon. Communication in the Presence of Noise. *Proceedings of the IRE*, 37(1):10–21, January 1949.

[34] Simon Foucart and Holger Rauhut. *A Mathematical Introduction to Compressive Sensing*. Birkhuser, 2013.

[35] David L Donoho. Compressed sensing. *IEEE Transactions on information theory*, 52(4):1289–1306, 2006.

[36] Emmanuel J Candes, Justin K Romberg, and Terence Tao. Stable signal recovery from incomplete and inaccurate measurements. *Communications on pure and applied mathematics*, 59(8):1207–1223, 2006.

[37] Moeness Amin. *Compressive sensing for urban radar*. Taylor and Francis, Hoboken, NJ, 2014.

[38] M. F. Duarte, M. A. Davenport, D. Takhar, J. N. Laska, Ting Sun, K. F. Kelly, and R. G. Baraniuk. Single-Pixel Imaging via Compressive Sampling. *Signal Processing Magazine, IEEE*, 25(2):83–91, March 2008.

[39] Chao Wu, Di Wu, Shuilin Yan, and Yike Guo. Sensor deployment in bayesian compressive sensing based environmental monitoring. In *MOBIQUITOUS 2013*, 2013.

[40] Antoine Liutkus, David Martina, Sébastien Popoff, Gilles Chardon, Ori Katz, Geoffroy Lerosey, Sylvain Gigan, Laurent Daudet, and Igor Carron. Imaging with nature: Compressive imaging using a multiply scattering medium. *Scientific reports*, 4, 2014.

[41] Michael Lustig, David Donoho, and John M. Pauly. Sparse MRI: The application of compressed sensing for rapid MR imaging. *Magnetic Resonance in Medicine*, 58(6):1182–1195, 2007.

[42] M. Lustig, D. L. Donoho, J. M. Santos, and J. M. Pauly. Compressed Sensing MRI. *Signal Processing Magazine, IEEE*, 25(2):72–82, March 2008.

[43] J. Wang, S. Tang, Baocai Yin, and Xiang-Yang Li. Data gathering in wireless sensor networks through intelligent compressive sensing. In *2012 Proceedings IEEE INFOCOM*, pages 603–611, March 2012.

[44] Yee Kit Chan and Voon Chet Koo. An introduction to synthetic aperture radar (SAR). *Progress In Electromagnetics Research B*, 2:27–60, 2008.

[45] Geomatics Consulting Thomas P. Ager — Tomager LLC and VA Training, Lansdowne. An introduction to synthetic aperture radar imaging. *Oceanography*, 26, June 2013.

[46] G. Turin. An introduction to matched filters. *IRE Transactions on Information Theory*, 6(3):311–329, June 1960.

[47] G. Franceschetti and R. Lanari. *Synthetic Aperture Radar Processing*. Electronic Engineering Systems. Taylor & Francis, 1999.

[48] M. Soumekh. *Synthetic Aperture Radar Signal Processing with MATLAB Algorithms*. Wiley, 1999.

[49] W.G. Carrara, R.S. Goodman, and R.M. Majewski. *Spotlight Synthetic Aperture Radar: Signal Processing Algorithms*. Artech House signal processing library. Artech House, 1995.

[50] B. D. Rigling and R. L. Moses. Taylor expansion of the differential range for monostatic SAR. *IEEE Transactions on Aerospace and Electronic Systems*, 41(1):60–64, Jan 2005.

[51] LeRoy A. Gorham and Linda J. Moore. SAR image formation toolbox for MATLAB. In Edmund G. Zelnio and Frederick D. Garber, editors, *Proc. of SPIE*, volume 7699, page 769906. SPIE, 2010.

[52] Max Born. Zur quantenmechanik der stoßvorgänge. *Zeitschrift für Physik*, 37(12):863–867, Dec 1926.

[53] C. Oliver and S. Quegan. *Understanding Synthetic Aperture Radar Images*. SciTech radar and defense series. SciTech Publ., 2004.

[54] David S. Taubman and Michael W. Marcellin. *JPEG2000 : image compression fundamentals, standards, and practice*. Kluwer Academic Publishers, Boston, 2002.

[55] Martin Vetterli, Pina Marziliano, and Thierry Blu. Sampling signals with finite rate of innovation. *IEEE Transactions on Signal Processing*, 50(6):1417–1428, 2002.

[56] Emmanuel J. Candès and Terence Tao. Near-optimal signal recovery from random projections: Universal encoding strategies? *IEEE Transactions on Information Theory*, 52(12):5406–5425, 2006.

[57] Emmanuel J. Candès and Carlos Fernandez-Granda. Towards a mathematical theory of super-resolution. *CoRR*, abs/1203.5871, 2012.

[58] Emmanuel J. Candès and Terence Tao. Decoding by linear programming. *IEEE Trans. Information Theory*, 51(12):4203–4215, 2005.

[59] Mark A. Davenport, Marco F. Duarte, Yonina C. Eldar, and Gitta Kutyniok. *Introduction to compressed sensing*. Cambridge University Press, 2012.

[60] Fan Yang, Shengqian Wang, and Chengzhi Deng. Compressive sensing of image reconstruction using multi-wavelet transforms. In *2010 IEEE International Conference on Intelligent Computing and Intelligent Systems*, volume 1, pages 702–705, Oct 2010.

[61] David L. Donoho, Michael Elad, and Vladimir N. Temlyakov. Stable recovery of sparse overcomplete representations in the presence of noise. *IEEE TRANS. INFORM. THEORY*, 52(1):6–18, 2006.

[62] Joel A. Tropp. Just relax: Convex programming methods for subset selection and sparse approximation. Technical report, 2004.

[63] Emmanuel J. Candès, Yonina C. Eldar, Deanna Needell, and Paige Randall. Compressed sensing with coherent and redundant dictionaries. *Applied and Computational Harmonic Analysis*, 31(1):59 – 73, 2011.

[64] L. Welch. Lower bounds on the maximum cross correlation of signals (corresp.). *IEEE Trans. Inf. Theor.*, 20(3):397–399, September 2006.

[65] M. F. Duarte and Y. C. Eldar. Structured compressed sensing: From theory to applications. *IEEE Transactions on Signal Processing*, 59(9):4053–4085, Sept 2011.

[66] J. A. Tropp. Greed is good: algorithmic results for sparse approximation. *IEEE Transactions on Information Theory*, 50(10):2231–2242, Oct 2004.

[67] L. Carin, D. Liu, and B. Guo. Coherence, compressive sensing, and random sensor arrays. *IEEE Antennas and Propagation Magazine*, 53(4):28–39, Aug 2011.

[68] Emmanuel J. Candès, Justin Romberg, and Terence Tao. Robust uncertainty principles: Exact signal reconstruction from highly incomplete frequency information, 2006.

[69] M. F. Duarte, M. A. Davenport, M. B. Wakin, and R. G. Baraniuk. Sparse signal detection from incoherent projections. In *2006 IEEE International Conference on Acoustics Speech and Signal Processing Proceedings*, volume 3, pages III–III, May 2006.

[70] Mark A Davenport. *Random observations on random observations: Sparse signal*

acquisition and processing. Rice University, 2010.

[71] Robert Tibshirani. Regression shrinkage and selection via the LASSO. *Journal of the Royal Statistical Society, Series B*, 58:267–288, 1994.

[72] Bradley Efron, Trevor Hastie, Iain Johnstone, and Robert Tibshirani. Least angle regression. *Annals of Statistics*, 32:407–499, 2004.

[73] David L. Donoho. For most large underdetermined systems of linear equations the minimal l1-norm solution is also the sparsest solution. *Comm. Pure Appl. Math*, 59:797–829, 2004.

[74] J. Wright, A. Y. Yang, A. Ganesh, S. S. Sastry, and Y. Ma. Robust face recognition via sparse representation. *IEEE Transactions on Pattern Analysis and Machine Intelligence*, 31(2):210–227, Feb 2009.

[75] M. Elad. Sparse and redundant representations: From theory to applications in signal and image processing. *Springer*, 2010.

[76] Joel A. Tropp and Anna C. Gilbert. Signal recovery from random measurements via orthogonal matching pursuit. *IEEE TRANS. INFORM. THEORY*, 53:4655–4666, 2007.

[77] Y. C. Pati, R. Rezaiifar, Y. C. Pati R. Rezaiifar, and P. S. Krishnaprasad. Orthogonal matching pursuit: Recursive function approximation with applications to wavelet decomposition. In *Proceedings of the 27 th Annual Asilomar Conference on Signals, Systems, and Computers*, pages 40–44, 1993.

[78] Thomas Blumensath and Mike E. Davies. Iterative hard thresholding for compressed sensing. *CoRR*, abs/0805.0510, 2008.

[79] Z. Zhang, Y. Xu, J. Yang, X. Li, and D. Zhang. A survey of sparse representation: Algorithms and applications. *IEEE Access*, 3:490–530, 2015.

[80] D. Needell and R. Vershynin. Signal recovery from incomplete and inaccurate measurements via regularized orthogonal matching pursuit. *IEEE Journal of Selected Topics in Signal Processing*, 4(2):310–316, April 2010.

[81] Deanna Needell and Joel A Tropp. Cosamp: Iterative signal recovery from incomplete and inaccurate samples. *Applied and Computational Harmonic Analysis*, 26(3):301–321, 2009.

[82] David L. Donoho, Yaakov Tsaig, Iddo Drori, and Jean luc Starck. Sparse solution of underdetermined linear equations by stagewise orthogonal matching pursuit. Technical

report, 2006.

[83] T. T. Do, L. Gan, N. Nguyen, and T. D. Tran. Sparsity adaptive matching pursuit algorithm for practical compressed sensing. In *2008 42nd Asilomar Conference on Signals, Systems and Computers*, pages 581–587, Oct 2008.

[84] R. K. Hersey and E. Culpepper. Radar processing architecture for simultaneous SAR, GMTI, ATR, and tracking. In *2016 IEEE Radar Conference (RadarConf)*, pages 1–5, May 2016.

[85] K. Eldhuset. An automatic ship and ship wake detection system for spaceborne SAR images in coastal regions. *IEEE Transactions on Geoscience and Remote Sensing*, 34(4):1010–1019, Jul 1996.

[86] S. Brusch, S. Lehner, T. Fritz, M. Soccorsi, A. Soloviev, and B. van Schie. Ship surveillance with terraSAR-X. *IEEE Transactions on Geoscience and Remote Sensing*, 49(3):1092–1103, March 2011.

[87] D. Pastina, G. Battistello, and A. Aprile. Change detection based GMTI on single channel SAR images. In *7th European Conference on Synthetic Aperture Radar*, pages 1–4, June 2008.

[88] M. Preiss and N.J.S. Stacy. Coherent change detection: Theoretical description and experimental results. *Defence Science and Technology Organisation (DSTO), Edinburgh, Australia, Tech. Rep. DSTO-TR-1851*, 2006.

[89] Shen Chiu and Chuck Livingstone. A comparison of displaced phase centre antenna and along-track interferometry techniques for RADARSAT-2 ground moving target indication. *Canadian Journal of Remote Sensing*, 31(1):37–51, 2005.

[90] I. Sikaneta and C. Gierull. Ground moving target detection for along-track interferometric SAR data. In *Aerospace Conference, 2004. Proceedings. 2004 IEEE*, volume 4, pages 2227–2235 Vol.4, March 2004.

[91] D. Cerutti-Maori and I. Sikaneta. A generalization of DPCA processing for multichannel SAR/GMTI radars. *IEEE Transactions on Geoscience and Remote Sensing*, 51(1):560–572, Jan 2013.

[92] Ross W. Deming, Scott MacIntosh, and Matthew Best. Three-channel processing for improved geo-location performance in SAR-based GMTI interferometry. *Proc. SPIE*,

8394:83940F–83940F–17, 2012.

[93] Ross Deming, Matthew Best, and Sean Farrell. Simultaneous SAR and GMTI using ATI/DPCA. *Proc. SPIE*, 9093:90930U–90930U–19, 2014.

[94] Ludger Prunte. GMTI from multichannel SAR images using compressed sensing. In *Synthetic Aperture Radar, 2012. EUSAR. 9th European Conference on*, pages 199–202, April 2012.

[95] H. M. Finn. Adaptive detection mode with threshold control as a function of spatially sampled clutter-level estimates. *RCA Review*, 29(2):414–464, 1968.

[96] M.C. Budge and S.R. German. *Basic Radar Analysis*. Artech House Radar Library. Artech House, 2015.

[97] J. H. G. Ender. Space-time processing for multichannel synthetic aperture radar. *Electronics Communication Engineering Journal*, 11(1):29–38, Feb 1999.

[98] Ross W. Deming. Along-track interferometry for simultaneous SAR and GMTI: application to gotcha challenge data. *Proc. SPIE*, 8051:80510P–80510P–18, 2011.

[99] Deng Haitao and Zhang Changyao. A real-time signal processing method for air-born three-channels GMTI. In *2007 1st Asian and Pacific Conference on Synthetic Aperture Radar*, pages 262–265, Nov 2007.

[100] Z. Hongbo, Y. Shaohua, and C. Demin. A signal processing method for airborne three-channel SAR-GMTI. In *2009 2nd Asian-Pacific Conference on Synthetic Aperture Radar*, pages 210–213, Oct 2009.

[101] J. H. G. Ender, P. Berens, A. R. Brenner, L. Rossing, and U. Skupin. Multi-channel SAR/MTI system development at FGAN: from AER to PAMIR. In *IEEE International Geoscience and Remote Sensing Symposium*, volume 3, pages 1697–1701 vol.3, June 2002.

[102] Z. Huang, J. Xu, S. Peng, and Z. Wang. A new channel balancing algorithm in image domain for multichannel sar-gmti system. In *IET International Radar Conference 2015*, pages 1–5, Oct 2015.

[103] Sune R. J. Axelsson. Position correction of moving targets in SAR imagery. *Proc. SPIE*, 5236:80–92, 2004.

[104] D. A. Garren. Smear signature morphology of surface targets with arbitrary motion in

spotlight synthetic aperture radar imagery. *IET Radar, Sonar Navigation*, 8(5):435–448, June 2014.

[105] Daniel Nuesch Maurice Ruegg, Erich Meier. Constant motion, acceleration, vibration, and rotation of objects in SAR data. In *Proc.SPIE*, volume 5980, 2005.

[106] N. Ozben Onhon and M. Cetin. SAR moving target imaging using group sparsity. In *Signal Processing Conference (EUSIPCO), 2013 Proceedings of the 21st European*, pages 1–5, Sept 2013.

[107] A. H. Oveis and M. A. Sebt. High resolution ground moving target indication by synthetic aperture radar using compressed sensing. In *2017 Iranian Conference on Electrical Engineering (ICEE)*, pages 1674–1679, May 2017.

[108] L. Pruente. Off-grid compressed sensing for GMTI using SAR images. In *CoSeRa*, 2013.

[109] L. Pruente. Compressed sensing for removing moving target artifacts and reducing noise in SAR images. In *Proceedings of EUSAR 2016: 11th European Conference on Synthetic Aperture Radar*, pages 1–6, June 2016.

[110] L. Pruente. Application of compressed sensing to SAR/GMTI-data. In *8th European Conference on Synthetic Aperture Radar*, pages 1–4, June 2010.

[111] ZONUMS. USGS seamless elevation data sets. *NASA EOSDIS Land Processes DAAC, USGS Earth Resources Observation and Science (EROS) Center, Sioux Falls, South Dakota*, 2010.

[112] B. Liu, K. Yin, Y. Li, F. Shen, and Z. Bao. An improvement in multichannel SAR-GMTI detection in heterogeneous environments. *IEEE Transactions on Geoscience and Remote Sensing*, 53(2):810–827, Feb 2015.

[113] C.H. Gierull. Digital channel balancing of along-track interferometric SAR data. In *Technical Memorandum DRDC Ottawa TM 2003-024*. Defence R&D, Ottawa, Canada, March 2003.

[114] Bin Guo, Duc Vu, Luzhou Xu, Ming Xue, and Jian Li. Ground moving target indication via multichannel airborne SAR. *IEEE T. Geoscience and Remote Sensing*, 49(10):3753–3764, 2011.

[115] Y. Li, R. Wu, M. Xing, and Z. Bao. Inverse synthetic aperture radar imaging of ship target

with complex motion. *IET Radar, Sonar Navigation*, 2(6):395–403, December 2008.

[116] C. Clapham, J. Nicholson, and J.R. Nicholson. *The Concise Oxford Dictionary of Mathematics*. Oxford Paperback Reference. OUP Oxford, 2014.

[117] Solomon W. Golomb and Leonard D. Baumert. Backtrack programming. *J. ACM*, 12(4):516–524, Oct 1965.

[118] Thomas Blumensath and Mike E. Davies. Iterative hard thresholding for compressed sensing. *Applied and Computational Harmonic Analysis*, 27(3):265 – 274, 2009.

[119] Thomas Blumensath and Mike E Davies. Iterative Thresholding for Sparse Approximations. *Journal of Fourier Analysis and Applications*, 14(5-6):629–654, December 2008.

[120] A. Beck and M. Teboulle. A Fast Iterative Shrinkage-Thresholding Algorithm for Linear Inverse Problems. *SIAM Journal on Imaging Sciences*, 2(1):183–202, March 2009.

[121] Richard M Goldstein and HA Zebker. Interferometric radar measurement of ocean surface currents. 1987.

[122] A. Budillon, V. Pascazio, and G. Schirinzi. Amplitude/phase approach for target velocity estimation in AT-InSAR systems. In *2008 IEEE Radar Conference*, pages 1–5, May 2008.

[123] G Palubinskas, F Meyer, H Runge, P Reinartz, R Scheiber, and R Bamler. Estimation of along-track velocity of road vehicles in SAR data. In *Remote Sensing*, pages 59820T–59820T. International Society for Optics and Photonics, 2005.

[124] Shen Chiu. Application of fractional Fourier transform to moving target indication via along-track interferometry. *EURASIP Journal on Advances in Signal Processing*, 2005(20):1–11, 2005.

[125] Christopher C. Paige and Michael A. Saunders. LSQR: An algorithm for sparse linear equations and sparse least squares. *ACM Trans. Math. Software*, pages 43–71, 1982.

[126] L. Rosenberg and D. Gray. Multichannel SAR imaging with backprojection. In *Proceedings of the 2004 Intelligent Sensors, Sensor Networks and Information Processing Conference, 2004.*, pages 265–270, Dec 2004.